

FRACTURE TOUGHNESS OF A HYPERELASTIC MATERIAL DURING  
SURGICAL CUTTING

by

KEVIN C. SMITH

A Thesis submitted in partial fulfillment of the requirements  
for the Honors in the Major Program in Mechanical Engineering  
in the College of Engineering and Computer Science  
and in the Burnett Honors College  
at the University of Central Florida  
Orlando, Florida

Spring Term 2013

Thesis Chair: Dr. Ali P. Gurdoin

## ABSTRACT

Despite being one of the most important organs of vertebrates, the material properties of skin are also one of the most poorly understood. In the field of designing medical devices and surgical tools there are significant advantages to having a model that describes the interaction of forces between a blade tip and skin during surgical cutting. In general, skin can best be described as a composite layer consisting of a viscoelastic dermis with interwoven collagen and elastin fibers beneath a superficial epidermis. The purpose of this research is to study the fracture toughness of porcine skin during practical cutting applications, the behavior of skin under quasi-static loads, and viscoelastic behavior of skin during stress relaxation. To fully describe the mechanics of skin in this model tensile test are conducted to determine the material properties of skin. The fracture toughness of the material is calculated by measuring the energy release rate of the material during required during cutting with Number 11 scalpel blade with a tip radius of  $12\mu\text{m}$ . These results are then compared to a finite element analysis with a debonding interface and a Mooney-Rivlin hyperelastic material model with viscoelastic relaxation in an effort to predict the loads required by tools during surgical applications. The main outcome of this research is the development of a testing protocol and material model of skin that can be used in finite element simulations of uniaxial loads and surgical cutting.

## ACKNOWLEDGEMENTS

## TABLE OF CONTENTS

1. INTRODUCTION .....	1
2. BACKGROUND .....	3
2.1 Material Properties .....	3
2.1.1 Orthotropic Nature .....	3
2.1.2 Linear Viscosity .....	5
2.1.3 Quasilinear Viscoelastic Relaxation .....	9
2.1.4 Hyperelasticity .....	10
2.1.5 Natural Variation .....	13
2.2 Quasi-Static Cutting .....	14
2.3 Existing Hemostatic Tools .....	17
2.4 Existing Biopsy Tools .....	20
2.5 New Biopsy Tools .....	22
3. EXPERIMENTAL APPROACH .....	30
3.1 Candidate Material .....	30
3.2 Specimen Preparation .....	32
3.3 Trial testing .....	35
3.4 Tensile Testing .....	37
3.5 Stress Relaxation .....	39
3.6 Cutting .....	39
4. DATA ANALYSIS .....	42
4.1 Pre-Load Testing .....	42
4.2 Tensile Testing .....	44
4.3 Relaxation Testing .....	53
4.4 Cutting .....	58
5. NUMERICAL APPROACH .....	61
5.1 Dog-Bone Model .....	61
5.2 Cutting Model .....	63

6. RESULTS .....	<b>Error! Bookmark not defined.</b>
7. CONCLUSIONS.....	79
8. FUTURE WORK .....	<b>Error! Bookmark not defined.</b>
BIBLIOGRAPHY .....	<b>Error! Bookmark not defined.</b>
APPENDIX A: CODES .....	87
A.1 Parametric Ansys Input File Scaled_Implicit_Interface_Mooney) .....	88

## LIST OF FIGURES

Figure 2.1: Skin Layer Diagram (Welch, Woloshin, & Schwartz, 2005).....	4
Figure 2.2: Kelvin-Voigt Model .....	6
Figure 2.3: Maxwell Model (Balmer).....	<b>Error! Bookmark not defined.</b>
Figure 2.4: Mode I Fracture Opening .....	15
Figure 2.5: Shave Biopsy (MacFarlane & Raphini, 2010) .....	21
Figure 2.6: Punch Biospy (MacFarlane & Raphini, 2010) .....	21
Figure 2.7: Excisional Biopsy (MacFarlane & Raphini, 2010) .....	21
Figure 2.8: Number 15 Scalpel in Mount .....	<b>Error! Bookmark not defined.</b>
Figure 2.9: Flat 12mm Punch.....	22
Figure 2.10: Rounded 12mm Punch .....	23
Figure 2.11: Elliptical Punch Cross-Section.....	<b>Error! Bookmark not defined.</b>
Figure 2.12: Flat 7.5mm Punch.....	23
Figure 2.13: Serrated 12mm Punch .....	<b>Error! Bookmark not defined.</b>
Figure 2.14: Vertical (90°) Puncture.....	24
Figure 2.15: Angled (56°) Puncture .....	<b>Error! Bookmark not defined.</b>
Figure 2.16: Elliptical 12mm Flat Bladed Punch Loads.....	25
Figure 2.17: Elliptical 7.5mm Punch Loads .....	26
Figure 2.18: #15 Scalpel Slicing Test.....	27
Figure 2.19: #15 Scalpel Puncture Test .....	<b>Error! Bookmark not defined.</b>
Figure 2.20: Elliptical Blade Rocking .....	26
Figure 2.21: Elliptical Blade Rocking .....	<b>Error! Bookmark not defined.</b>

Figure 2.22: (Surgical Blades) .....	28
Figure 2.23: Scalpel 90 Degree Punch.....	<b>Error! Bookmark not defined.</b>
Figure 2.24: Scalpel 90 Degree Slice.....	<b>Error! Bookmark not defined.</b>
Figure 3.1: Sample 1 Preconditioning Cycles.....	34
Figure 3.2: Saw-tooth PLA Clamps.....	35
Figure 3.3: Dog-bone Skin Specimen.....	31
Figure 3.4: Scalpel Mount Isometric View .....	40
Figure 3.5: Scalpel Mount Side View.....	<b>Error! Bookmark not defined.</b>
Figure 3.6: Cutting Assembly.....	41
Figure 4.1: Gauge Strain Cyclic Preload .....	42
Figure 4.2: Video Strain Cyclic Preload.....	43
Figure 4.3: Tensile Test with Scaled Gauge Strain.....	45
Figure 4.4: Tensile Test with Video Extensometer .....	46
Figure 4.5: Video Extension Tensile Data.....	46
Figure 4.6: Gauge Strain Tensile Data.....	47
Figure 4.7: Fit of Sample 17 Linear Stress-Strain Region.....	48
Figure 4.8: 2-Parameter Mooney Rivlin Fit.....	49
Figure 4.9: 3-Parameter Mooney Rivlin Fit.....	50
Figure 4.10: 5-Parameter Mooney Rivlin Fit.....	51
Figure 4.11: 9-Parameter Mooney Rivlin Fit.....	<b>Error! Bookmark not defined.</b>
Figure 4.12: 1 <sup>st</sup> Order Polynomial Fit.....	52
Figure 4.13: 2 <sup>nd</sup> Order Polynomial Fit .....	53

Figure 4.14: 3 <sup>rd</sup> Order Polynomial Fit.....	<b>Error! Bookmark not defined.</b>
Figure 4.15: Skin Relaxation at Constant 5% Strain .....	54
Figure 4.16: Skin Relaxation at Constant 10% Strain .....	55
Figure 4.17: Skin Relaxation at Constant 15% Strain .....	56
Figure 4.18: Normalized Stress-Relaxation.....	57
Figure 4.19: Load-Displacement During Skin Cutting with #11 Scalpel.....	58
Figure 5.1: Finite Element Analysis Diagram .....	64
Figure 5.2: Scalpel Microscopy .....	65

## LIST OF TABLES

Table 1: Skin Properties at Room Temperature.....	14
Table 2: Hysteresis Effects of Sample 1 .....	44
Table 3: Tensile Group .....	44
Table 4: Variables of 2-Parameter Mooney Rivlin Fit .....	49
Table 5: Variables of 3-Parameter Mooney Rivlin Fit .....	50
Table 6: Variables of 5-Parameter Mooney Rivlin Fit .....	51
Table 7: Variables of 9-Parameter Mooney Rivlin Fit .....	<b>Error! Bookmark not defined.</b>
Table 8: Variables of 1 <sup>st</sup> Order Polynomial Fit.....	52
Table 9: Variables of 2 <sup>nd</sup> Order Polynomial Fit.....	53
Table 10: Variables of 3 <sup>rd</sup> Order Polynomial Fit .....	<b>Error! Bookmark not defined.</b>
Table 11: Summary of Data for Relaxation of Skin of Skin of Skin at Constant 5% Strain .....	54
Table 12: Summary of Data for Relaxation of Skin of Skin of Skin at Constant 10% Strain .....	55
Table 13: Summary of Data for Relaxation of Skin of Skin of Skin at Constant 15% Strain .....	56
Table 14: Maxwell Viscosity .....	57
Table 15: Summary of Fracture Toughness.....	59

## NOMENCLATURE

$A$	Area
$u$	Blade displacement
$X$	Blade force
$\rho_w$	Density of water
$\sigma_E$	Elastic stress
$W$	Energy Density
$d\Gamma$	Energy lost due to remote plastic flow of sample
$C_w$	Heat Capacity of water
$I$	Invariant
$l$	Length
$l_0$	Length (initial)
$m_t$	Mass of tissue
$Y(t)$	Position of Ultrasonic Blade
$P$	Power
$T^\epsilon$	Quasilinear Stress
$G$	Relaxation Stress
$J$	Resistance to Fracture
$d\Lambda$	Stored strain energy due to tension of the material
$\dot{\epsilon}$	Strain Rate
$\lambda$	Stretch Ratio

$T_c$	Temperature of cauterization
$Y_0$	Ultrasonic Blade Amplitude
$V_0$	Velocity of Ultrasonic Blade
$\sigma_v$	Viscous stress
$\nu$	Viscosity
$V$	Voltage
$E$	Young's Modulus

## 1. INTRODUCTION

To meet the growing demand of precision and safety in medical procedures a number of new constitutive models have been developed into an attempt to characterize the behavior of the human body in response to thermal, electrical, and mechanical stimuli for the development of new surgical instruments and implants. In recent years, the biomedical industry has developed an increasing interest in the more efficient biopsy tools and the uses of hemostatic cutting to minimize recovery time.

An example of such a tool is a recently prototyped elliptical biopsy punch for dermatological procedures involving the removal of moles, warts, and growths for clinical testing. It is believed that a 3:1 elliptical incision will be easier to suture shut and recovery faster than round holes produced by circular biopsy punches currently on the market (Weiner et al., 2009; Messana and Wagner, 2008). However, preliminary testing of this device has shown that the fracture toughness of tissue must be taken into account in the design of a new surgical instrument to minimize the loads required during the procedure. This need has led to a growing interest in the mechanical properties of skin for simulation purposes.

The mechanical behavior of such biomaterials has exhibited a great deal of uncertainty because of the complex microstructure and many independent variables affecting the tissue properties; such as time, temperature, health, etc. This is why many authors in tissue mechanics, such as Humphrey, have placed emphasis on the fact that the constitutive models used to describe biomaterials can only be considered accurate under a very specific set of circumstances; which do not always reflect in vivo conditions and often widely vary in testing protocols

between researchers (Humphrey, 2008).

The aim of this research is provide a foundation in the mechanical behavior testing of biomaterials and the development of a constitutive model that could be used to predict the loads encountered and energy dissipated during surgical cutting. The candidate material is porcine skin, which is readily available and considered acceptable substitute for human skin consistency. The stress-strain behavior of the tissue is most effectively regressed with a hyperelastic and viscoelastic constitutive model during uniaxial testing with the use video extensometers for strain measurements. The accuracy of these models during surgical conditions is further verified through experimental cutting of the tissue with surgical tools.

## 2. BACKGROUND

### 2.1 Material Properties

In general, most biomaterials are orthotropic and to some degree all biomaterials exhibit viscoelasticity and strain rate dependency. Further, many types of tissue are also considered incompressible and fitted with a hyperelastic model because of their bulk modulus often highly exceeds their shear modulus due to their high water content which ranges from 5% to 85% depending on storage conditions (Livermore Software Technology Corporation, 2012; Humphrey, 2008; Suh, Woo, & Kim, 2005). It is for these reasons, and the numerous independent variables associated with tissues (health, moisture, mechanical adaptation, etc.), that biomaterials are conventionally modeled with nonlinear solvers using power models, polynomials, and constitutive rubber models.

#### 2.1.1 Orthotropic Nature

The orthotropic description of biomaterials and skin tissue stems from the variations in the cellular layers and the extracellular matrix in the transverse direction. The extracellular matrix (ECM) which makes up the largest portion of the dermis consists of highly hydrated proteoglycan proteins and fibrous support structures produced by fibroblast. Mechanically, the two primary molecules of interest which form the microfiber mesh in this composite material are type I collagen which provides the strength and rigidity of the material, and elastin which provides the material with elasticity (Schultz et al., 2005). As a result, at strain levels beneath 0.3 the elastin tends to provide most of the resistance to deformation and the elastic ability of skin to return to its original shape. While at higher strain levels of 0.3-0.6 collagen provides most

of the resistance to deformation by providing a much rigid support (Silver et al., 2001). This effect creates a non-linear J-shape stress-strain curve with small variations in stress as the load is transferred between collagen bundles (Edwards & Marks, 1995).

On a microscopic level both collagen and elastin molecules respectively cross-link to form collagen and elastin fibers (Schultz, Ladwig, & Wysocki, 2005). During strain, both fibers undergo an uncoiling similar to the behavior of rubber molecules causing a decrease in entropy and subsequent increase temperature (Humphrey, 2008; Courtney, 2005).

Anatomically, skin is a soft form of dense connective tissue and is composed of two heterogeneous layers; the outer epidermis and the inner dermis which lies superior to the fatty hypodermis as shown in Figure 2.1 (Belkoff & Haut, 2008; Samsam, 2012). In humans, this the skin thickness can range from 0.3-1.5mm thick (Brannon, 2007).

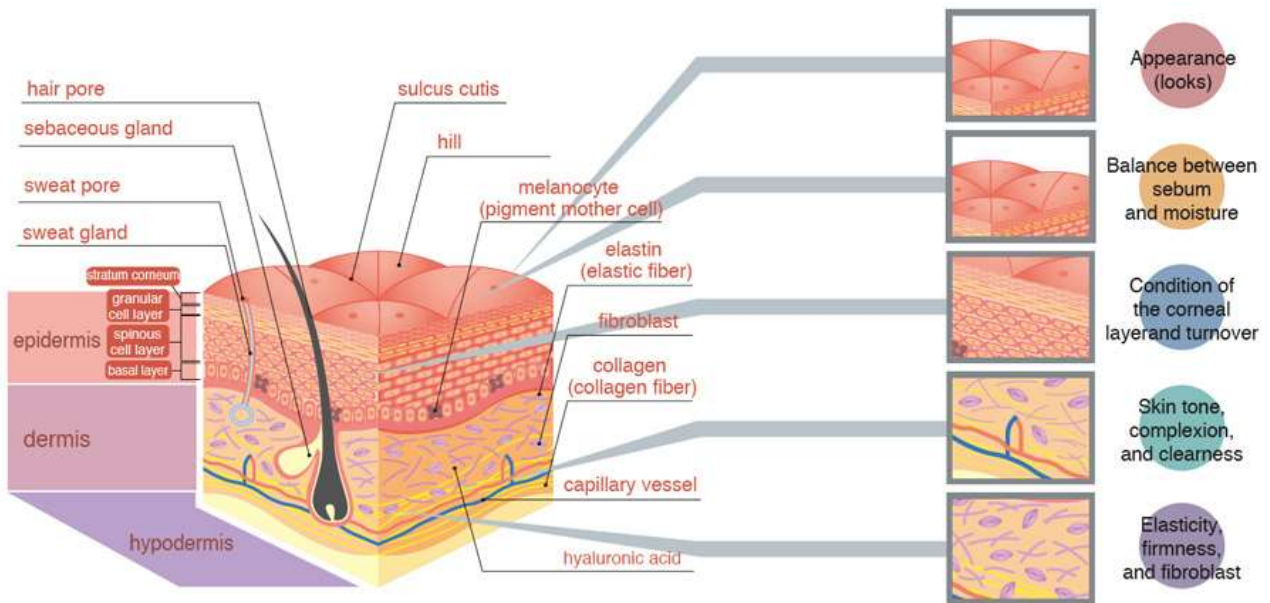


Figure 2.1: Skin Layer Diagram (Welch, Woloshin, and Schwartz, 2005)

The ECM and the properties of skin can also vary in the transverse direction depending on the anatomical location of the sample. The natural paths of these anisotropic variations can be traced in what are called relaxed tension lines and Langer lines (Borges, 1984). Tests have shown significantly higher strength in loads parallel to these paths of collagen and elastin fibrils located in the dermis (Khatyr et al., 2004).

### 2.1.2 Linear Viscosity

To describe the time-dependent properties of biomaterials, such as creep and stress-relaxation, constants for Newtonian viscoelasticity ( $\eta$ ) are often included in the constitutive model describing the stress relaxation at constant strain. In the case of linear viscosity, the viscous stress ( $\sigma_v$ ) is directly proportional to viscosity and strain rate( $\dot{\epsilon}$ ) in Equation 2.1.

$$\sigma_v = \eta \dot{\epsilon}$$

Eq. 2.1

When this viscous stress term is combined with Hooke's law for elastic stress ( $\sigma_E$ ) with Young's Modulus ( $E$ ) and strain ( $\epsilon$ ) in Equation 2.2, the stress-strain response of the system can be expressed as a series of springs and dashpots respectively representing the elastic and viscous properties of the material. The two most basic models that utilize these spring and dashpot elements are the Maxwell and Voigt or Kelvin models.

$$\sigma_E = E\epsilon$$

Eq. 2.2

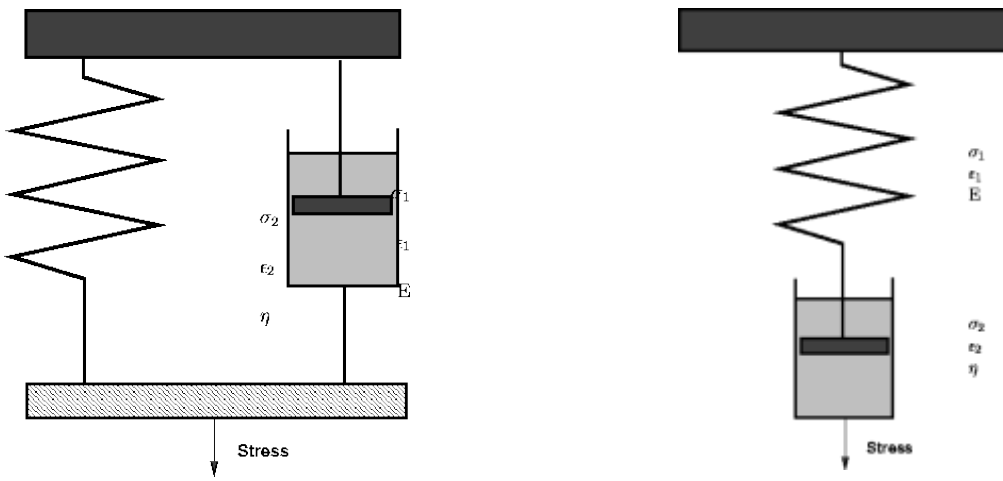


Figure 2.2: (left) Kelvin-Voigt Model and (right) Maxwell Model (Balmer, 2003)

In the case of the Maxwell model the spring and dashpot are in series, thus the stress on each element in the system is equal and the total strain in the system is a summation of both the viscous strain and elastic strain shown in Equation 2.4 and 2.3. Using equations 2.2, 2.3, and 2.4 it is possible to express the strain rate as a linear differential equation as shown in Equation 2.5 (Courtney, 2005).

$$\epsilon_{Total} = \epsilon_E + \epsilon_v \quad \text{Eq. 2.3}$$

$$\sigma_{Total} = \sigma_E = \sigma_v \quad \text{Eq. 2.4}$$

$$\dot{\epsilon}_{Maxwell} = \frac{1}{E} \frac{d\sigma}{dt} + \frac{\sigma}{\eta} \quad \text{Eq. 2.5}$$

When this is at a constant strain, as in the case of stress relaxation, the differential equation becomes solvable by separable variables as shown in Equation 2.6. In this equation it shows that stress decreases as a function of exponential decay that is dependent on elasticity and viscosity.

$$\frac{d\epsilon}{dt} = 0 \quad \sigma_{\text{Maxwell}} = E\epsilon_0 e^{-Et/\eta} = \sigma_0 e^{-Et/\eta} \quad \text{Eq. 2.6}$$

Under conditions of creep, or the strain over time at constant stress, the elastic modulus is eliminated from the Maxwell equation and strain rate, shown in Equation 2.7, is dependent on only the dashpot or viscosity element in the system.

$$\frac{d\sigma}{dt} = 0 \quad \dot{\epsilon}_{\text{Maxwell}} = \frac{\sigma}{\eta} \quad \text{Eq. 2.7}$$

Upon integration it is found that the strain is proportional to a function of elasticity, viscosity, and time. When this expression is isolated the time value is representative of the relaxation time ( $t_r$ ) of the material. In cases when the time is greater than the relaxation time the viscous properties dominant the system, where time is less than relaxation time it is instead the elastic properties that dominate the system (Balmer, 2003).

$$\epsilon_{\text{Maxwell}} = \sigma_0 \left( \frac{1}{E} + \frac{t}{\eta} \right) \quad \text{Eq. 2.8}$$

$$t_r = \frac{\eta}{E} \quad \text{Eq. 2.9}$$

In the Kelvin-Voigt model parallel elements can represent the total stress experienced by the system at a constant strain as described by Equation 2.10 and 2.11. As done previously with the Maxwell model, these equations can also be combined with Hooke's law to express strain rate as a linear differential equation shown by the general form of the Kelvin-Voigt model in Equation 2.12.

$$\epsilon_{\text{Total}} = \epsilon_E = \epsilon_v \quad \text{Eq. 2.10}$$

$$\sigma_{Total} = \sigma_E + \sigma_v$$

Eq. 2.11

$$\dot{\epsilon}_{Voigt} = E\dot{\epsilon} + \eta \frac{d\epsilon}{dt}$$

Eq. 2.12

At constant stress the Kelvin-Voigt equation can be solved to show strain as a function of the initial loading conditions, the material properties, and time (see Equation 2.13). In this case, the strain value determined from the stress loading conditions is slowly approached as the viscous resistance to strain contribution decays. Conversely, at conditions of constant strain the viscous term is removed from the Kelvin-Voigt model and Hooke's law for stress is reproduced in Equation 2.14.

$$\frac{d\sigma}{dt} = 0$$

$$\epsilon = \frac{\sigma_o}{E} \left( 1 - e^{-\frac{Et}{\eta}} \right)$$

Eq. 2.13

$$\frac{d\epsilon}{dt} = 0$$

$$\sigma = E\epsilon$$

Eq. 2.14

In practice the Kelvin-Voigt model performs better in modeling constant stress effects of creep where the Maxwell model is better at modeling the stress relaxation effects.

To compensate for the drawbacks present in each model, the Maxwell and Kelvin-Voigt model are often combined to create the standard linear solid model. The addition of this extra spring and dashpot enables the model to additionally capture the effects of viscoplasticity in which an initial offset of strain at  $t = 0$  and the permanent deformation that prevents the model from completely returning to zero strain (Courtney, 2005).

This standard linear solid model is sometimes further expanded into a general Maxwell-Wiechert Model viscoelasticity model in which the Maxwell elements have been infinitely repeated allowing numerical solvers to fit viscoelastic curves with a high degree of accuracy (Roylance, 2001).

### 2.1.3 Quasilinear Viscoelastic Relaxation

Because of the non-linear nature of the stress-strain curve for skin and biomaterials and their relatively large deformations, Fung first postulated that infinitesimal strain was inadequate to describing the behavior of the material. Instead, he used finite deformation to compare Piola-Kirchoff stress-deformation gradient to stress and found a near linear correlation between stiffness and stress for the 1-D behavior of mesentery tissue (Humphrey, 2008). This is shown in Equation 2.15 where Fung assumes that the stress of the material could be expressed as a convolution integral of the reduced relaxation function  $G(t)$  of the material and the elastic stress  $T^e(\lambda)$  in which the relaxation function is time dependent and the stress is dependent on the stretch ratio (Yoo et al., 2009).

$$\sigma = G(t) * T^e(\lambda) \quad \text{Eq. 2.15}$$

This reduced relaxation function shown in Equation 2.16 is the normalized relaxation stress of the material in reference to stress at the initial conditions after loading. Empirically, these values are found through a regression of Equation 2.16 (Wills & Picton, 1972). In this equation three independent exponential functions that is used to describe the decay of stress during stress relaxation testing.

$$G(t) = ae^{-bt} + ce^{-dt} + ge^{-ht} \quad \text{Eq. 2.16}$$

The stress function  $T(\lambda)$  is expressed through a 2-parameter exponential function of the stretch ratio of the material shown in Equation 2.18. Here the two constants A and B can be found through regression of the

$$\lambda = \frac{l}{l_o} = \epsilon + 1 \quad \text{Eq. 2.17}$$

$$T^e(\lambda) = A(e^{B\lambda} - 1) \quad \text{Eq. 2.18}$$

To expand upon this model for multi-axial loads, Fung used an energy storage function in the form of a hyperelastic constitutive equation. Since then, many other researchers have taken similar approaches by using well define hyperelasticity models such as Ogden, Yeoh, Rivlin-Mooney, and polynomial fits (Humphrey, 2008). While these basic rubber models reflect the incompressible nature of biomaterials (due to its high water content), modifications are often made to allow for anisotropic and time-dependent behavior (Natali et al., 2006).

#### 2.1.4 Hyperelasticity

A hyperelastic constitutive model is a function that closely describes the deformation response of nearly incompressible highly elastic materials such rubber which is commonly expressed with the Mooney-Rivlin hyperelastic model. According to the McGinty, the general expression of the Mooney-Rivlin model consist of the strain energy density function ( $W$ ) shown in Equation 2.19 and a summation of the invariants across the  $ij$ -matrix with their principle constant values. In applications of this model to rubber like and incompressible materials, the third invariant is eliminated as will be shown.

$$W = \sum_i \sum_j C_{ij} (I_1 - 3)^i (I_2 - 3)^j \quad \text{Eq. 2.19}$$

Unlike Cauchy stress tensor which utilize stress and differential strain, the Mooney-Rivlin tensor is composed of the stretch ratio expressed in Equation 2.17. When this three dimensional tensor is solved for the x, y, and z axis the eigenvalues, or invariants, shown in Equation 2.19 – 2.21, are composed of the principle stretch ratios.

$$I_1 = \lambda_1^2 + \lambda_2^2 + \lambda_3^2 \quad \text{Eq. 2.20}$$

$$I_2 = \lambda_1^2 \lambda_2^2 + \lambda_2^2 \lambda_3^2 + \lambda_1^2 \lambda_3^2 \quad \text{Eq. 2.21}$$

$$I_3 = \lambda_1^2 \lambda_2^2 \lambda_3^2 \quad \text{Eq. 2.22}$$

These three equations can be further reduced to the two equations 2.22 and 2.23 in the case of an incompressible material. This is because when the material is compressible the third invariant ( $I_3$ ) in Equation 2.25 becomes equal to one, hence the third stretch ratio in Equation 2.26 can be expressed as a function of the first two (McGinty, 2013).

$$I_1 = \lambda_1^2 + \lambda_2^2 + \frac{1}{\lambda_1^2 \lambda_3^2} \quad \text{Eq. 2.23}$$

$$I_2 = \lambda_1^2 \lambda_2^2 + \lambda_2^2 \lambda_3^2 + \lambda_1^2 \lambda_3^2 \quad \text{Eq. 2.24}$$

$$I_3 = 1 = \lambda_1 (\lambda_2)^2 \quad \text{Eq. 2.25}$$

$$\text{Which implies } \lambda_3^2 = \frac{1}{\lambda_1^2 \lambda_2^2} \quad \text{Eq. 2.26}$$

Next, when a load is only applied in one principle direction as in the case of uniaxial loading, the second stretch ratio ( $\lambda_2$ ) is equal to the third stretch ratio ( $\lambda_3$ ). Thus the invariants can be expressed as a function of only two principle relations and Equation 2.26 can be expressed as a direct relationship of the first and second stretch ratio (McGinty, 2013).

$$I_1 = \lambda_1^2 + \lambda_2^2 + \frac{1}{\lambda_1^2 \lambda_2^2} \quad \text{Eq. 2.27}$$

$$I_2 = \lambda_1^2 \lambda_2^2 + \frac{1}{\lambda_1^2} + \frac{1}{\lambda_2^2} \quad \text{Eq. 2.28}$$

$$\lambda_2^2 = \frac{1}{\lambda_1^2 \lambda_3^2} \text{ implies } \lambda_2 = 1/\sqrt{\lambda_1} \quad \text{Eq. 2.29}$$

To place these two invariants in the terms of a single stretch ratio, equation 2.29 can be back substituted into 2.28 and 2.29 to yield the two invariant expressions in Equation 2.30 and 2.31 (McGinty, 2013). Additionally, by substitution of these two new equations and equation 2.29 into the general expression for Mooney-Rivlin work for uniaxial loads, a relationship between engineering stress and the principle strain ratio can be expressed. This is shown in Equation \_ where stress in the remaining two directions of an uniaxial load is zero (Battles, 2010).

$$I_1 = \lambda_1^2 + \frac{1}{\lambda_1} \quad \text{Eq. 2.30}$$

$$I_2 = 2\lambda_1 + \frac{1}{\lambda_1^2} \quad \text{Eq. 2.31}$$

$$\sigma_E = \left(2C_{01} + \frac{2C_{10}}{\lambda}\right) \left(\lambda - \frac{1}{\lambda^2}\right) \quad \text{Eq. 2.32}$$

A further simplification of this model is often made by expressing the invariants constants as a ratio( $\alpha$ ) (Feng & Hallquist, 2012).

$$\alpha = \frac{C_{10}}{C_{01}} \quad \text{Eq. 2.33}$$

$$\sigma = 2C_1 \left( \lambda - \frac{1}{\lambda^2} \right) \left( 1 + \frac{\alpha}{\lambda} \right) \quad \text{Eq. 2.34}$$

The values of these constants are often found through a least squares regression of the stress strain response for a given material. In cases when a two parameter Mooney-Rivlin model is insufficient to capture the behavior of the material, most finite element solvers can expand the model to 3, 5, and 9 parameters expressions (Livermore Software Technology Corporation, 2012).

### **2.1.5 Natural Variation**

Although the focus of this paper is strictly limited to a study of the mechanical properties of skin, it is worth mentioning that tissue properties can vary due to both environmental testing conditions and the localized adaptation of the tissue; something Humphrey refers to as mechanobiology. In this type of adaptation, mechanical or chemical stimuli from neighboring cells and the ECM trigger new chemical pathways that alter which genes are expressed by the cell. Subsequently, significant variation in mechanical properties has been seen by a number of different researchers who have tested a variety of subjects and sample location for both human and porcine as shown in the table 2.1 (Lapeer et al., 2011; Tilleman et al., 2004; Jachomicz et al., 2007; Ankersen, 1999; Lim et al., 2011; Diridollou et al., 1998; Dunn and Silver, 1983; Krehbiel and Berfield, 2005; Edwards and Marks, 1995).

Table 2.1: Comparison of Skin Properties

Skin Type	Poisson's Ratio	Stress of failure (MPa)	Viscosity (kN·s/m <sup>2</sup> )	Ultimate Strain (%)	Young's Modulus (MPa)
Human Skin	0.4-0.5	15 – 30	37-277	35 – 115%	20 kPa – 57
Pig Skin	0.3	7 MPa (belly) 15 MPa (back)	-	25 - 118%	3.3-17 MPa

Further variation in the measured mechanical also comes from the testing procedures and storage conditions. For example, some researchers have performed experimentation in saline baths at a controlled temperature near the natural temperature of the human body, e.g. 37°C (Mansour et al., 1993). Additionally, because most samples are often frozen between uses, a concern in testing is whether or not this affects the material properties of the tissue. According to Foutz who had tested the effects of freezing on rat skin, there was no significant deviation in the loading response of the frozen samples and freshly excised samples; however, Foutz did find an increase in fracture strength in the samples that had been frozen, indicating that caution must be taken in applying any experimental results to in vivo conditions (Foutz et al., 1992).

## 2.2 Quasi-Static Cutting

Because of the widespread application of cutting tools in the food, medical, and production industries, numerous cutting models of mechanical blades have been developed to describe the relative sharpness of the cutting tool. While some of these models will go as far as to measure the microscopic width of the blade, nearly all models consider the required cutting force at specific depth to be a function of sharpness. Additionally, it has also been widely assumed that cutting blades, opposed to sawing blades, will produce a Mode I fracture shown in

Figure 2.3 during which a blade tip of infinitesimal width is expected to be met with negligible resistance force as it produces an opening in the material (McCarthy et al., 2010).

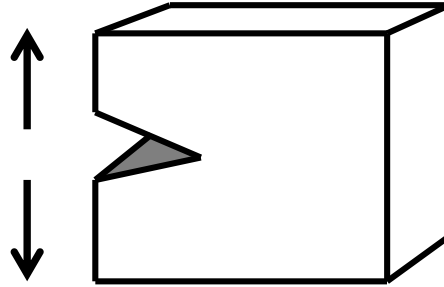


Figure 2.3: Mode I Fracture Opening

An example of such a model is the blade sharpness index (BSI) devised by McCarthy and colleagues, which relates the relative sharpness to the required cutting force. Under this model, it is assumed that with constant force, blade displacement is a function of sharpness. To measure this force ( $F$ ) in terms of initiation energy ( $E_i$ ), the load and deflection are integrated over the initial x-direction displacement ( $\delta_i$ ) as shown in the Equation 2.39.

$$E_i = \int_{\delta_i} F dx \quad \text{Eq. 2.35}$$

This integral equation is representative of the work required for propagation crack in which a new surface area is generated on opposite faces of the blade. When this energy is normalized ( $\bar{E}^*$ ), as done in Equation 2.40, with respect to both thickness  $t$  and mode I fracture toughness ( $J$ ) the value of the energy expenditure is dependent on only the relative sharpness of the blade and depth thereby providing a relative scale on which blade sharpness can be evaluated. Further to describe the so called BSI value of a blade at any arbitrary crack length, the normalized energy can be divided by the depth of the cut ( $\delta_i$ ) as shown in Equation 2.41. When this equation is

examined at a constant force it shows that cut depth is inversely proportional to BSI value which is to be expected for sharper blades (McCarthy, Hussey, & Gilchrist, 2007).

$$\bar{E}_i^* = \int_{\delta_i} \frac{Fdx}{tJ} \quad \text{Eq. 2.36}$$

$$BSI = \int_{\delta_i} \frac{Fdx}{\delta_i tJ} \quad \text{Eq. 2.37}$$

To find this relative fracture toughness ( $J$ ) or critical energy release rate of skin during cutting McCarthy used an energy based equation that was originally made by Doran and associates in similar soft tissue cutting experiments.

$$dX \cdot u + dU = d\Lambda + J \cdot dA + d\Gamma \quad \text{Eq. 2.38}$$

The left hand side of Doran's equation describes the differential of work ( $dX \cdot u$ ) of force ( $dX$ ) time's displacement ( $u$ ) done during cutting plus the stored strain energy due to tension of the surface( $dU$ ). Whereas the right hand side represents the differential stored strain energy ( $d\Lambda$ ) caused by the blade, the resistance to fracture per exposed area ( $J \cdot dA$ ) and the energy that is lost due to remote plastic flow ( $d\Gamma$ ). Solving for the resistance to fracture gives Equation 2.43 shown below (Doran et al., 2004) .

$$J = \frac{(X \cdot u - d\Lambda) + dU - d\Gamma}{dA} \quad \text{Eq. 2.39}$$

In McCarthy's modification to this equation, the initial sample is unstrained and it is assumed that with sufficiently sharp blades the remote deformation is minimized, thus the stored strain energy ( $dU$ ) and the remote plastic flow energy ( $d\Gamma$ ) are considered negligible and

removed from the equation. Next, McCarthy adds an additional variable  $P$  to account for energy lost to friction. To find this frictional energy, McCarthy records the load-displacement curve required to remove the blade from a precut sample. Hence, the net energy required to cut the material can be calculated by integration of the load-displacement curve minus the frictional energy (McCarthy et al., 2010; Doran et al., 2004).

$$J = \frac{\mathbf{u} \cdot (\mathbf{X} - \mathbf{P}) - d\Lambda}{dA} \quad \text{Eq. 2.40}$$

With use of their Blade Sharpness Index and finite element simulations, McCarthy's group found that blunt blades tend to have a fracture that propagates ahead of the material at a stress level near that of the tensile strength of the material. In contrast, quickly loaded and relatively sharp blades tend to have the fracture tip that lies adjacent to blade and approach a constant force during cutting (McCarthy et al., 2010).

In general skin is assumed to have a viscoelastic deformation mode because of its time dependent ability to store energy (Doran et al., 2004; Dunn and Silver, 1983; Khatyr et al., 2004); however, it is implied that during quasi-static cutting that the time-dependent behavior becomes less significant. In such cases like McCarthy's testing on polyurethane, this relaxation has been completely ignored by their choice to model polyurethane as an incompressible hyperelastic Ogden material in their finite element analysis (McCarthy et al., 2007).

### 2.3 Existing Hemostatic Tools

Hemostatic tools are cutting instruments that cause the surrounding tissue to coagulate, thereby preventing blood loss. This is usually accomplished by causing a localized cauterization

of the surrounding tissue with the application of heated probes, electric currents, lasers, or ultrasonic vibration.

In a comparison between ultrasonic cutting and cauterizing tools, ultrasonic loads tend to cause less thermal damage to the surrounding tissue because coagulation is initiated through mechanical vibration instead of direct conduction of heat. The dynamic load combined with the heat generated from friction causes localized denaturing of proteins and effectively breaks down cellular walls to produce a hemostasis effect to stop bleeding (Mason and Lorimer, 2002; Sinha and Gallagher, 2003).

Additionally, because the high velocity sinusoidal motion of the blade tip, the fracture of the tissue occurs at a higher strain rate than during cutting with traditional scalpels (Mason and Lorimer, 2002; Zahn, Schneider, and Rohm, 2006). During surgical applications the frequency ( $f$ ) of the blade typically lies between 55kHz to 100kHz with an average blade amplitude ( $Y_0$ ) of 100  $\mu\text{m}$ . Because the blade tip velocity is a sinusoidal function shown in Equation 2.37 the peak blade velocity can be calculated to be somewhere between 350 and 630 m/s (Polyakov et al., 1974).

$$V_{blad}(t) = Y_0 2\pi f \cos(2\pi f t) \quad \text{Eq. 2.41}$$

The power requirements during ultrasonic cutting are determined by the interaction of the oscillating blade with the target material. Because most ultrasonic systems implement a feedback control system to maintain a target frequency and a specific blade amplitude different materials require different power inputs to maintain to achieve the desired cutting or welding affect. To

approximate this value as the work done on the material in Equation 2.38, the target velocity of the blade is multiplied by the force applied to the tool during cutting. (Branson, 2012).

$$P \approx F \times \omega Y_0 \quad \text{Eq. 2.42}$$

In contrast, electrosurgery cauterizes tissue by applying a high frequency electric current directly on the target surface. Because the human nervous system is responsive from 0-1000 Hz, electrosurgery usually has an operating frequency of at 200 kHz to 5 MHz. This frequency range is sufficiently high that the electro-tool can be operated safely without stopping the patient's heart. Additionally, there are two branches of electrosurgery; monopolar and bipolar. In bipolar surgery, an electric charge is passed between two opposing poles each located in a tip of a specialized forceps. However, during monopolar surgery the electric current is passed from the scalpel or needle directly through the patient to a large return electrode pad in contact with their body. (Schellart , 2005).

During electrosurgery the coagulation and cutting rate is determined by power and frequency of the current delivered to the tissue. This power requirement is calculated by making the assumption that both density ( $\rho_w$ ) and heat capacity ( $C_w$ ) of soft tissues approximately equal to that of water (Schellart , 2005). With this assumption, the known temperature of coagulation, a desired coagulation rate, and an approximation of the mass of the tissue in the electrified forceps, Equation 2.40 can be used to determine the necessary power requirements for the electro-cauterization.

$$P = \frac{m \times C_w \times T}{time} \quad \text{Eq. 2.43}$$

Additionally, this input current can be further manipulated by the surgeon depending on the procedure. When cutting is desired the input current is applied as a continuous sinusoidal current, while coagulation alone is achieved by applying an intermediate current so that hemostasis takes place instead of complete tissue desiccation (Schellart , 2005).

With fewer accidental burns and less smoke during cutting, ultrasonic tools are often considered to be a safer alternative to electrosurgery. Nevertheless, there exists some controversy about whether ultrasonic cutting is in fact less damaging to tissue than electrosurgical procedures. In a study by Homayounfar and coworkers, who examined the coagulation of freshly excised porcine skin, it was found that the necrosis present in tissue samples was consistently deeper in ultrasonic cutting than that caused by a monopolar electrosurgical tool (Homayounfar et al., 2012). Yet, in a study by Sinha and Gallagher on the recovery time of the oral mucosa in guinea pigs, it was found that traditional blades and ultrasonic blades, had a much faster recovery than monopolar surgery, bipolar surgery, and laser surgery (Sinha and Gallagher , 2003). A plausible explanation for this discrepancy is that, albeit the cellular death is greater, the damage from an ultrasonic blade only effects a localized area, while the thermal damage caused by an electric current goes to a greater depth than indicated by cellular necrosis.

## **2.4 Existing Biospy Tools**

Currently there are three main types of biopsies that a dermatologist might choose from in the testing of melanoma: shave biopsy, circular punch biopsy, and elliptical cut biopsy. The shave biopsy (Figure 2.4) consists of running a curved razor or scalpel along the epidermis or skin surface to remove a superficial layer of the skin. The traditional punch biopsy (Figure 2.5)

consists of a circular blade being driven into the skin and rotated to cut a circle around the targeted region. The elliptical incision biopsy (Figure 2.6) involves a skilled surgeon using a scalpel to make an elliptical cut around the targeted region. The final decision of the technique used will ultimately fall to the dermatologist and the patient, however, the elliptical biopsy has been credited with achieving the best incision depth and it is also the easiest to suture. The drawbacks to this technique are that the elliptical biopsy requires the most time and equipment, and in some cases additional scarring may occur (MacFarlane and Raphini, 2010).



Figure 2.4: Shave Biopsy (MacFarlane & Raphini, 2010)      Figure 2.5: Punch Biopsy (MacFarlane & Raphini, 2010)



Figure 2.6: Excisional Biopsy (MacFarlane & Raphini, 2010)

Provided this increasing demand for dermal biopsies, new elliptical biopsy punches have been developed with the goal of improving the quality of biopsies. While the current prototype designs still require a puncture force too high for patient use, it is believed that ultrasonic cutting tools could potentially reduce this required force making the procedure more feasible.

## 2.5 New Biopsy Tools

In conjunction with Noble Corporation (Orlando, FL), preliminary research on biopsy tools and scalepels was carried out at UCF to determine the performance of various blade designs. In the same manner as Weiner and colleagues, forces versus displacement curves were recorded and analyzed (Weiner et al., 2009). The types of surgical tools under analysis consisted of a 12mm flat elliptical punch (Figure 2.8), a 12mm rounded elliptical punch (Figure 2.9), a number 15 scalpel (Figure 2.10), a 7.5mm rounded elliptical punch (Figure 2.11), a 12mm serrated rounded elliptical punch (Figure 2.12), and number 15C scalpel.

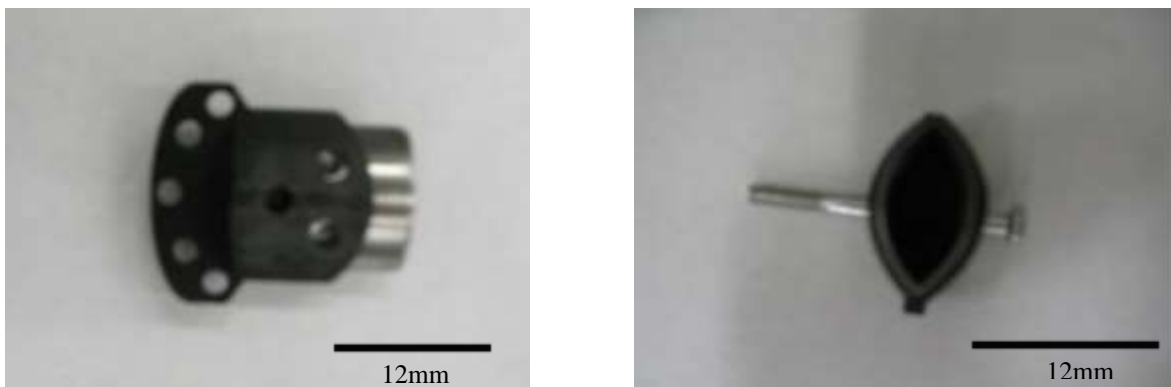


Figure 2.7: Flat 12mm Elliptical Punch side (left) inside (right)



Figure 2.8: Rounded 12mm Elliptical Punch (left) Number 15 Scalpel in Mount (right)

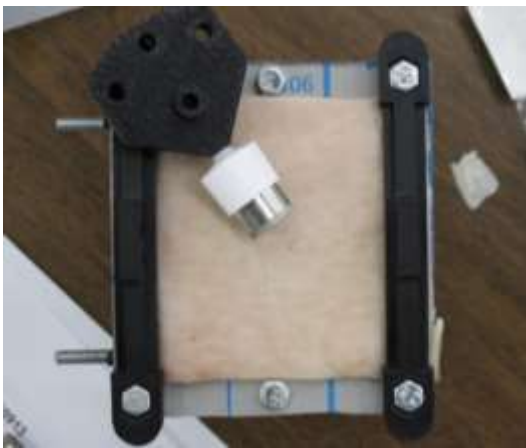


Figure 2.9: Flat 7.5mm Punch (left) Serrated 12mm Punch (right)

The simplest test conducted on these instruments was a traditional vertical (90 degree) puncture shown in Figure 2.10. As one might expect, the required cutting force was shown to be proportional to the surface area being cut; a comparison of 100N (22.5 lbs) for the larger 12mm punch and 40N (9.0 lbs) for the smaller 7.5mm punch. However, there is some uncertainty associated with these results as required force is measured from the sudden drop on the load-displacement plots (Figure 2.11 - 2.12) before the blade began cutting into the support mat.

Additional testing of the serrated blade showed much less required force, however, testing with both the serrated blade and rounded blade was not considered successful as they had failed to completely cut out the skin in the desired elliptical pattern.



Figure 2.10: Vertical (90°) Puncture (left) Angled (56°) Puncture (right)

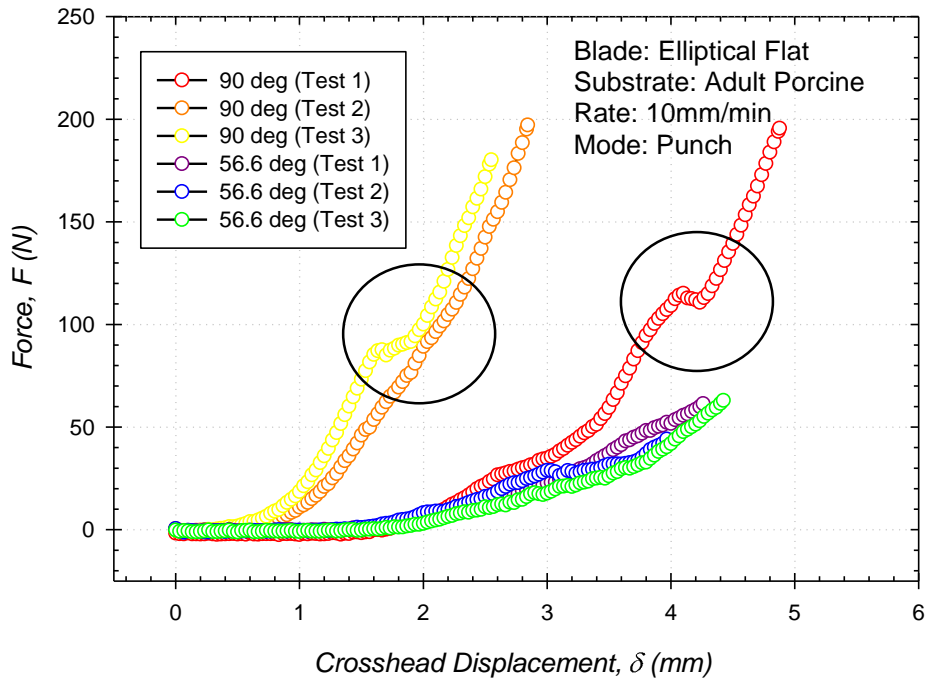


Figure 2.11: Elliptical 12mm Flat Bladed Punch Loads

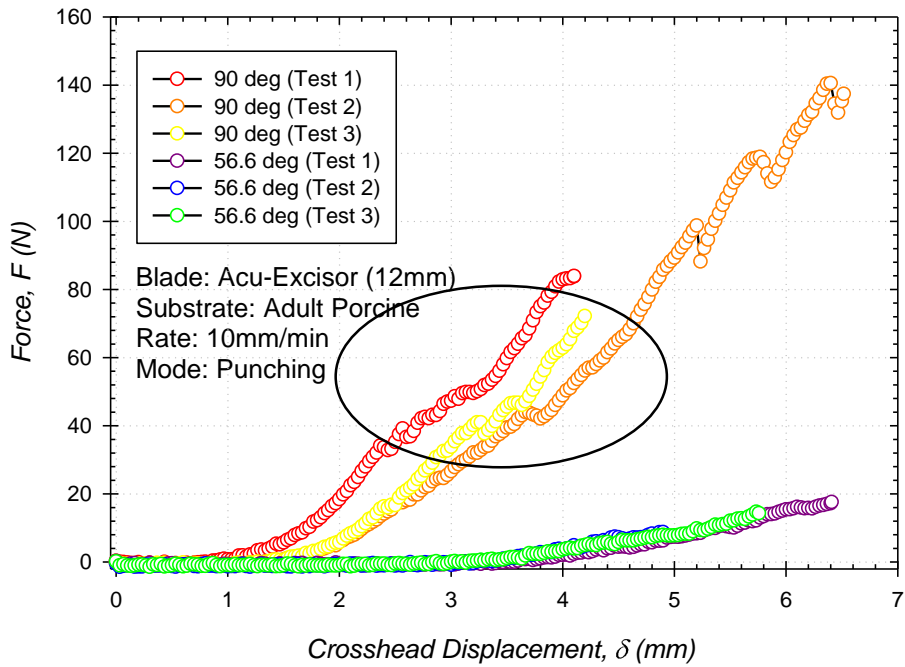


Figure 2.12: Elliptical 7.5mm Punch Loads

The second motion studied was an angled puncture with the tip of the elliptical blade followed by a rocking motion. Each motion of cutting was studied separately by first testing an angled puncture with the corner of the tool by rotating blade 56 degrees and then by testing the required force to continue the cut by rotating the blade. The angled punch entry required much less force than the vertical punch, approximately 20 N (4.5lb) for the rounded blade, 15N (3lb) for the flat blade, and 9N (2lb) for the serrated blade. However, the rocking motion (Figure 2.14) of the biopsy punches proved to be inconclusive as none of the blades successfully cut out the desired elliptical shape due to folding of the skin as the blade rolled across it.

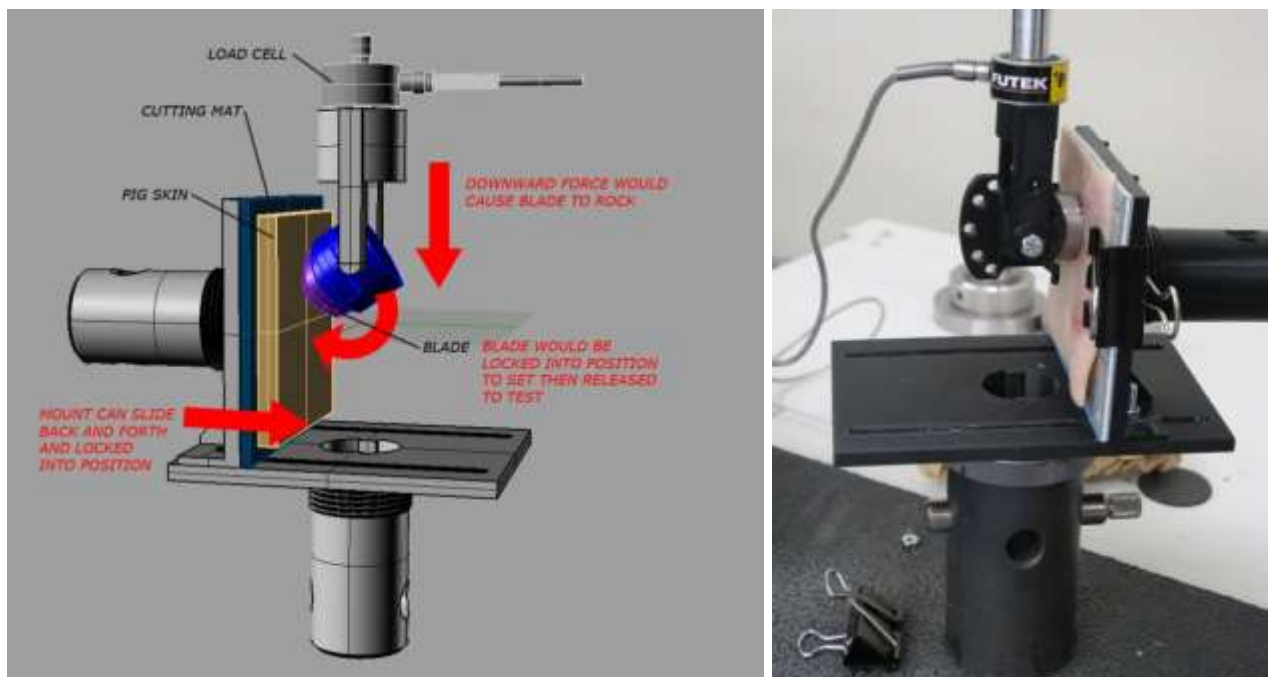


Figure 2.13: Elliptical Blade Rocking

During the testing of the 15 and 15C scalpels force was measured for the two stages of cutting in surgery; the force for the initial penetration with the blade tip, and the required force of the blade to continue cutting with the blade at a 45 to 90 degree angle to the skin (Figure 2.14). It was found that the initial penetration force with the number 15 scalpel was about 1 N (0.2lb) at the tip and when angled 45 degrees so the body of the blade made the initial cut it instead required about 4N (0.8lb). Conversely, the 15C scalpel only required about 1 N (0.2lb) to make the initial incision with either the body or the tip of the blade.



Figure 2.14: #15 Scalpel Slicing Test (left) #15 Scalpel Puncture Test (right)

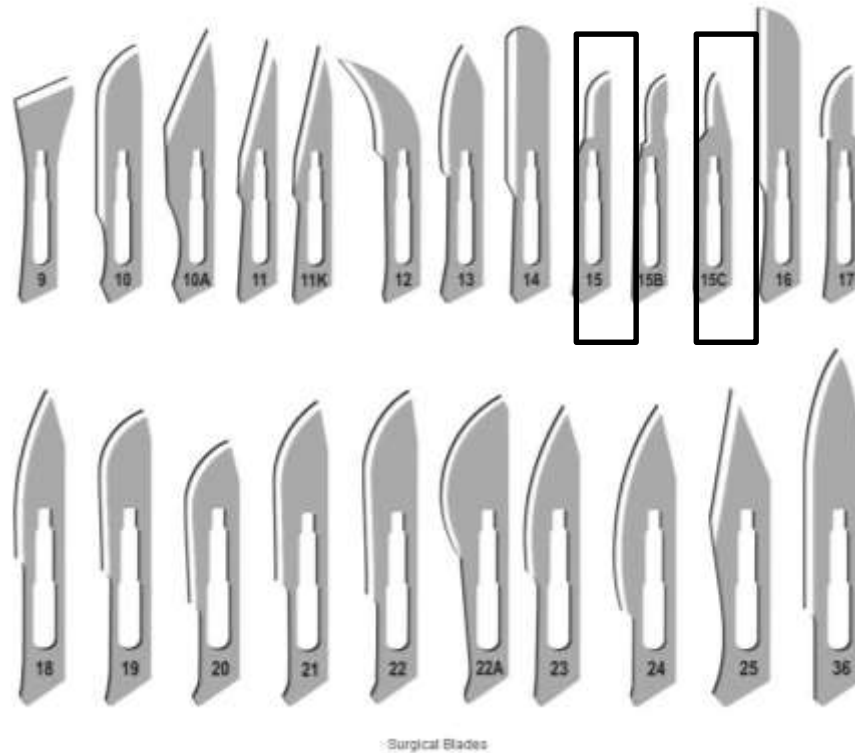


Figure 2.15: Scalpel Blade Profiles (Lokseva Surgicals)

When the number 15 scalpel was tested for slicing, it was found that about 1 N (0.22 lbs) require for cutting in both the 45 and 90 degree orientation. Whereas the number 15C scalpel required about 1.6 N (1.36 lbs) for its 90 degree cut and 0.6 N (0.13) for its 45 degree cut.

From these experiments it was determined that the tested elliptical biopsy punch designed Noble Corporation requires too much force to create an elliptical excision during minor surgery with only localized anesthesia. The cause of this excessive load is the relatively high amount of skin to blade surface area that the elliptical biopsy has in comparison to traditional scalpels. To calculate the amount of force required in the design of future surgical tools the fracture toughness of the target material during cutting must be known. However, because the material

properties of skin, and biomaterials in general, is poorly understood it has led to the need for a material characterization study which this thesis will focus on.

### 3. EXPERIMENTAL APPROACH

Although the ultimate goal of this study is the development of a material model that describes the cutting of living human tissue, it is currently not feasible to perform the necessary mechanical testing and experiments with human tissue or with in vivo conditions. As this often the case, an acceptable skin substitute that has been repeatedly used in the area of biomaterials is porcine skin (Shergold et al., 2006; Zak, Kuropka et al., 2011). Thus the outcome of these experiments will be an experimental approach to model the mechanical properties of skin with limited data and resources.

To capture these properties and the response of skin during surgical cutting, three types of experiments were implemented. First, tensile testing was performed as it represents the most basic experiments of mechanics of materials and offers the greatest insight into the mechanical deformation mode. Next, stress relaxation test were completed at 5%, 10%, and 15% strain to describe the time dependent behavior of skin. Finally, the force displacement response during cutting with a number 11 scalpel blade was measured to determine the fracture toughness of the skin during practical applications. From this experimental data a constitutive model will later be developed and verified in a finite element analysis to show the correlation between the material properties and the testing procedure.

#### **3.1 Candidate Material**

The porcine skin used in these experiments was obtained from Hopkins Meat Packing (Sanford, FL) where the skin was frozen and stored at -23°C for a period of 4 weeks prior to testing. The skin samples were cut laterally across the anterior, or belly, of the swine in long

strips measuring up to 30 inches long. Tensile specimens were the cut from these strips in a superior to inferior orientation as shown with the dog-bone stencil in Figure 3.1. Due to the processing of the material, some sections of the skin did have small uniformly spaced abrasions on the external surface of the dermis seen in Figure 3.2. Subsequently, these sections were avoided in testing.

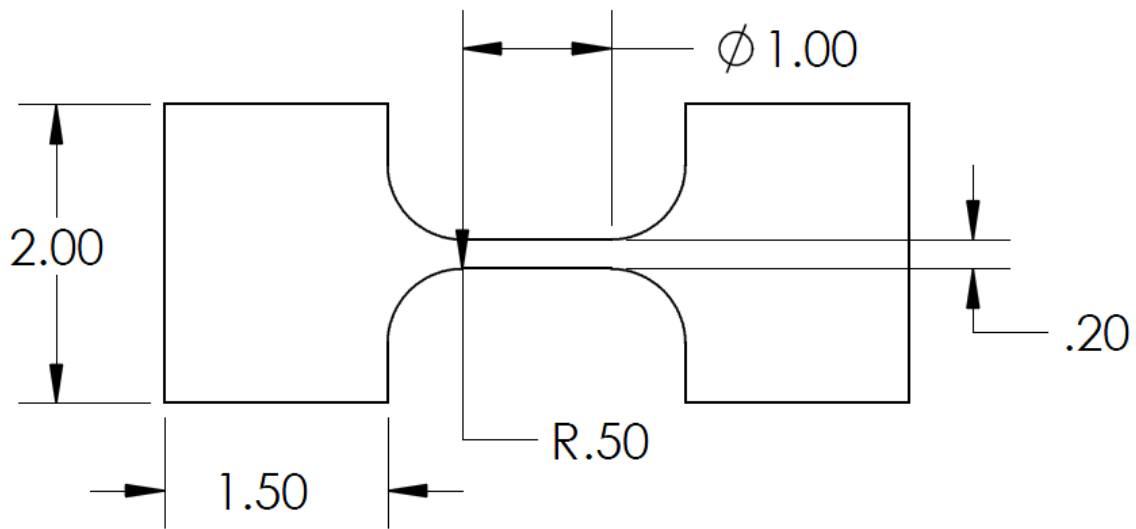


Figure 3.1: Dog-bone Skin Specimen (inches)



Figure 3.2: Frozen Skin Sample with Dog-bone Stencil

### 3.2 Specimen Preparation

The skin samples were stored off campus in a freezer maintained at the maximum freezer setting of approximately  $-18^{\circ}\text{C}$  and allowed to air warm to room temperature over a period of one hour before testing. Because of the viscoelastic nature of the material, it was found that the best time to cut the specimens with the designed stencil was about 15 minutes into this thawing time. At this time the skin was warm enough to cut with a steel handled X-acto knife and cutting

board, and yet rigid enough that the stencil could be followed with a fair degree of accuracy. As a safety precaution latex gloves were worn during this procedure.

Due to the strong history-dependence of viscoelastic solids, it was also necessary to apply a cyclic preconditioning to each specimen to provide a constant stress history during the relaxation and tensile testing (Belkoff & Haut, 2008; Carew et al., 2004). This preconditioning consisted of five tensile loading cycles of 0.05-0.15 MPa being applied to each sample prior to testing at a rate of 50 mm/min and data acquisition rate of 6 Hz as shown in Figure 3.2. These load values are similar to the values used in previous studies on the effects of stress, strain, and load preconditioning in tissue mechanics (Liu and Yeung, 2008; Zemanek et al., 2009). In this case, the stress preload is preferred to compensate in the variation in cross-section area among the hand cut specimens. When the precondition was applied, the stress-strain curve shifted to the right and the hysteresis between each loads cycle decreased with each additional load until preload strain behavior becomes nearly elastic; or pseudoelastic (Humphrey, 2008; Liu & Yeung, 2008). This behavior is shown in Figure 3.3 and Figure 3.4 where each cycle is plotted over the course of a complete preload sequence respectively against time and strain measured by the video extensometer.

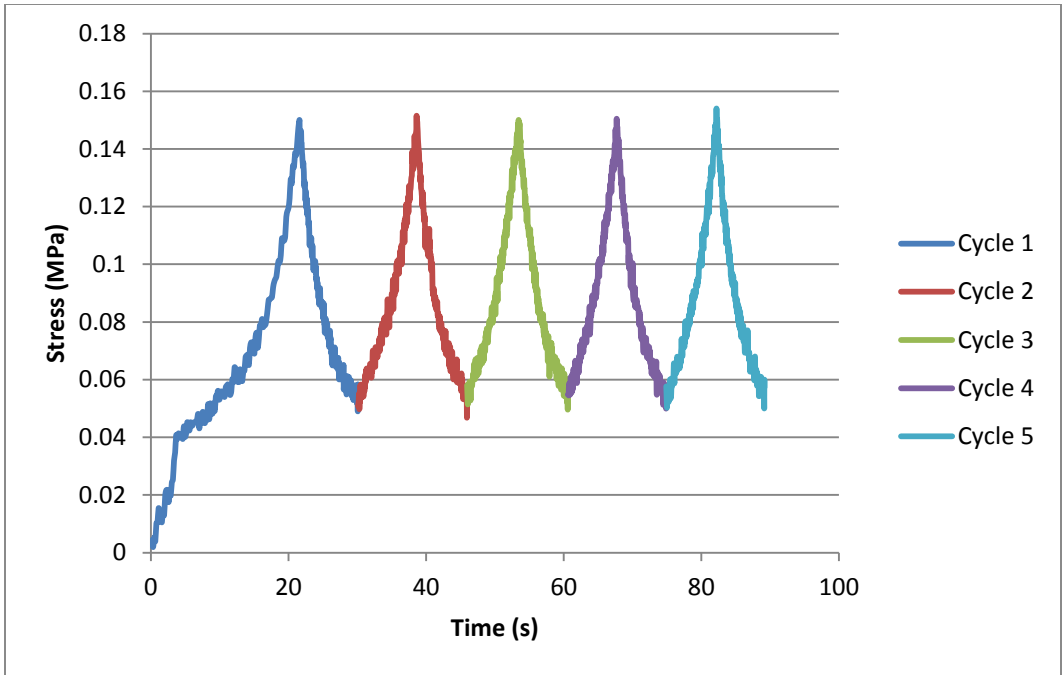


Figure 3.3: General Preconditioning Cycles

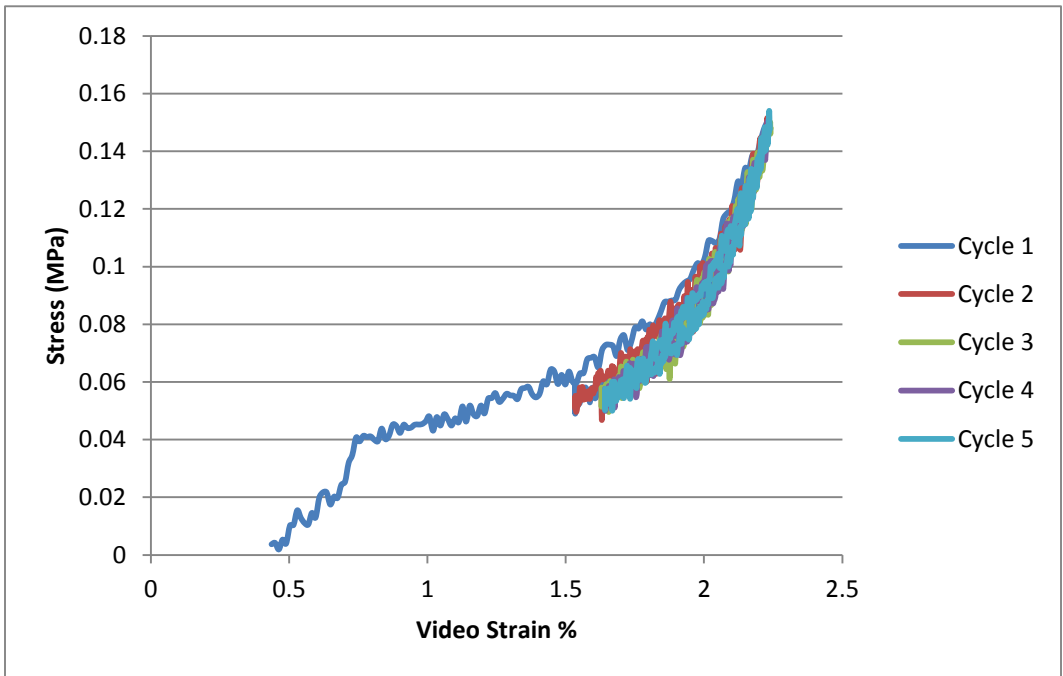


Figure 3.4: General Preconditioning Cycles

### 3.3 Trial testing

Because there is limited standardization in the mechanical testing of biological materials, some effort was needed to develop the skin fixture, specimen configuration, and loading conditions leading to repeatable results. One of the main obstacles in this endeavor was high water content of the skin which prevents conventional clamps from having sufficient friction to hold the specimen during tensile testing. After a trial and error approach, it was found that most effective grips consisted of 2 inch extruded saw-tooth staggered clamps that were printed from a three-dimensional printer (Makerbot Replicator2) with a 45% infill of polyacetic acid (PLA) plastic as shown in Figure 3.3 & 3.4.



Figure 3.5: Saw-tooth PLA Clamps

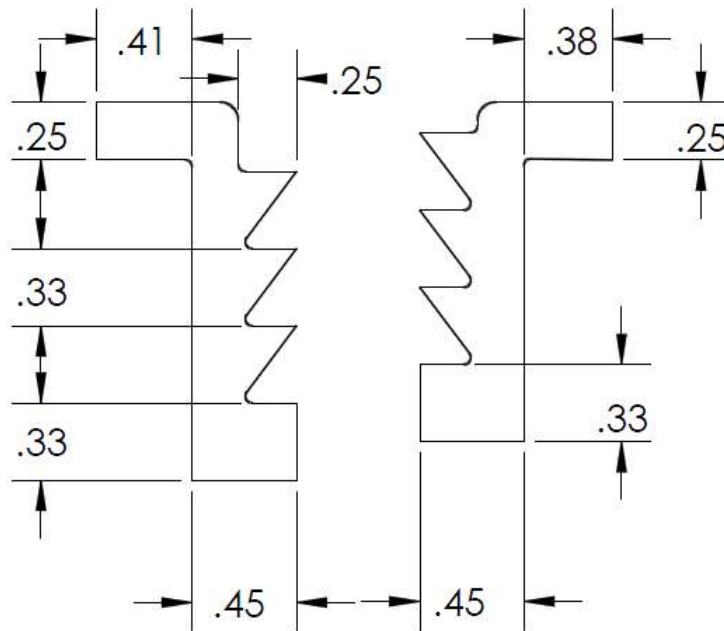


Figure 3.6: Sketch of Saw-Tooth Clamps (inches)

The second obstacle encountered during the development of this testing procedure was to ensure a repeatable specimen failure within the marked gauge length. Because of the stress concentration of the skin at the clamp teeth, the initial straight specimens had a tendency to tear, slip, or peel their way out of the clamp. To correct this, a dog-bone profile shown in Figure 3.5 was developed to provide a 0.5 inch fillet for a 1 inch gauge length with a 5mm width similar to dimensions used by Zak (Zak et al., 2011). To create the dog-bone specimens, a stencil was designed in SolidWorks and printed in PLA plastic to provide a guide in cutting the pig skin to the exact dimensions of the specimen. Additionally, because the epidermis and dermis layers varied in thickness from 5-8mm, it was decided to use skin that had been uniformly trimmed at the butcher to a 3-4mm thickness.

One final note on the skin condition is that all the experiments described in this paper are performed in air and room temperature. A more advance technique that is sometimes used in the tensile testing of biomaterials is to submerge the sample in a saline baths at controlled temperatures during testing to mimic the hydration of skin found in vivo conditions (Mansour et al., 1993).

### **3.4 Tensile Testing**

Uniaxial tensile test were run on these hand-cut dog-bone shaped specimens with the goal of establishing a hyperelastic model based on nonlinear curve fitting. During the setup of the tensile testing a 1 inch gauge length was marked with an Expo dry erase marker and the cross section area was measured (shown in Figure 3.6). The skin was then locked in place with the PLA printed clamps, the cyclic precondition was applied to the specimen, and then the gauge length and cross section area were re-measured.

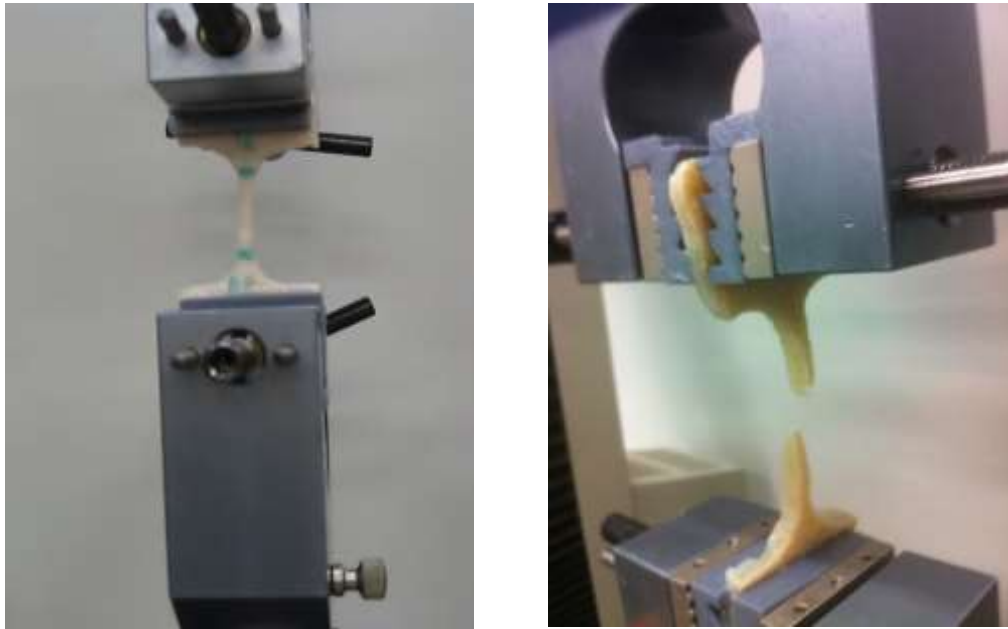


Figure 3.7: Tensile Testing Before (left) and After (right)

Next, the specimen was once again loaded back to 0.15 MPa and the tensile test was administered until fracture with the crosshead displacement rate of the load frame set to 50mm/min with a data acquisition rate of 10 Hz. The gauge strain was measured using both strain relative to the cross head displacement and strain from a frame to frame analysis of the test recorded by a 8-megapixel Cannon PowerShot digital video extensometer. Due to the geometry of the dog-bone specimens it is expected that the crosshead displacement would provide a large overestimate of the actual strain of the gauge length. Thus, the aid of a video extensometer will minimize this error. Finally after completing the test, the cross section area and gauge length of the specimen were measured and recorded for the third time with the digital caliper.

### **3.5 Stress Relaxation**

To describe the time dependent viscous properties of the skin, stress relaxation was measured using the previously described hand cut dog-bone specimens at 5%, 10%, and 15% of their gauge length in a similar testing protocol outlined by Liu and Yeung. Similar to the tensile testing, a one inch gauge length was marked on the dog-bone specimens with an Expo dry erase marker and the cross section area of the specimen was measured. Next, each sample was preloaded with the cyclic preconditioning described in section 3.2, measured, and then re-loaded back to the 0.15 MPa. Finally, the specimens was extended to the desired strain level at a rate of 50 mm / min and held at this strain for a period of 20 minutes during which stress relaxation was measured with data acquisition rate of 6 Hz. Although there is no standard time for the relaxation testing of skin, initial trials indicated that stress levels appear to approach an asymptote in several minutes, and following Liu's example, it was assumed that at 20 minutes the material could be considered fully relaxed.

### **3.6 Cutting**

The force required to cut skin with a scalpel blade was measured by constructing a rig capable of holding the skin while the movement of the blade and reaction force was measured by the MTS universal load frame equipped with a similar blade attachment as used in the experiments that were performed with the Noble Engineering Incorporation. The blade used during these tests was a straight edge number 11 Harvel scalpel that was set up to cut at a rate of 50 mm / min. The MTS attachment shown in Figure 3.7 was designed a snap in clip for the scalpel blade and angled at a 13 degree slope such that the blade edge was perpendicular with the

skin during cutting. Further, the scalpel attachment was equipped with an adjustable locking wheel with 60 degree intervals and should other angles be desired. The entire design was printed with PLA plastic using a Makerbot Replicator 2 printer and attached to the load frame with ¼-28 carriage bolt and crosshead adaptor.

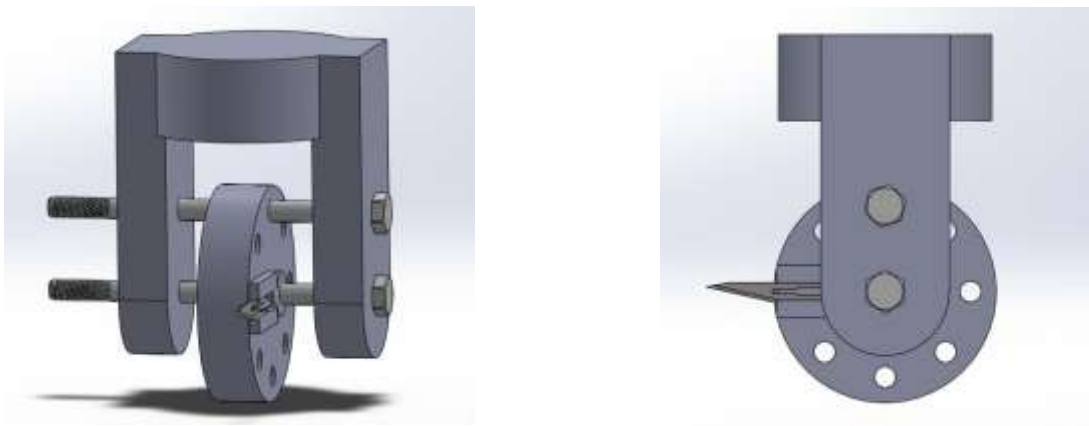


Figure 3.8: Scalpel Mount CAD Isometric & Side View

Unlike the previous experiments with Noble Engineering Incorporated, the rig used in these cutting experiments was designed to suspend the skin between two vertical posts to allow the blade to cut through only the skin and avoid any supporting surfaces as shown in Figure 3.8. The rig was constructed from six 1 ft extruded aluminum 80/20 framing equipped with a two 2"x4" plates used to hold the skin during tests via binder clamps. Each skin specimen was cut to a 2"x4" rectangle to provide the scalpel blade with a 2 inch length of skin to cut between the 80/20 supports.



Figure 3.9: Cutting Assembly

## 4. DATA ANALYSIS

### 4.1 Pre-Load Testing

The cyclic preloading used to establish a pseudoelastic state and similar strain history is shown below in Figure 4.1 and Figure 4.2. During this preconditioning protocol a preload stress of 0.1-0.15MPa was applied for a five cycle duration to each of dogbone skin specimen for the subsequent tensile and stress relaxation experiments. Because the video strain of the preloading being measured by visual inspection, there is a greater degree of uncertainty than the gauge strain from the cross head's displacement. Nevertheless, when these two measurement techniques are compared it can be inferred that measurement from the crosshead alone provides an overestimate of strain due to a deformation of the sample outside the gauge length.

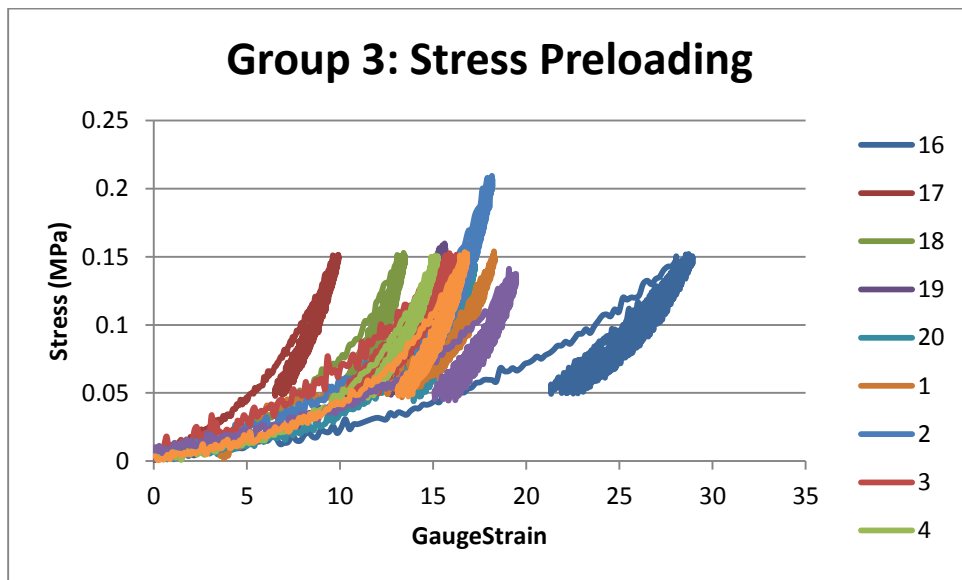


Figure 4.1: Gauge Strain Cyclic Preload

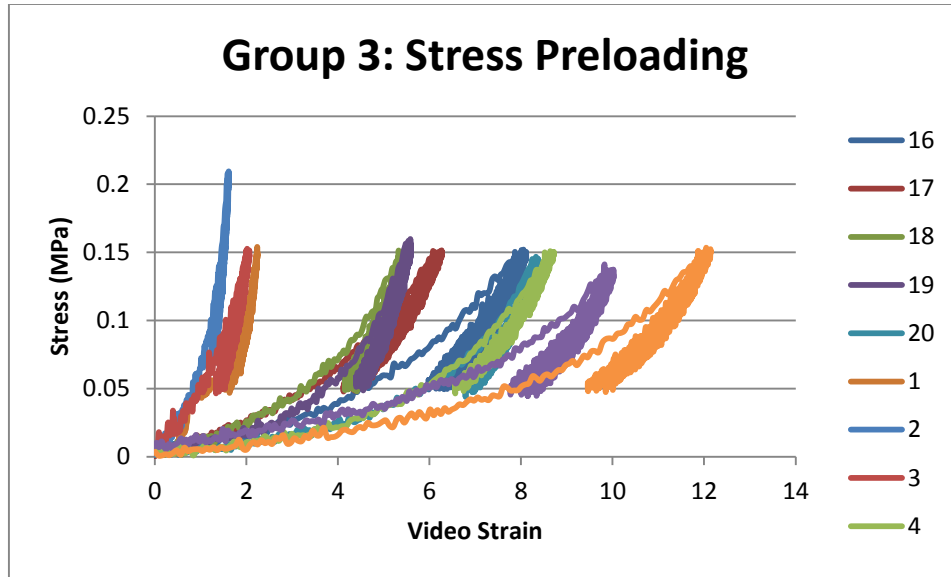


Figure 4.2: Video Strain Cyclic Preload

Further, because of the large variation of gauge strain and the presence of hysteresis in each load cycle, it can be understood why biomaterials are often considered highly variable and strain history dependent. These effects are shown particular well by an analysis of the energy density lost in the loading and unloading of sample of number 1 of the 5% stress relaxation group (shown in Figure 3.2) with the derived equation 4.3. This equation is derived from Equation 4.1 where the integral of force to displacement is equal to half the pressure ( $\sigma A$ ) times displacement( $\epsilon l_0$ ).

In the experiment, the amount of energy lost to hysteresis is calculated by subtracting the loading area of the force displacement curve from the unloading curve. In doing so, the material appears to approach a state of pseudo-elasticity as the hysteresis seems reach a lower limit by the third cycle; summarized in Table 2 (Hibbeler, 2011).

$$U = \int F dx = \frac{1}{2} \sigma A \epsilon l_0 \quad \text{Eq. 4.1}$$

$$dU = \frac{1}{2} \sigma \epsilon dV \quad \text{Eq. 4.2}$$

$$\frac{dU}{dV} = \rho_e = \frac{1}{2} \sigma \epsilon \quad \text{Eq. 4.3}$$

Table 4.1: Hysteresis Effects of Sample 1

Cycle	1	2	3	4	5
Initial Strain	0.00	12.53	13.31	13.51	13.41
Final Strain	12.53	13.31	13.51	13.41	13.62
$\Delta$ Strain	18.21	18.21	18.30	18.22	18.27
Energy Density Lost (J/m <sup>3</sup> )	2.18E+05	4.46E+04	2.20E+04	1.22E+04	1.99E+04

## 4.2 Tensile Testing

The uniaxial tensile stress response of the cyclically preconditioned skin was measured using the MTS testing frame load cell while the strain response was again measured with both the video extensometer and crosshead displacement relative to the measured gauge length. From comparison of these two experimental techniques shown in Figure 4.3 and Figure 4.4, it appears that the video extensometer did in fact provide a much more consistent value for strain at failure; approximately 25.66% with a standard deviation of ( $\pm 3.78$ )% in comparison to 87.50 ( $\pm 19.64$ ) % gauge length strain. The average strength at failure was recorded to be 11.61 ( $\pm 2.45$ ) MPa with an ultimate strength of 12.05( $\pm 2.67$ ) MPa.

Table 4.2: Tensile Group

Specimen No.	Percent Reduction Area	Post Gauge Strain	Video Strain	Ultimate Stress (MPa)	Strength (MPa)
16	3.3	10.1	30.0	9.7	9.3
17	16.4	6.4	23.9	11.5	11.4
18	15.2	3.9	23.1	15.0	14.2

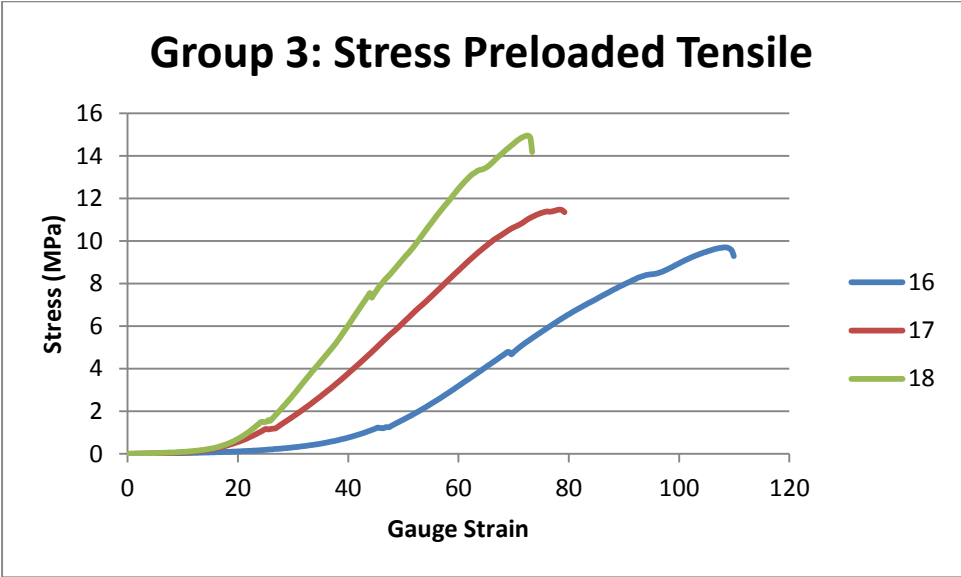


Figure 4.3: Tensile Test with Scaled Gauge Strain

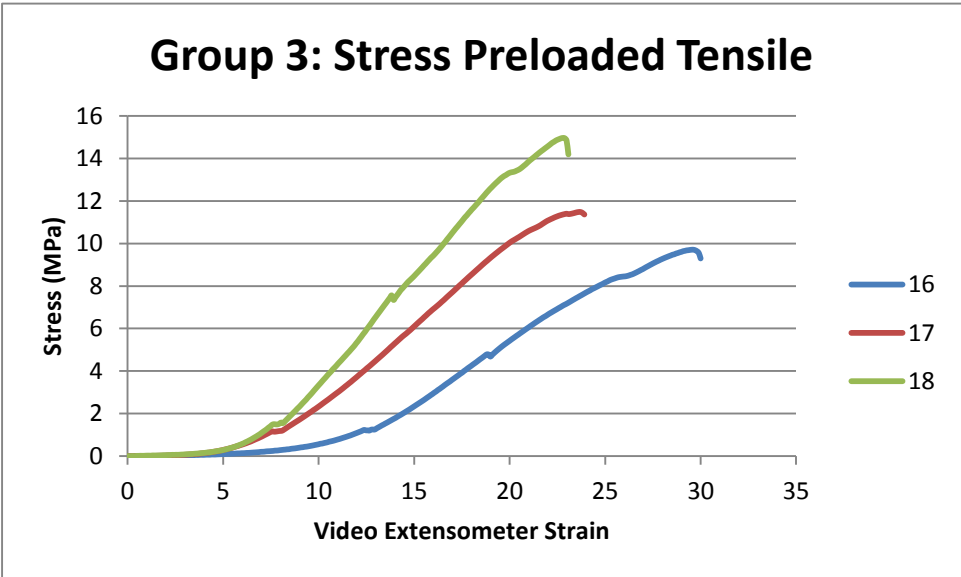


Figure 4.4: Tensile Test with Video Extensometer

Due to the highly non-linear nature of the biomaterial an exponential toe-region precedes the linear elastic region of the stress-strain curve occurs during the initial loading of the material. Once this region is removed in each respectively sample, a better approximation of the final strain of the material is found to be about 15% as shown in the toe-offset video extension data in Figure 4.5 & 4.6.

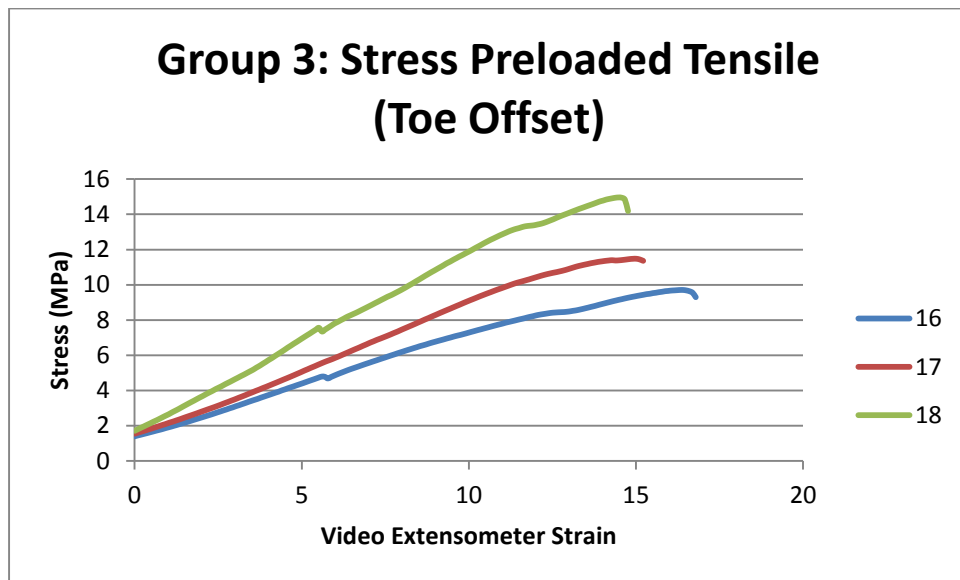


Figure 4.5: Toe Offset Video Extension Tensile Data

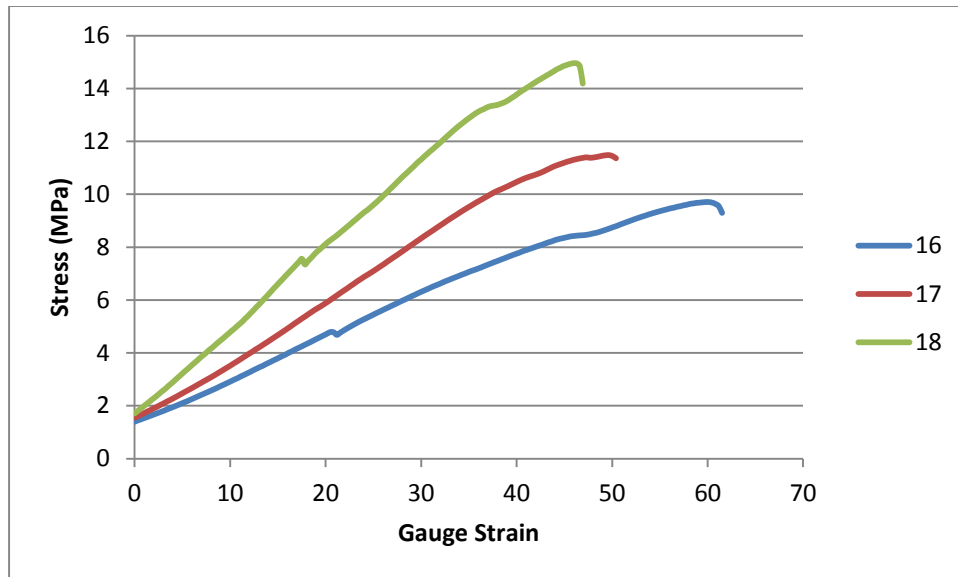


Figure 4.6: Toe Offset Gauge Strain Tensile Data

With the removal of this toe-region and the assumption that sample number 17 is representative of the linear stress-strain portion of the material response can be fitted to approximate the Young's Modulus of skin to be about 77 MPa with the video data and 23 MPa with gauge data (Figure 4.7 & 4.8).

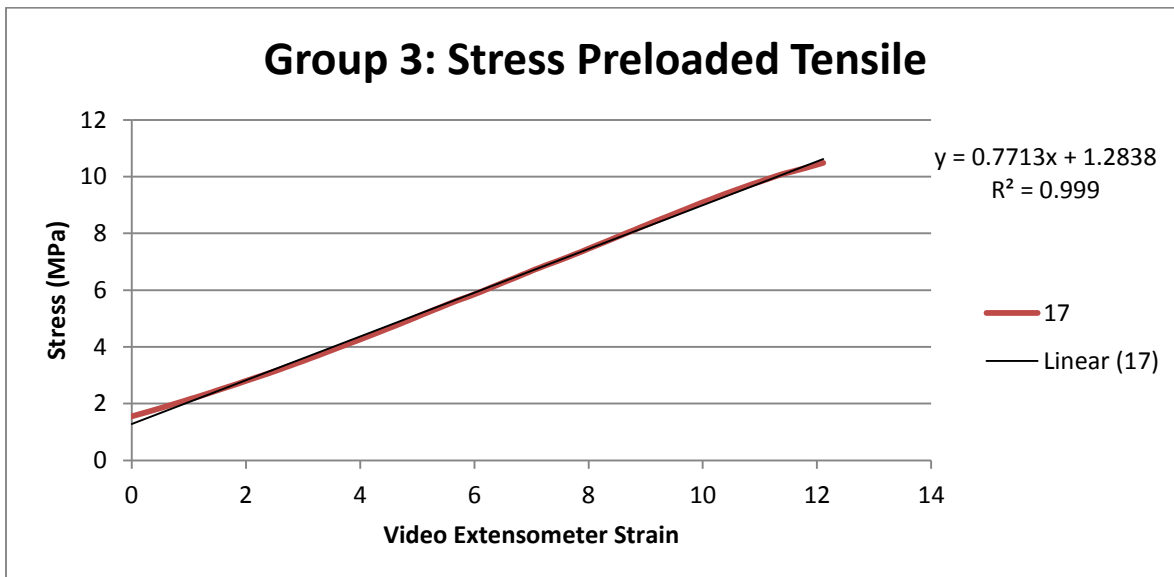


Figure 4.7: Sample 17 Video Strain Linear Region Fit

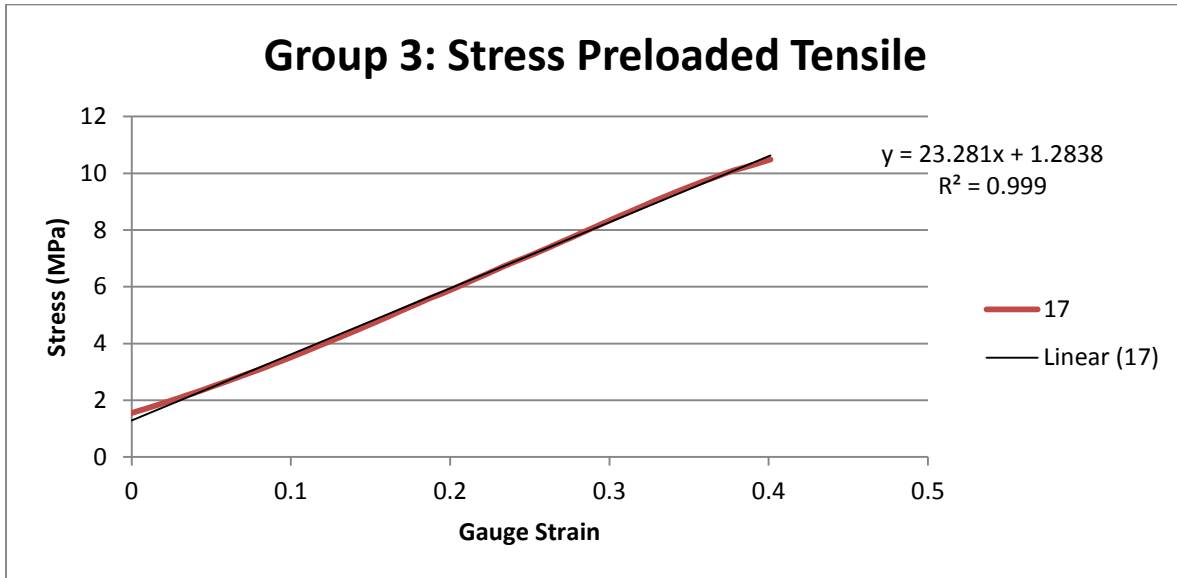


Figure 4.8: Sample 17 Gauge Strain Linear Region Fit

Further, upon a non-linear analysis of sample number 17 as a hyperelastic material it is shown that the stress-strain behavior of skin is well best fitted by either a polynomial model or the Mooney Rivlin rubber constitutive model shown in Figure 4.8-4.14.

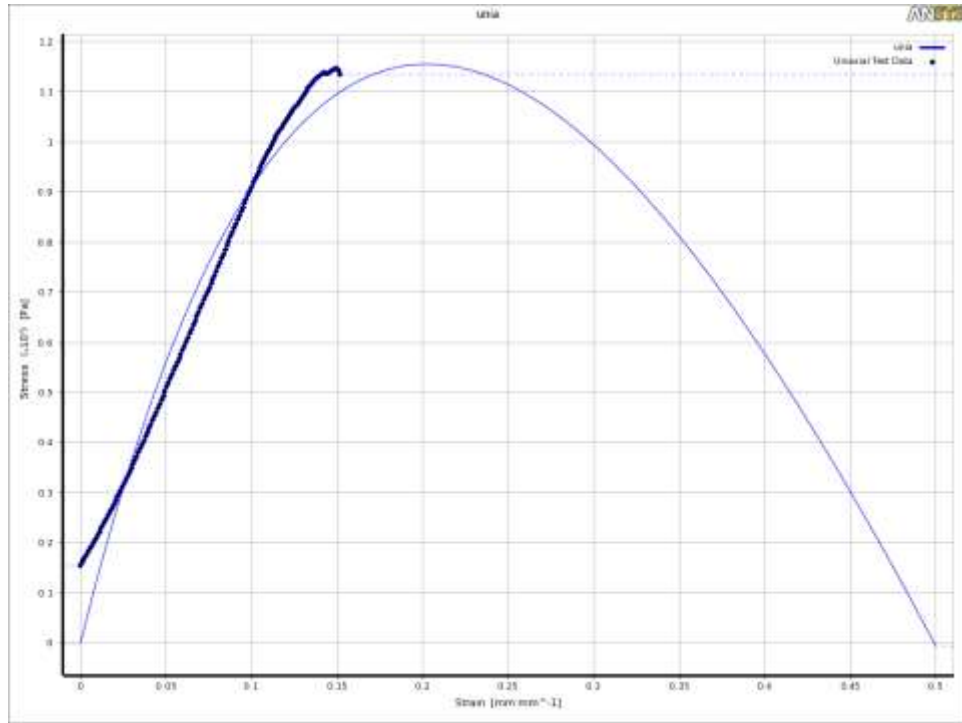


Figure 4.9: 2-Parameter Mooney Rivlin Fit

Table 4.3: Variables of 2-Parameter Mooney Rivlin Fit

Material Constant C01	68771070.92 Pa
Material Constant C10	-45876747.49 Pa
Residual	6.02

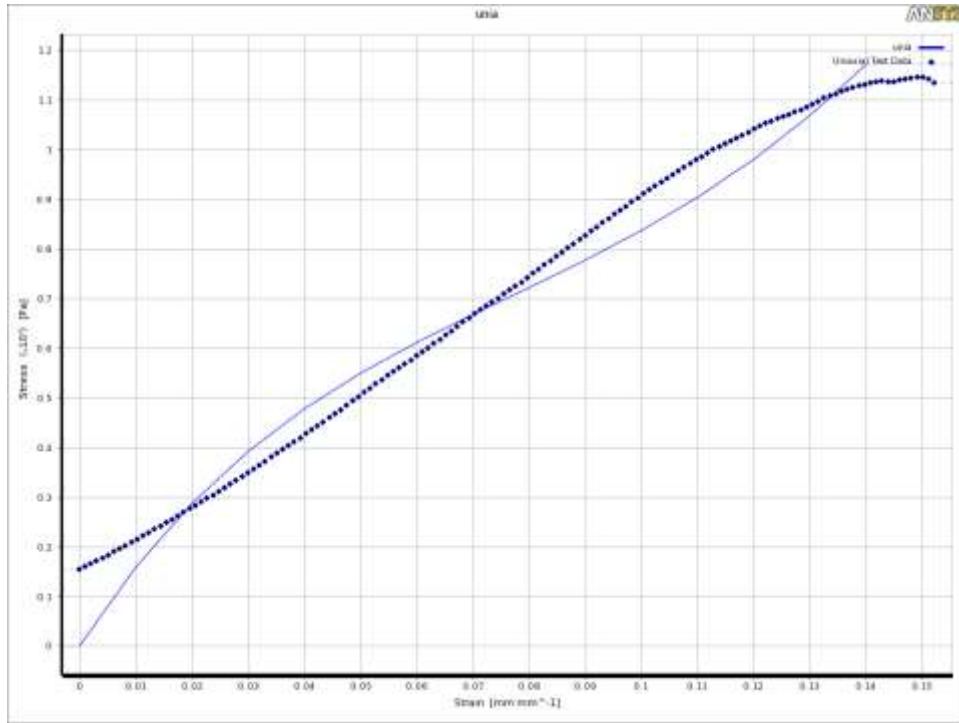


Figure 4.10: 3-Parameter Mooney Rivlin Fit

Table 4.4: Variables of 3-Parameter Mooney Rivlin Fit

Material Constant C01	270219489.7 Pa
Material Constant C10	-240968903.1 Pa
Material Constant C11	204086206.5 Pa
Residual	5.01

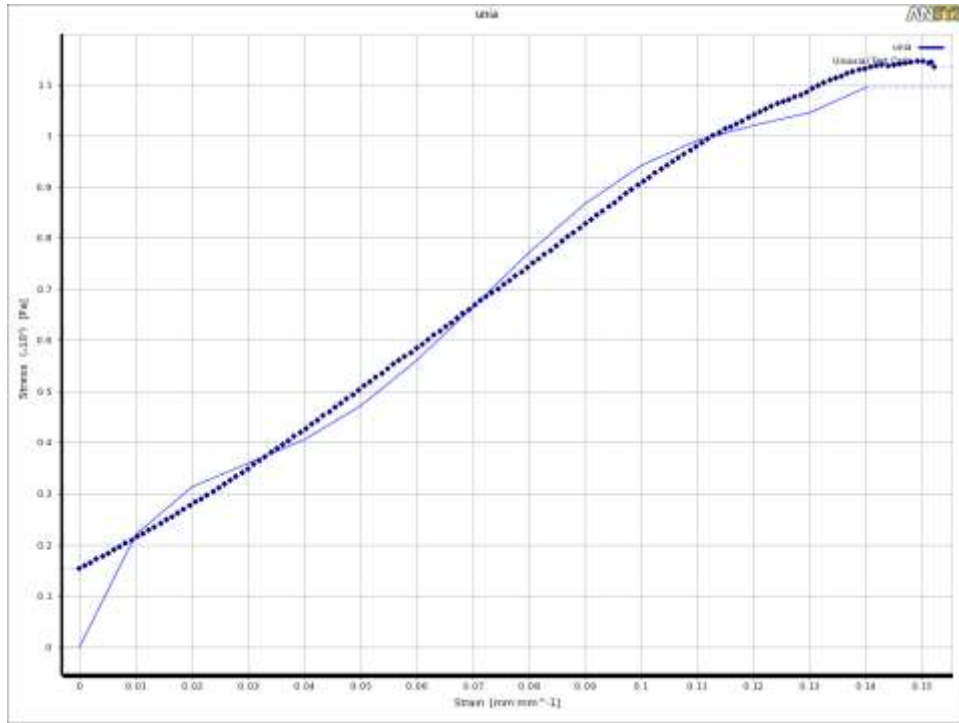


Figure 4.11: 5-Parameter Mooney Rivlin Fit

Table 4.5: Variables of 5-Parameter Mooney Rivlin Fit

Material Constant C01	2016856179.51 Pa
Material Constant C02	243376895450.02 Pa
Material Constant C10	-1963307781.84 Pa
Material Constant C11	-419633881603.39 Pa
Material Constant C20	182620608294.59 Pa
Residual	2.89

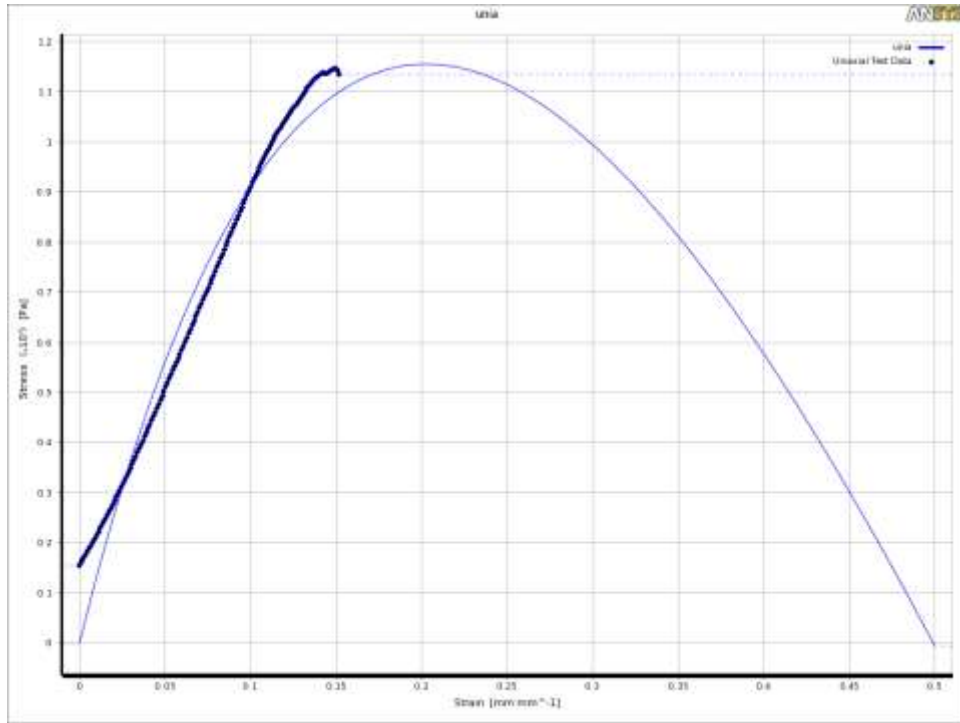


Figure 4.12: 1<sup>st</sup> Order Polynomial Fit

Table 4.6: Variables of 1<sup>st</sup> Order Polynomial Fit

Material Constant C01	68771071 Pa
Material Constant C10	-45876747 Pa
Residual	6.02

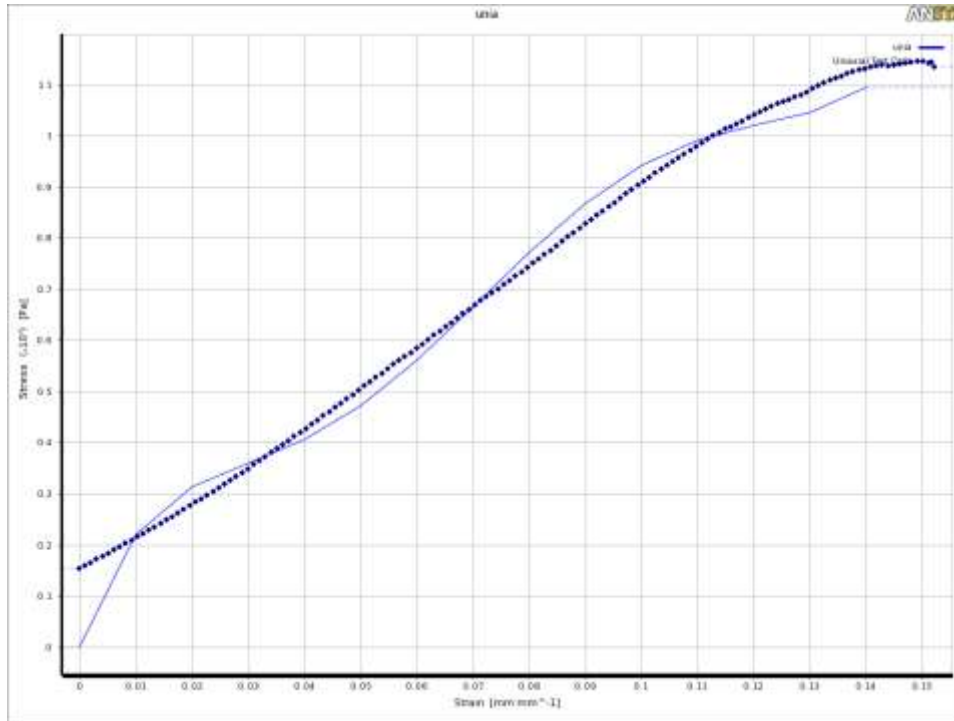


Figure 4.13: 2<sup>nd</sup> Order Polynomial Fit

Table 4.7: Variables of 2<sup>nd</sup> Order Polynomial Fit

Material Constant C01	2016856108.19 Pa
Material Constant C02	243376878889.59 Pa
Material Constant C10	-1963307711.31 Pa
Material Constant C11	-419633852388.38 Pa
Material Constant C20	182620595333.56 Pa
Residual	2.89

### 4.3 Relaxation Testing

The stress relaxation testing used to determine the time dependent properties of viscoelastic relaxation of skin was determined at 5%, 10%, and 15% of the gauge length strain over a period of 20 minutes as shown in Figure 4.15-4.17. To better show the stress values of interest, and the relaxation of the material, the normalized end stress values are tabulated in Table 4-10 through 4-12.

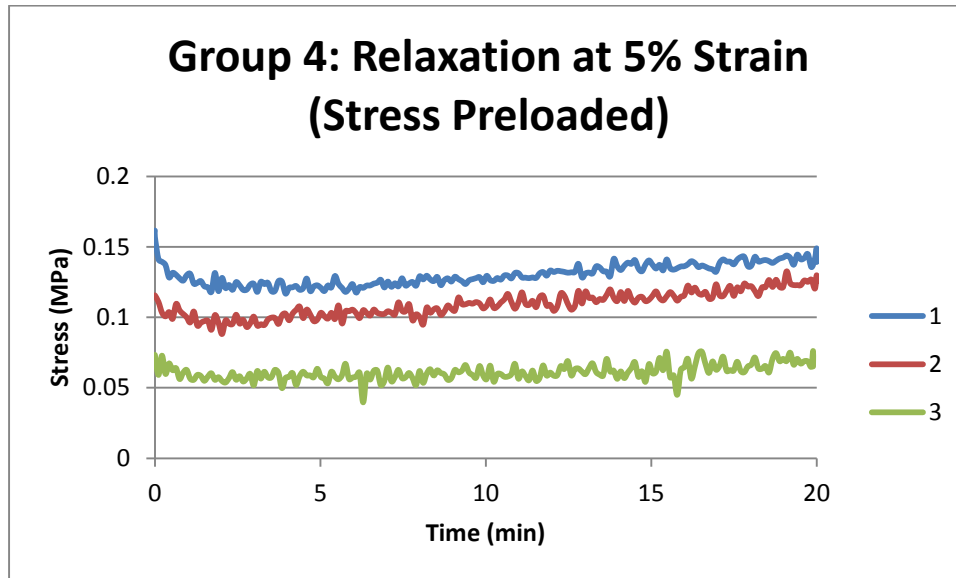


Figure 4.14: Skin Relaxation at Constant 5% Strain

Table 4.8: Summary of Data for Relaxation of Skin of Skin of Skin at Constant 5% Strain

Sample	Initial Stress (MPa)	Min Stress (MPa)	Time at Min Stress (min)	End Stress (MPa)	End Stress Normalized (MPa)
1	0.16	0.12	3.95	0.14	0.86
2	0.12	0.09	2.03	0.13	1.09
3	0.07	0.04	6.29	0.07	0.89

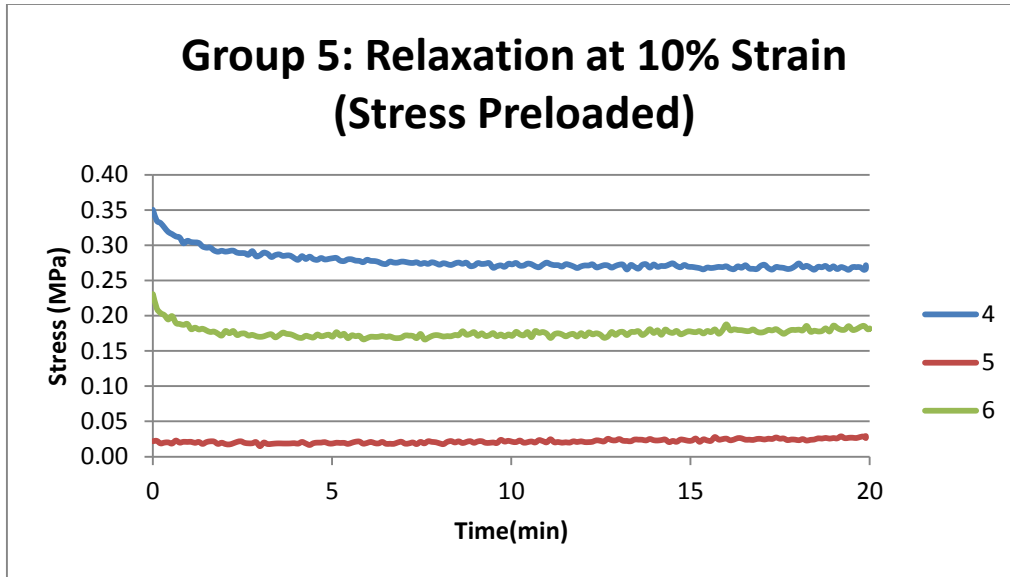


Figure 4.15: Skin Relaxation at Constant 10% Strain

Table 4.9: Summary of Data for Relaxation of Skin of Skin of Skin at Constant 10% Strain

Sample	Initial Stress (MPa)	Min Stress (MPa)	Time at Min Stress (min)	End Stress (MPa)	End Stress Normalized (MPa)
4	0.35	0.27	19.84	0.27	0.78
5	0.02	0.01	2.99	0.03	1.34
6	0.23	0.17	7.57	0.18	0.79

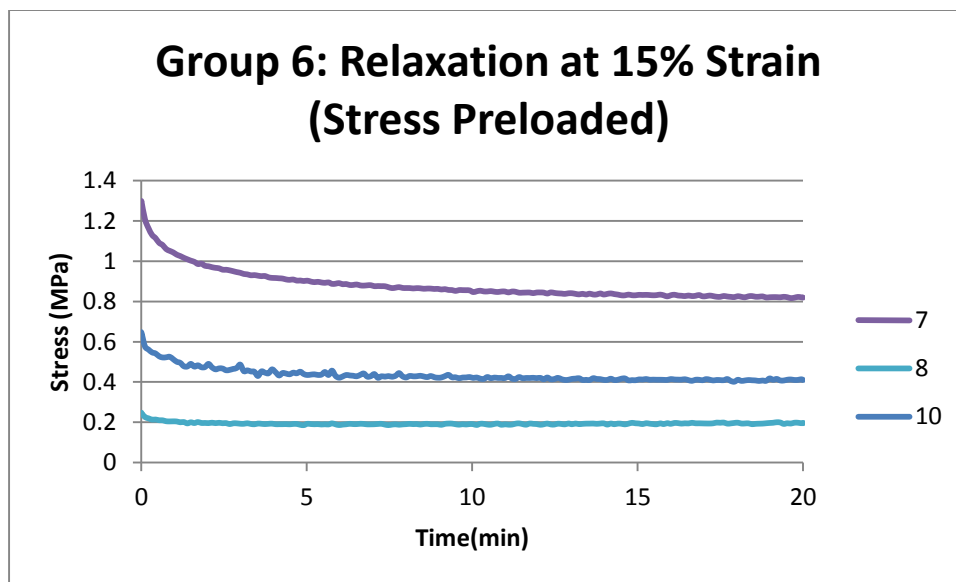


Figure 4.16: Skin Relaxation at Constant 15% Strain

Table 4.10: Summary of Data for Relaxation of Skin of Skin of Skin at Constant 15% Strain

Sample	Initial Stress (MPa)	Min Stress (MPa)	Time at Min Stress (min)	End Stress (MPa)	End Stress Normalized (MPa)
7	1.30	0.82	19.63	0.82	0.63
8	0.25	0.19	4.91	0.20	0.79
10	0.62	0.40	17.92	0.41	0.66

In an effort to describe a general relaxation model for skin, samples 1, 4, and 7 are considered to be best representative of the stress relaxation at of 5%, 10%, and 15% gauge strain. As expected, during the relaxation of skin, the tensile stress approaches a minimum; however, after reaching this minimum the stress begins to increase as time elapses resulting in a somewhat elevated normalized end stress that is particularly apparent at lower strain levels. A possible explanation for this tensing is the drying of the samples as they are exposed to air. Thus, to characterize the viscous relaxation of skin at 5%, 10%, and 15%, it is assumed that samples 1, 4, and 7 are representative of the material as they showed the lowest normalized end stress (plotted in Figure 4.18) in each respective group and provided the smoothest trend data.

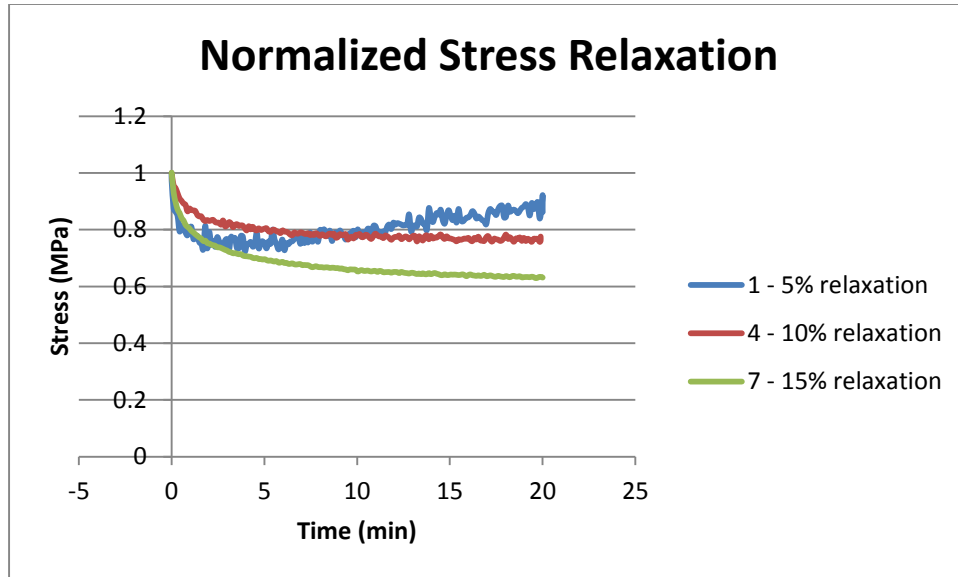


Figure 4.17: Normalized Stress-Relaxation

By applying the value of elasticity from the tensile testing to the relaxation, the Maxwell model in Equation 5 for viscoelastic relaxation at constant strain can be rearranged to solve for viscosity shown in Equation 39. This equation can then be used to approximate the viscosity parameter of skin at the 5%, 10%, and 15% strain at the time of the stress minimum respectively in samples 1, 4, and 7 as shown in Table 4-13. In doing so, the apparent stiffening of the material is not taken into account, thus the calculations of the relaxation time with Equation 8 are considered unrealistic.

$$\frac{-Et}{\ln\left(\frac{\sigma_{Maxwell}}{\sigma_o}\right)} = \eta \quad \text{Eq. 4.4}$$

Table 4.11: Maxwell Viscosity

Strain	Stress Min. (MPa)	Time (min)	Viscosity(GPa · s)	Relaxation time
--------	-------------------	------------	--------------------	-----------------

5% - Relaxation Sample No.1	0.12	3.95	0.56	12.17
10% - Relaxation Sample No.4	0.27	19.84	3.45	74.59
15% - Relaxation Sample No.7	0.82	19.63	1.97	42.64

#### 4.4 Cutting

To ascertain the fracture toughness of skin during practical applications, the cutting force with the number 11 scalpel blade was measured using the scalpel attachment to the MTS load frame and the skin mount. It was observed during testing the scalpel blade had to overcome a greater initial load due to folding of the skin before a steady rate of cutting or crack propagation was reached at a lower load level of approximately 10 N (2.25lbs). Because of this the calculation of the fracture toughness of skin with McCarthy's energy equation is best represented only in this region of steady propagation which occurs approximately between 0.026 and 0.05m.

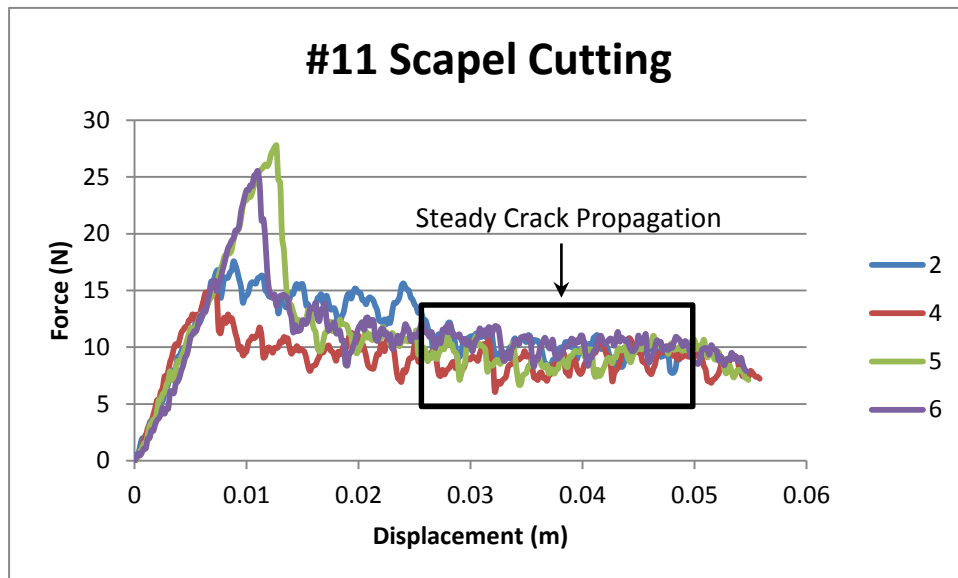


Figure 4.18: Load-Displacement During Skin Cutting with #11 Scalpel

A similar approach as Doran and McCarthy was used to calculate the energy required to create the incision by integration of force and displacement. However, because the blades are sufficiently sharp that the remote deformation is minimal, and the thin layer of skin was allowed to fall away in the upright position, the energy lost due to remote deformation and frictional force is considered negligible. Additionally, because the fracture toughness is only being calculated from the steady state region, it is both impractical and unnecessary to calculate energy lost to the initial deformation of the material as Doran had previously done. Hence, in this experiment the fracture toughness or critical energy release rate is strictly calculated from the steady state region of the load-displacement plot via Equation 40.

$$J = \frac{X \cdot u}{dA} \quad \text{Eq. 4.5}$$

In using the previously found young's modulus from the tensile experiments it then becomes possible to use the relationship for the toughness, sometimes referenced as  $G_{1c}$  or  $\gamma$ , to calculate the mode I fracture toughness constant ( $K_{1c}$ ) as shown in Equation 42 and summarized in Table (Ashby, 2011).

$$G_{1c} = \frac{K_{1c}^2}{E(1 + \nu)} \quad \text{Eq. 4.6}$$

$$K_{1c} = \sqrt{G_{1c}E(1 + \nu)} \quad \text{Eq. 4.7}$$

Table 4.12: Summary of Fracture Toughness

Specimen	Region Length (m)	Thickness (mm)	Cutting Work (J)	Work of Fracture	Fracture Toughness
----------	-------------------	----------------	------------------	------------------	--------------------

				(J/m <sup>2</sup> )	(Pa√m)
2	0.024	3.60	0.22	1276.73	38400.85
4	0.024	3.25	0.21	1312.64	38937.09
5	0.024	3.81	0.22	1199.10	37215.00
6	0.024	4.20	0.25	1239.09	37830.55

## 5. NUMERICAL APPROACH

Numerical simulations were conducted to study the accuracy of the collected empirical model data that describes the material properties of skin and the correlation of these properties to the fracture toughness. To do this, the curve fitted Mooney-Rivlin model was first verified by creating a finite element model (FEM) based on the dog-bone specimen profile and subjected to the same strain conditions as the specimen using the implicit solver in Ansys. Next, the hyperelastic skin and linear elastic 440A stainless steel scalpel were modeled in a separate Ansys input file provided in Appendix A.1 to describe the contact between the skin and blade. In this model de-bonding interface elements were used to calculate the stress at the crack tip, the distance of the crack ahead of the blade tip, and the reaction force on the blade.

### 5.1 Dog-Bone Model

To study the effects of the specimen geometry on the localized stress and strain experienced in the gauge length a Finite Element Analysis (FEA) was performed on a dog-bone specimen in Ansys Workbench. In this analysis the dog-bone geometry was generated by modifying the SolidWorks stencil file to match the recorded dimensions of specimen number 17 as shown in Figure 5.1. Similarly the material properties used in this model were obtained from the tensile experiments described in Section 4.2. These included the regressed Mooney Rivlin 3-parameter coefficients, the elastic modulus of 77 MPa. While the sample was assumed to behave in an incompressible manner, it was necessary to approximate the Poisson's ratio to 0.49967 instead of an absolute 0.5 to allow for a better numerical convergence.

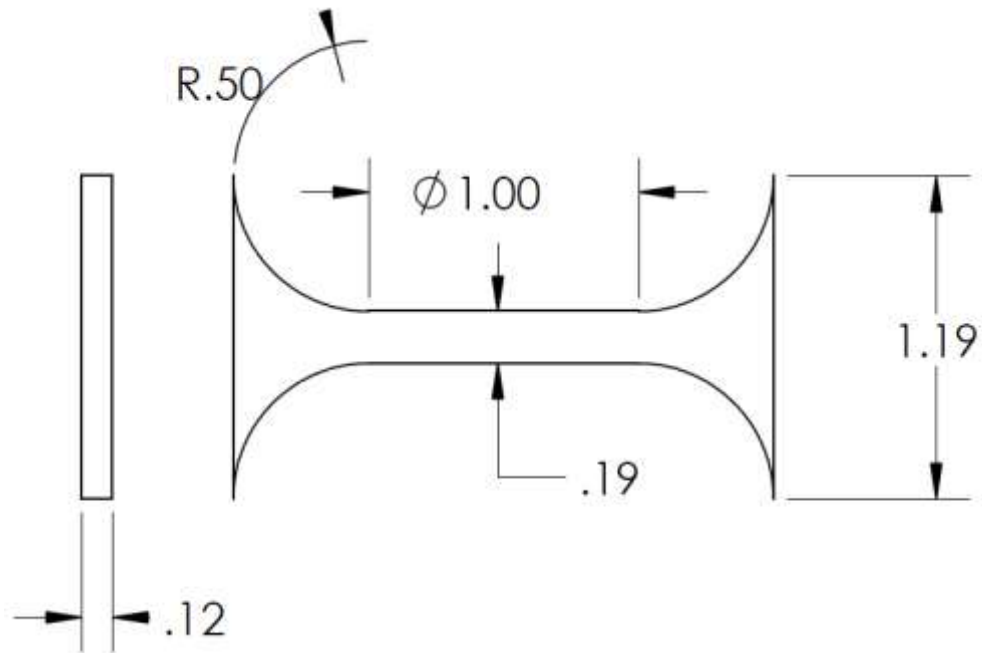


Figure 5.1: Specimen 17 Geometry (inches)

The dog-bone profile was meshed using a mapped face feature with SOLID186 20 node elements (Figure 5.2). Next, a fixed boundary condition was applied to a single face of the extruded geometry and displacement condition of was applied to the opposite face. In this model, the value of the displacement was set equal to the 19.251mm crosshead displacement recorded during the tensile testing of specimen number 17.

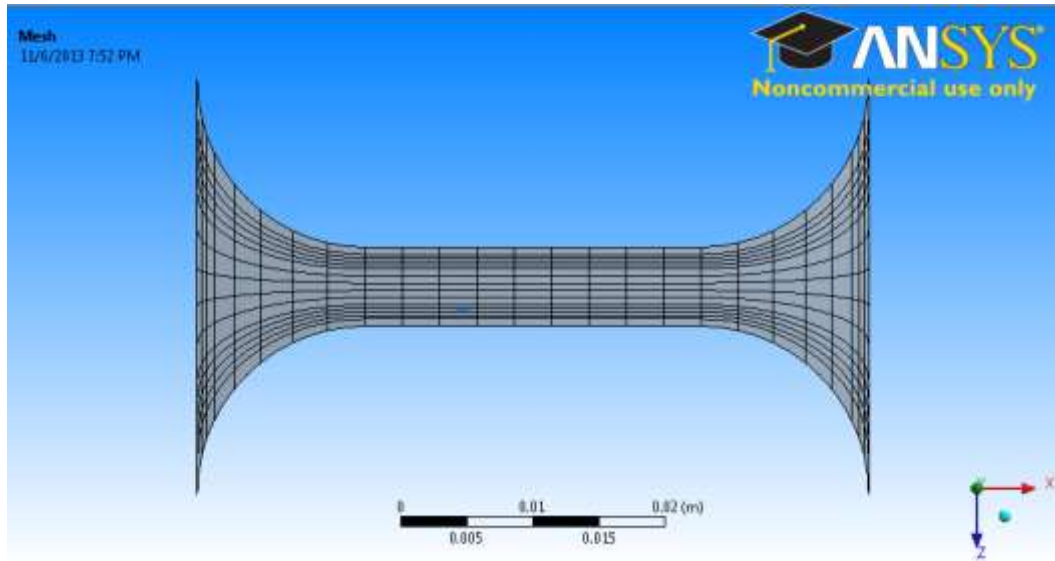


Figure 5.2: Dog-bone Mapped Mesh

## 5.2 Cutting Model

To model the crack propagation of skin during cutting with a scalpel blade with the nonlinear implicit geometry solver in Ansys, several assumptions were first made about the geometry and boundary conditions of this interface. First, it was assumed that the blade geometry could accurately be represented as a triangular wedge with a tip radius of several microns. Next, it was decided that the problem could be simplified by using a 2D symmetric model with a plane of symmetry about the center of the blade. Finally, it was assumed that the geometry of the skin during steady state cutting could be represented by placing a notch in the skin (Figure 5.1). The purpose of this notch is to reduce the amount of excessive element deformation where the blade contacts the skin, thus improving the overall stability of the model.



in Figure 5.2. In this analysis the blade was examined using a glass slide ruler and Dino-Lite Microscopy eyepiece camera. In a cross section microscope analysis with Leica FireCam software this showed that the scalpel angles out at approximately 30 degrees to a final width of 300  $\mu\text{m}$ .

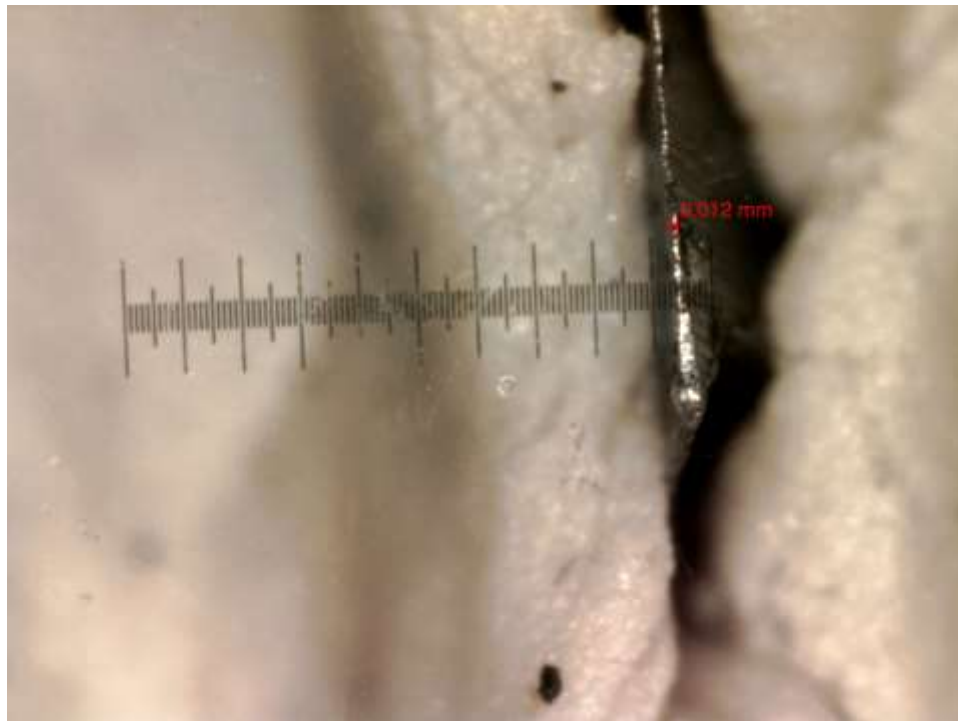


Figure 5.4: Microscopy Scalpel Thickness

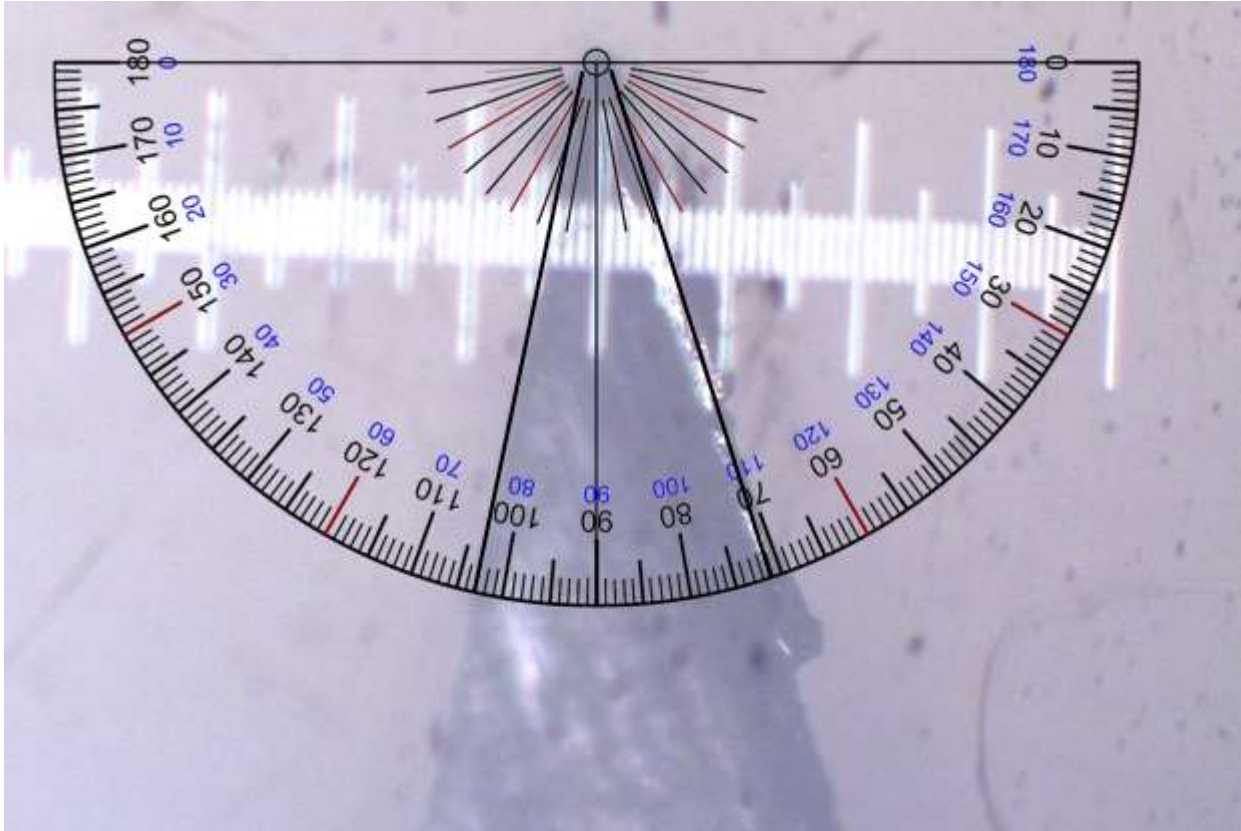


Figure 5.5: Microscopy Scalpel Cross-Section Angle

To generate the blade tip geometry in this model, it was necessary to divide the blade tip into two sections to avoid problems in adding areas that are infinitesimally close to one another. First a 12  $\mu\text{m}$  quarter circle at was generated with an overlapping rectangular area set to 15 degrees; half the of the blade angle. Once these two areas were combined, they were once again divided along the x-axis. In doing so, it was possible to generate a high quality mesh with rectangular elements by specifying the number of element divisions to be used along the straight edge of the quarter circle and along the length of the blade (Figure 5.3). The element type used in this mesh was 2-D four node PLANE182 element in which plane strain was activated with an

enhanced strain formulation to better account for the high strain of the nearly incompressible material.

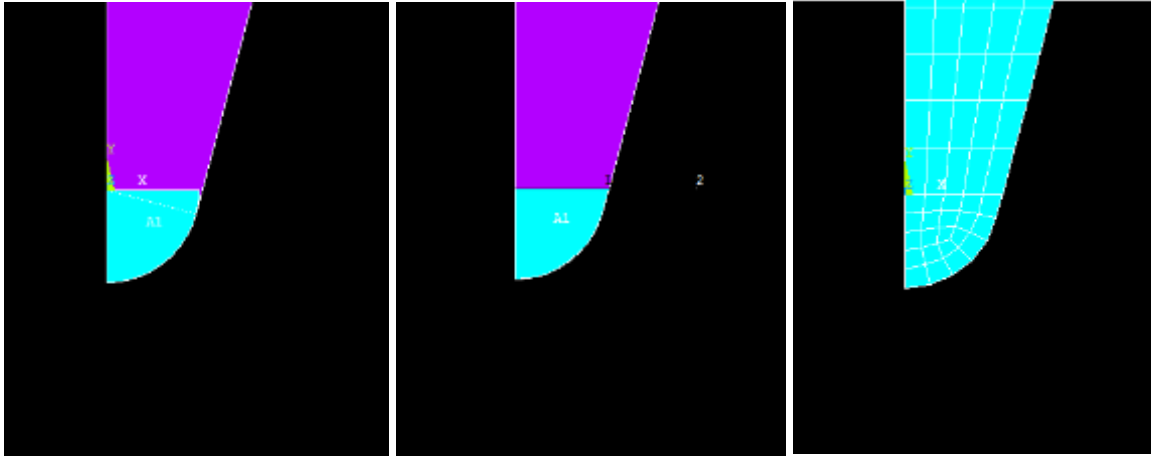


Figure 5.6: Blade Tip Mesh

Similarly, in the modeling of the skin two rectangles with a set number of element divisions were combined to create a notched geometry in skin. However, to better focus the FEA on the region of interest along the de-bonding surface, a spacing ratio of 2:1 was placed to twice as many nodes on the end near the crack initiation when compared to the far side of the model (Figure 5.4). Additionally, it was necessary to generate a thin area on the opposite side of the y-axis to provide fixed elements to prevent the finite element skin from crossing the symmetry plane and provide nodes from which the interface elements could de-bond from.

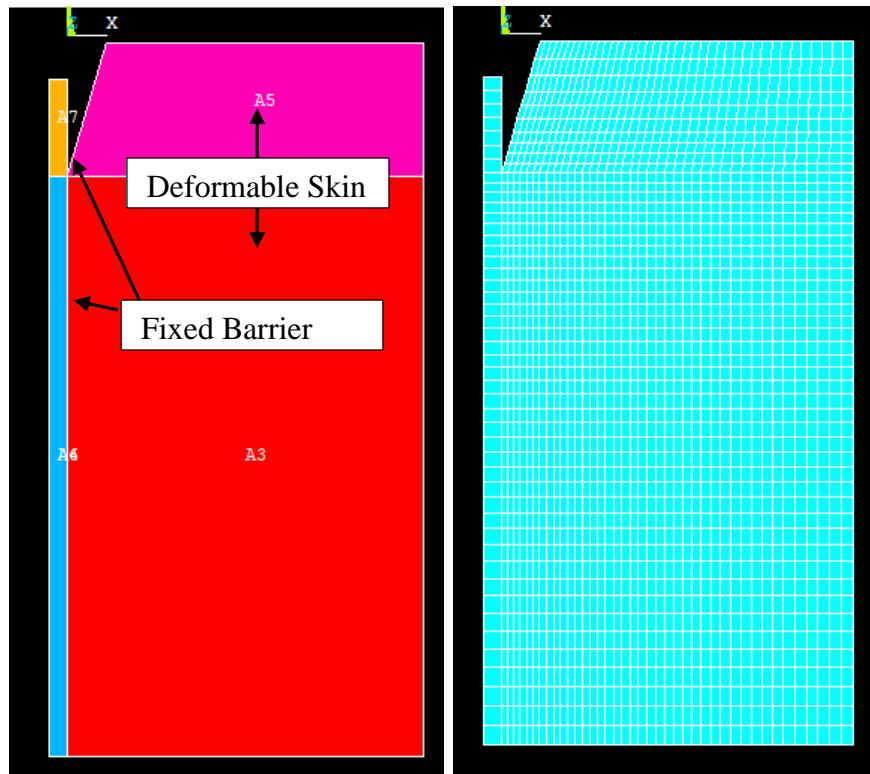


Figure 5.7: Skin Mesh

Due to the relatively small dimensions of the blade tip geometry, it was necessary to appropriately scale the dimensions of the model and stress values to further reduce the solve time of the FEA and avoid the use of extremely large or small magnitudes for velocity, length, and density. This was accomplished by assuming that the “measured” force on the blade nodes could be output as a scalar with nonconventional units and converted back to newton force units during post processing analysis. This is shown in Table 5-1 where the solver units are specifically manipulated to change the magnitude of the resulting variables of stress, density, velocity, and force shown in Table 5-2.

Table 5.1: Solver Unit Conversions

	Mass	Length	Time
--	------	--------	------

Standard Units	kilograms	meter	seconds
Solver units	$m' = 10^{-6}\text{kg}$	$L' = 10^{-5}\text{m}$	$s' = 10^{-4}\text{s}$
Conversion Factor	$1 \times 10^{-6}$	1	$10^{-4}$

Table 5.2: Variable Unit Conversions

	Force	Stress	Density	Velocity
Standard Units	$N = \frac{\text{Kg} \times \text{m}}{\text{s}^2}$	$\text{Pa} = \frac{\text{Kg}}{\text{m} \times \text{s}^2}$	$\rho = \frac{\text{Kg}}{\text{m}^3}$	$V = \frac{\text{m}}{\text{s}}$
Substitution	$\frac{10^6 \times 10^5}{(10^4)^2}$	$\frac{10^6}{10^5 \times (10^4)^2}$	$\frac{10^6}{(10^5)^3}$	$\frac{10^5}{10^4}$
Conversion Factor (standard to solver)	$10^3$	$10^{-7}$	$10^{-9}$	10

## 6. RESULTS AND DISCUSSION

### 6.1 Tensile Analysis

During the analysis of the dog-bone specimen tensile simulation generated in Ansys Workbench, it was realized that the model was not correctly implementing the hyperelastic material model in the generated input file. Instead, the material was being modeled as linear elastic isotropic material shown in Figure 6.1 and 6.2. In these analyses it shows that the maximum stress experienced by the gauge length at the recorded specimen displacement was approximately 38MPa with a 0.49 strain value, much higher than the empirically recorded value of 11.6 MPa and 0.26 strain.

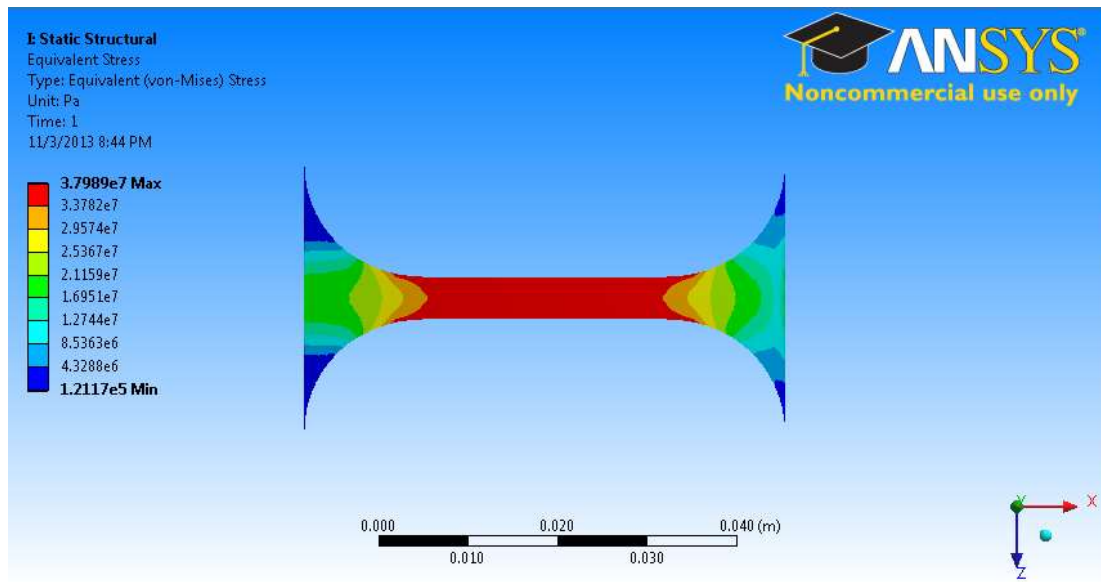


Figure 6.1: Linear Elastic Dog-bone Equivalent stress at crosshead displacement with video extensometer data in Workbench

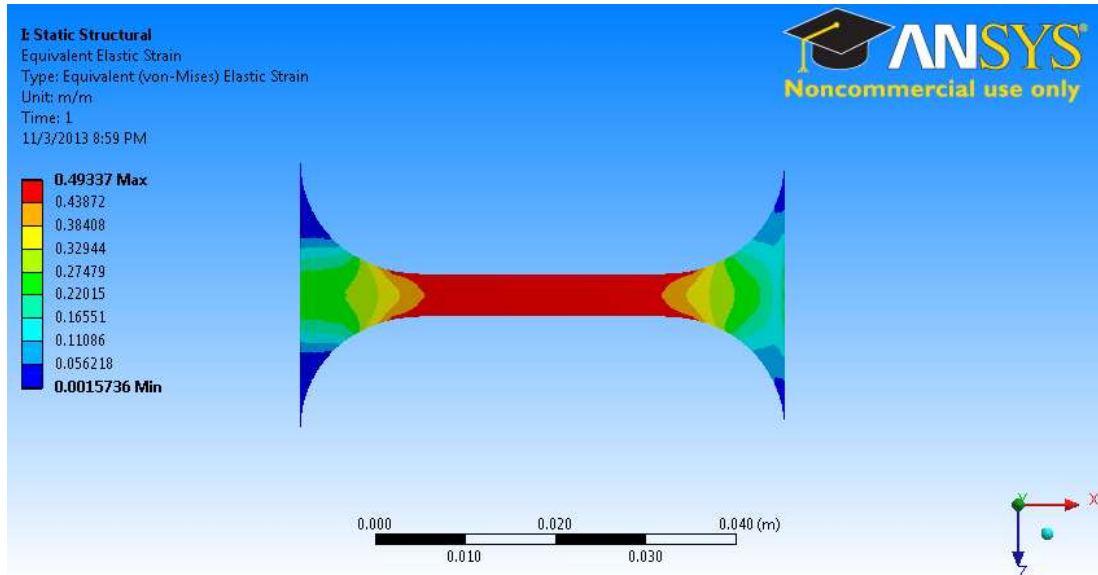


Figure 6.2: Linear Elastic Dog-bone Equivalent strain at crosshead displacement with video extensometer data in Workbench

To properly implement the Mooney Rivlin model into Ansys, the generated mesh was exported as an input file into Ansys traditional. From there the 3-parameter Mooney Rivlin model was added to the material properties and the nonlinear solver was turned on. The resulting FEA produced a slightly lower maximum Von Mises stress of about 33MPa and 43% strain value shown respectively in Figure 5.4 & 5.5, however, these values are still significantly higher than the recorded empirical strain.

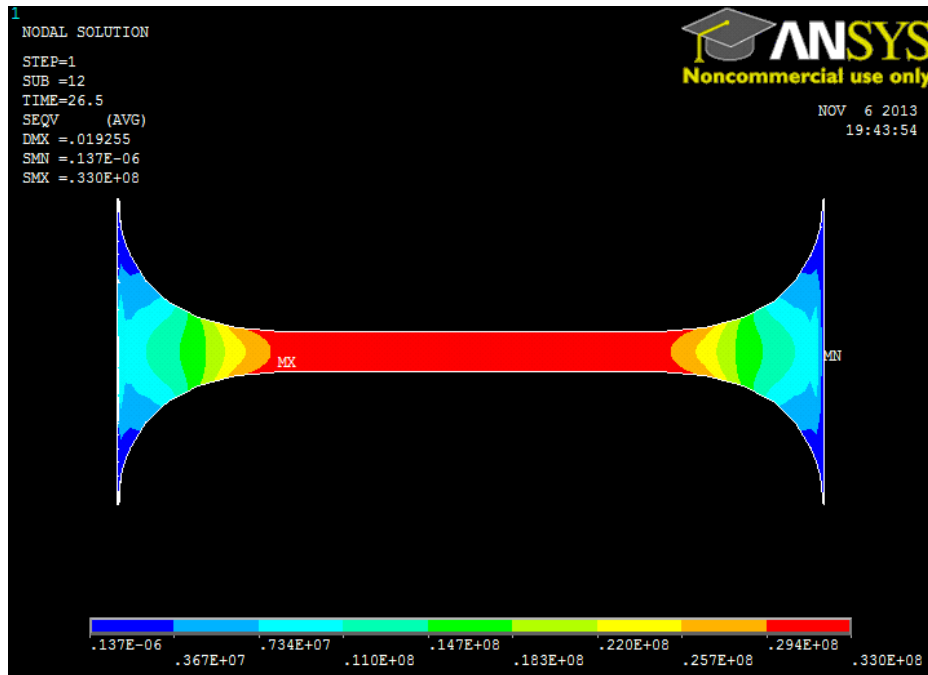


Figure 6.3: Dog-bone Equivalent stress at cross head displacement and with video extensometer data in APDL

(units: Pa)

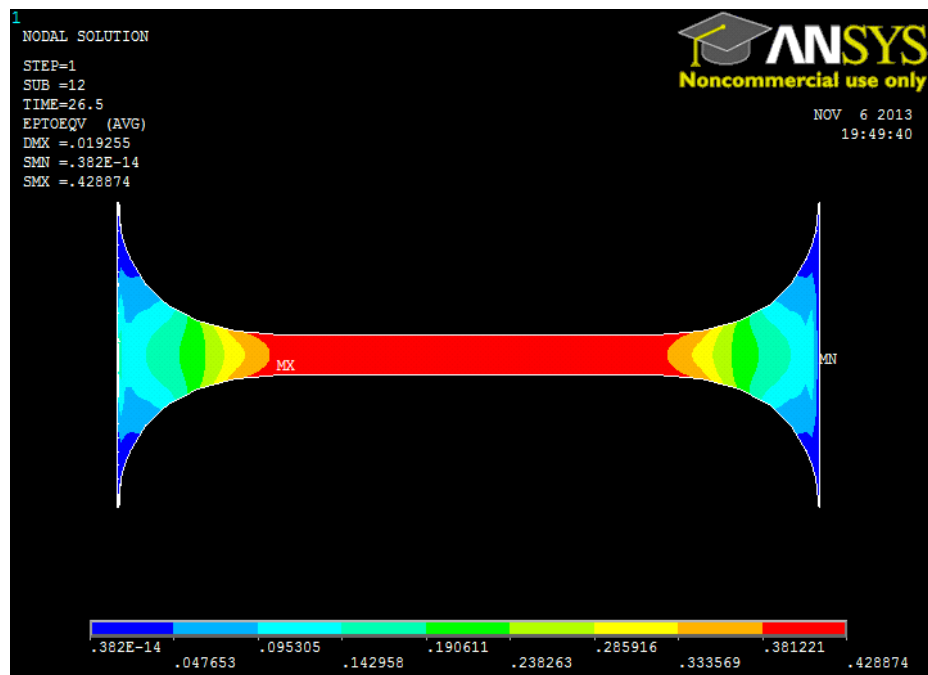


Figure 6.4: Dog-bone Equivalent strain at crosshead displacement with video extensometer data in APDL

To correct for this overshoot, a third simulation was prepared using the calculated displacement 6.07 mm shown by the gauge length from video extensometer. In this case, the maximum stress experienced by the model was 11.5 MPa and 0.149 strain; much closer to the actual stress recorded in the empirical analysis and in literature reviews. Based on this, it can be inferred that the crosshead displacement is not representative of the true displacement of the gauge length. This supports earlier assumptions that the strain recorded by the crosshead is overestimated due to deflection at the boundary conditions and poor fixation in the clamps.

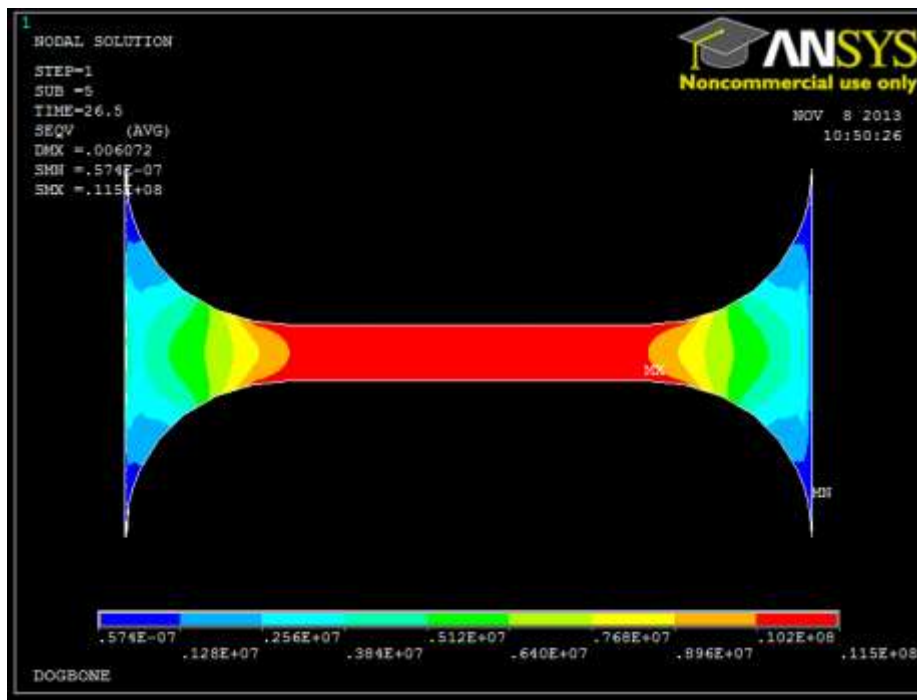


Figure 6.5: Dog-bone Equivalent stress at recorded gauge length displacement and with video extensometer data in APDL (units: Pa)

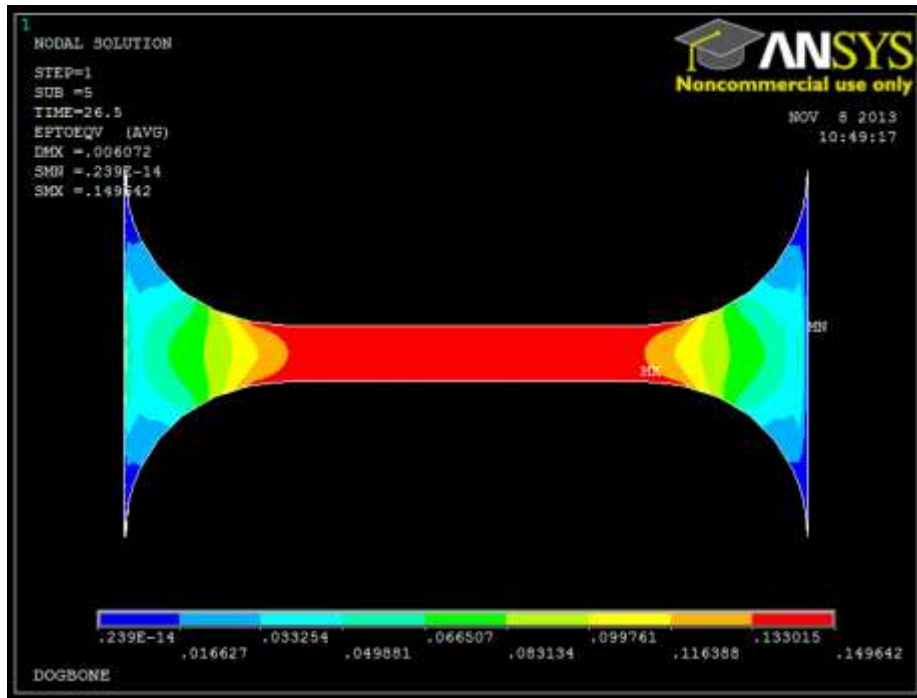


Figure 6.6: Dog-bone Equivalent strain at gauge length displacement with video extensometer data in APDL

## 6.2 Cutting Analysis

In the cutting simulation performed in Ansys a separate post processing and export code provide in Appendix A.2 and A.3 were written to keep track of the stress at the crack, the position of the blade tip, the position of crack, the maximum stress along the crack path, and the simulated reaction force on the blade. Due to the scaling convention applied to the solver units it was first necessary use the factors listed in Table 6. to convert all the length, stress and force values from the FEA back into conventional units of meters, Pascal's, and newtons.

Table 6.1: Conversion Factor of solver units to SI units

Standard Unit	Length (m)	Stress (Pa)	Force (N)

Conversion Factor	$10^{-5}$	$10^7$	$10^{-3}$
-------------------	-----------	--------	-----------

In a contour plot of the Von Mises stresses during the first substep of the iterative solver see in Figure 7, it shows the initial elements in contact with the blade results in a localized distortion of individual elements resulting in an unrealistically large stress value. Nevertheless, the simulation also shows that there is a stress region localized around the crack that is expected in notched geometries.

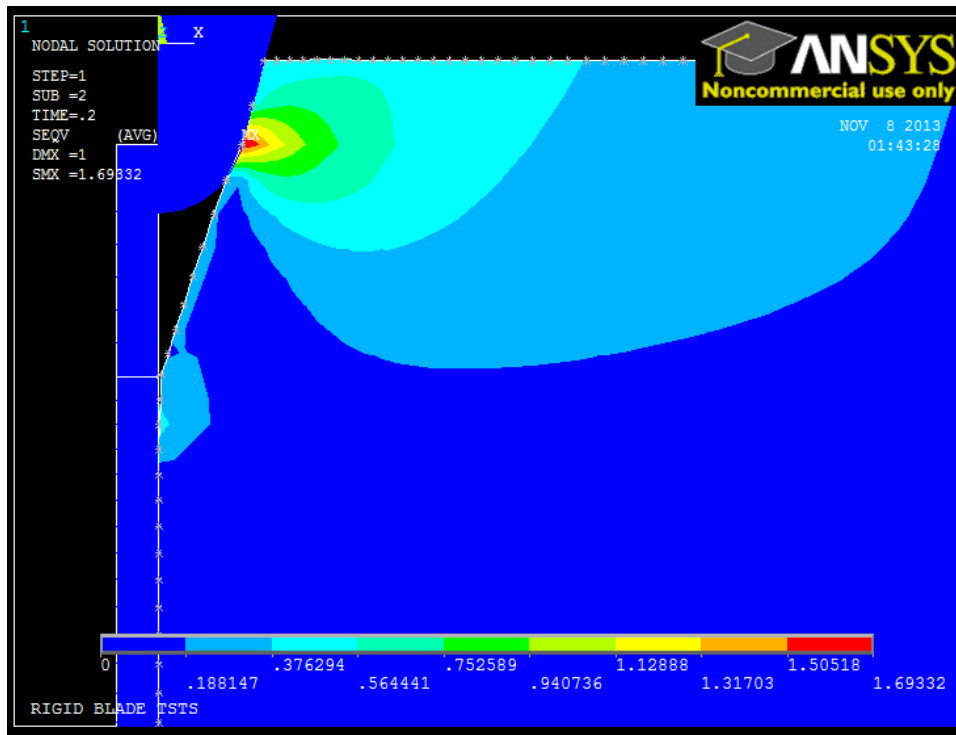


Figure 6.7: Equivalent stress during initial contact between blade and skin (units:  $10^{-7}$ )

When the post processing code is run, the stress at this crack tip can be plotted as a function of time as shown in Figure 6.8. Although the de-bond stress of the interface element was set to 11.6 MPa, this plot shows that the stress of the crack tip did not remain constant at this

value. Instead the values tend to fluctuate as the load jumps from node to node along the path of the crack.

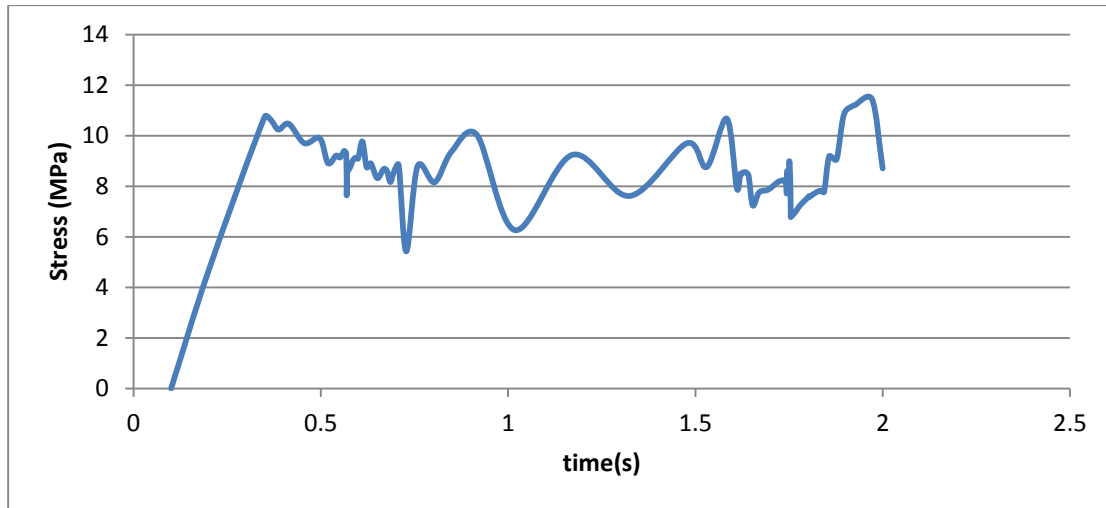


Figure 6.8: Crack Tip Stress

Based on the position of the blade and the node released from the interface it the distance ahead of the blade in which the crack propagates can also be calculated. This gap is largely due to the notched geometry that forms between the skin crack from and the width of the blade radius as seen in Figure 6.9 showing the final deformation of the skin during the finite element analysis.

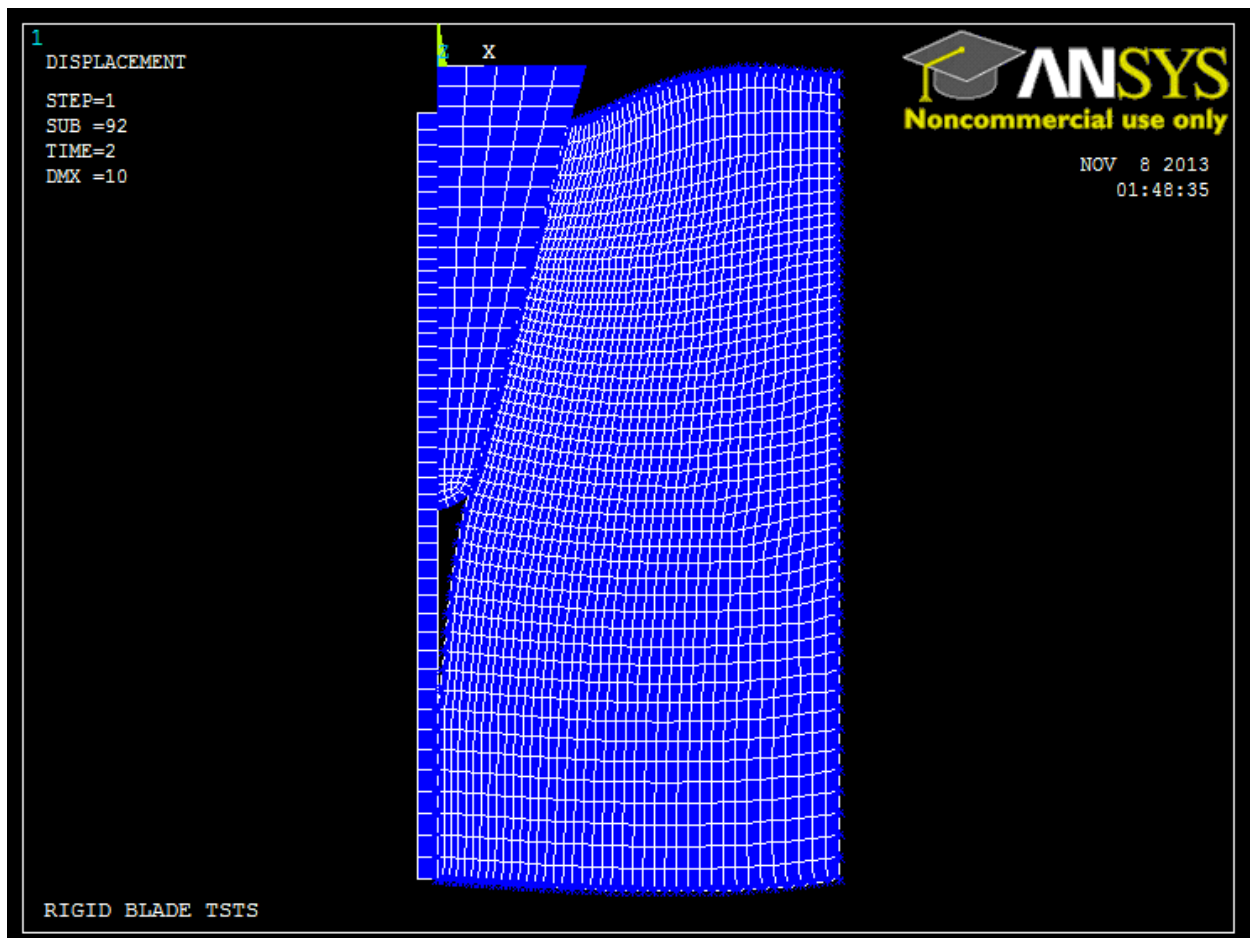


Figure 6.9: Final deformation of the FEA

The force required to cut the material can be exported by taking the summation of the reaction force on the blade nodes. When plotted this is plotted against blade displacement, as shown in Figure 6.10, it can be seen that the force is expected to increase exponentially as the blade continues into the material.

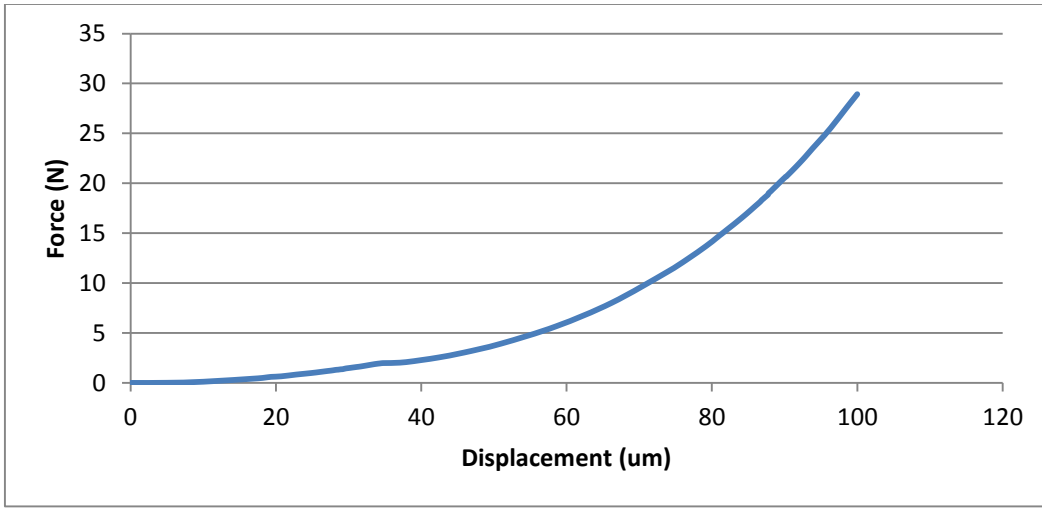


Figure 6.10: FEA Blade Reaction Force During Cutting

While this exponential behavior of force is observed in the region of cut initiation during the experimental testing, there is no indication from this finite element analysis that the cutting force will level off as observed during the cutting with the number 11 scalpel.

## 7. CONCLUSIONS

To characterize the mechanical properties and behavior of skin during surgical cutting a cyclic preconditioning protocol was developed and three types of experiments were implemented and discussed in this thesis. The first type of experiment consisted of uniaxial testing on a dog-bone profile specimen with a video extensometer to provide the stress-strain response of the material on which a nonlinear regression analysis could be performed. Next, stress relaxation experiments were performed using the same dog-bone profile at three different strain levels. Finally, the fracture toughness of the skin was empirically measured during the cutting of the material with a surgical blade. The relationship between this experimental data and a Mooney Rivlin hyperelastic model constitutive model was then examined using finite element analysis of the dog-bone tensile experiment and the cutting experiment. The results suggest that the even with specialized grips specimen slipping may be present and video strain measurement is essential to generate an accurate material model of biomaterials.

## REFERENCES

- Acner. (2011). *What is collagen & elastin*. Retrieved December 1, 2011, from Acner.org: Acne Treatment: <http://acner.org/what-is-collagen-elasting>
- Agache, P., Humbert, P., & Maibach, H. (2004). *Measuring the skin*. New York, NY: Springer Verlag.
- Amar, D., Fogel, D., & Shah, J. (1996, July). The Shaw Hemostatic Scalpel as an Alternative to Electrocautery in Patients with Pacemakers. *Anesthesiology*, 85(1), 223. Retrieved from [http://journals.lww.com/anesthesiology/fulltext/1996/07000/the\\_shaw\\_hemostatic\\_scalpel\\_as\\_an\\_alternative\\_to.36.aspx](http://journals.lww.com/anesthesiology/fulltext/1996/07000/the_shaw_hemostatic_scalpel_as_an_alternative_to.36.aspx)
- Ankersen, J. (1999). Puncture resistance and tensile strength of skin simulants. *Proceedings of the Institution of Mechanical Engineers Part H Journal of Engineering in Medicine*, 213, pp. 493-501. Scotland: University of Glasgow.
- Ashby, M. F. (2011). *Materials Selection in Mechanical Design Fourth Edition*. Oxford: Elsevier.
- Balmer, D. (2003, December 3). *Mathematical Models of Viscoelastic Behaviour*. Retrieved September 29, 2013, from Chemical Engineering at University of Edinburgh: <http://www.see.ed.ac.uk/~johnc/teaching/fluidmechanics4/2003-04/visco/>
- Battles, C. (2010, April 22). *Calculating Mooney-Rivlin Constants*. Retrieved March 13, 2013, from SchrodingersGhost.com: <http://www.schrodingersghost.com/?p=334>
- Belkoff, S. M., & Haut, R. C. (2008). Experimental Methods in Biological Tissue Testing. In *Springer Handbook of Experimental Mechanics Sharpe (Ed.)*. New York: Springer.
- Borges, A. F. (1984). Relaxed Skin Tension (RSTL) Lines Versus Other Skin Lines. *Plastic and Reconstructive Surgery*, 144-150.
- Brannon, H. (2007, April 9). *Skin Anatomy*. Retrieved July 23, 2013, from About.com: <http://dermatology.about.com/cs/skinanatomy/a/anatomy.htm>
- Branson. (2012, January). *Ultrasonic Welding*. Retrieved December 5, 2012, from Emerson Industrial Automation: [http://www.emersonindustrial.com/en-US/documentcenter/BransonUltrasonics/Plastic%20Joining/Ultrasonics/Technologies/TL-2\\_Amplitude\\_Reference\\_Guide.pdf](http://www.emersonindustrial.com/en-US/documentcenter/BransonUltrasonics/Plastic%20Joining/Ultrasonics/Technologies/TL-2_Amplitude_Reference_Guide.pdf)

- Carew, E. O., Garg, A., Barbaer, J. E., & Vesely, I. (2004, April). Stress Relaxation Preconditioning of Porcine Aortic Valves. *Annals of Biomedical Engineering*, XXXII(4), 563-572.
- Chan, K. K., Wtmough, D. J., Hope, D. T., Moir, K., & Chan, F. (1985). The Mode of Action of Surgical Tissue Removing Devices. *IEEE 1985 Ultrasonics Symposium*, (pp. 855-859).
- Chanthasopephan, T., Desai, J. P., & Lau, A. C. (2006). Determining fracture characteristics in scalpel cutting of soft tissue. *Paper presented at the Biomedical Robotics and Biomechatronics*, (pp. 899-904). Philadelphia.
- Cimino, W., & Bond, L. (1995). Physics of ultrasonic surgery using tissue fragmentation. *Ultrasonics Symposium, 1995. Proceedings., 1995 IEEE*, 2(11), pp. 1597-1600.
- Courtney, T. H. (2005). *Mechanical Behavior of Materials*. Long Grove, IL: Waveland Press.
- Department of Medical Physics, University of Amsterdam. (2005). *Principles of Medical Physics Compendium: Principles of Medical Physics and Medical Technology*. (N. Schellart, Editor) Retrieved December 30, 2012, from Electrosurgery: <http://onderwijs1.amc.nl/medfysica/compendiumDT.htm>
- Diridollou, S., Berson, M., Vabre, V., Black, D., Karlsson, B., Auriol, F., . . . Patat, F. (1998). An in vivo method for measuring the mechanical properties of the skin using ultrasound. *Ultrasound in Medicine & Biology*, 24(2), 215-224.
- Dong Sun, Zhou, Z. Y., Liu, Y. H., & Shen, W. Z. (1997). Development and application of ultrasonic surgical instruments. *Biomedical Engineering, IEEE*, 462-467.
- Doran, C. F., McCormack, B. A., & Macey, A. (2004). A simplified model to determine the contribution of strain energy in the failure process of thin biological membranes during cutting. *Strain*, 40(4), 173-179.
- Dunn, M., & Silver, F. (1983). Viscoelastic behavior of human connective tissues: Relative contribution of viscous and elastic components. *Connective Tissue Research*, 12(1), 59-70.
- Edwards, C., & Marks, R. (1995). Evaluation of biomechanical properties of human skin. *Clinics in Dermatology*, 13(4), pp. 375-380.
- Foutz, T., Stone, E., & Abrams, C. J. (1992). Effects of Freezing on Mechanical Properties of Rat Skin. *American Journal of Veterinary Research*, 53(5), 788-792.

- Fuchs, J. (2012, January 4). *Ultrasonics – Transducers – Piezoelectric Hardware*. Retrieved December 24, 2012, from John Corner's Technical Blog: Cleaning Technology Group: <http://www.ctgclean.com/tech-blog/2012/01/ultrasonics-transducers-piezoelectric-hardware/>
- Green, A. R., Elgart, G. W., Ma, F., & Federman, D. G. (2004). Documenting dermatology practice: Ratio of cutaneous tumors biopsied that are malignant. *Dermatologic Surgery*, *30*(9), 1208-1209.
- Hendriks, F. M., Brokken, D., van Eemeren, J. T., Oomens, C. W., & Baaigens, J. A. (n.d.). A numerical-experimental method to characterize the non-linear mechanical behaviour of human skin. *Skin Research & Technology*, *9*, pp. 274-283.
- Hibbeler, R. C. (2011). *Mechanics of Materials Eighth Edition*. Upper Saddle River: Prentice Hall.
- Holt, K. (2010, April/May). Exploring the Ultrasonic Welding Stack. *Plastics Decorating*, pp. 18-21. Retrieved January 5, 2013, from [www.herrmannultrasonics.com/uploads/media/Plastics\\_Decorating\\_Assembly\\_April\\_May\\_\\_01.pdf](http://www.herrmannultrasonics.com/uploads/media/Plastics_Decorating_Assembly_April_May__01.pdf)
- Homayounfar, K., Meis, J., Jung, K., Klosterhalfen, B., Sprenger, T., Conradi, L.-C., . . . Becker, H. (2012). Ultrasonic scalpel causes greater depth of soft tissue necrosis compared to monopolar electrocautery at standard power level settings in a pig model. *BMC Surgery*, *12*(3).
- Humphrey, J. D. (2008). Biological Soft Tissues. In *Springer Handbook of Experimental Mechanics Sharpe (Ed.)* (pp. 169-185). New York: Springer.
- Jachomicz, J., McMullen, R., & Prettypaul, D. (2007). Indentometric analysis of in vivo skin and comparison with artificial skin models. *Skin Research & Technology*, *13*, 299-309.
- Khatyr, F., Imberdis, C., Vescovo, P., & Varchon, D. (2004). Model of the viscoelastic behavior of skin in vivo and study of anisotropy. *Skin Research & Technology*, *10*(2), 96-103.
- Krehbiel, J., & Berfield, T. (2005). Applying digital image correlation to biological materials. *Unpublished manuscript, Sotos Research Group at the Beckman Institute for Advanced Science and Technology Illinois, University of Illinois*. Urbana, Illinois.

- Lapeer, R. J., Gasson, P. D., & Karri, V. (2011). A hyperelastic finite-element model of human skin for interactive real-time surgical simulation. *Biomedical Engineering, IEEE Transactions on*, 58(4), 1013-1022.
- Lim, J., Hong, J., Chen, W. W., & Weerasooriya, T. (2011). Mechanical response of pig skin under dynamic tensile loading. *International Journal of Impact Engineering*, 38(2-3), 130-135.
- Liu, Z., & Yeung, K. (2008). The Preconditioning and Stress Relaxation of Skin Tissue. *Journal of Biomedical & Pharmaceutical Engineering*, 2(1), 22-28.
- Livermore Software Technology Corporation. (2012, April 18). *LS-DYNA manuals*. Retrieved November 20, 2012, from LS-DYNA Support: [http://www.dynasupport.com/manuals/ls-dyna-manuals/LS-DYNA\\_manual\\_Vol\\_II\\_R6.0.0.pdf](http://www.dynasupport.com/manuals/ls-dyna-manuals/LS-DYNA_manual_Vol_II_R6.0.0.pdf)
- Lokseva Surgicals. (n.d.). *Surgical Blades*. Retrieved January 4, 2013, from Lokseva Surgicals: <http://www.loksevasurgicals.com/surgical-blades.htm>
- MacFarlane, D., & Raphini, R. (2010). *Skin cancer management: Biopsy techniques and interpretation* (1 ed., Vol. 1). New York, NY: Springer.
- Mansour, J. M., Davis, B. R., Srour, M. M., & Theberge, R. R. (1993). A method for obtaining repeatable measurements of the tensile properties of skin at low strain. *Journal Of biomechanics*, 26(2), 211-216.
- Mason, T. J., & Lorimer, J. P. (2002). *Applied Sonochemistry*. Weinheim, Germany: Wiley.
- McCarthy, C. T., Annaidh, A. N., & Gilchrist, M. D. (2010). On the Sharpness of Straight Edge Blades in Cutting Soft Solids Part II – Analysis of Blade Geometry. *Engineering Fracture Mechanics*, 77(3), 473-451.
- McCarthy, C. T., Hussey, M., & Gilchrist, M. D. (2007). On the sharpness of straight edge blades in cutting soft solids: Part I – indentation experiments. *Engineering Fracture Mechanics*, 74(14), 2205-2224.
- McCulloch, E. (2012, December 10). *Experimental and finite element modelling of ultrasonic cutting of food*. Retrieved July 1, 2013, from University of Glasgow: <http://theses.gla.ac.uk/264/>
- Messana, C. A., & Wagner, A. M. (2008). emystifying dog-ears. *Pediatric Dermatology*, 25(3), 416-418.

- Moon, D. K., Woo, S. L.-Y., Takakura, Y., Gabriel, M. T., & Abramowitch, S. D. (2006). The effects of refreezing on the viscoelastic and tensile properties of ligaments. *Journal Of Biomechanics*, 39(6), 1153-1157.
- Natali, A. N., Carniel, E. L., & Pavan, P. G. (2006). Hyperelastic Models for the Analysis of Soft Tissue Mechanics: Definition of Constitutive Parameters. *IEEE/RAS-EMBS Int. Conf. Biomedical*, (pp. 1-8). Pisa.
- Piezo Systems*. (n.d.). Retrieved Decemeber 24, 2012, from History of Piezoelectricity: <http://www.piezo.com/tech4history.html>
- Polyakov, V. A., Nikolaev, G. A., Volkov, M. V., Loshchilov, V. I., & Loshchilov, V. I. (1974). *Ultrasonic Bonding of Bones and Cutting of Live Tissues*. (L. Aksenova, & B. Kuznetsov, Trans.) Moscow, Union of Soviet Socialist Republics: Mir Publishers.
- Rao, S. S. (2011). *Mechanical Vibrations (5th ed.)*. Upper Saddle River, NJ: Pearson.
- Roylance, D. (2001, October 21). *Engineering Viscoelasticity*. Retrieved September 29, 2013, from Massachusetts Institute of Technology Department of Material Science and Engineering: <http://web.mit.edu/course/3/3.11/www/modules/visco.pdf>
- Samsam, M. (2012). *Functionally Oreinted Regional Anatomy*. Hayden-McNeil.
- Schultz, G. S., Ladwig, G., & Wysocki, A. (2005, August 30). *Extracellular Matrix: Review of its Role in Acute and Chronic Wounds*. Retrieved July 18, 2013, from World Wide Wounds: <http://www.worldwidewounds.com/2005/august/Schultz/Extrace-Matric-Acute-Chronic-Wounds.html>
- Shergold, O. A., Fleck, N. A., & Radford, D. (2006). The uniaxial stress versus strain response of pig skin and silicone rubber at low and high strain rates. *International Journal of Impact Engineering*, 32(9), 1384-1402.
- Shih, C. F., Moran, B., & Nakamura, T. (1986). nergy Release Rate Along a Three-Dimensional Crack Front in a Thermally Stressed Body. *International Journal of Fracture*, 30(2), pp. 79-102.
- Silver, F. H., Freeman, J. W., & Devore, D. (2001). Viscoelastic Properties of Human Skin and Processed Derma. *Skin Research and Technology*(7), 18-23.

- Sinha, U. K., & Gallagher, L. A. (2003, February). Effects of Steel Scalpel, Ultrasonic Scalpel, CO2 Laser, and Monopolar and Bipolar Electrosurgery on Wound Healing in Guinea Pig Oral Mucosa. *The Laryngoscope*, 113(2), 228-236.
- Suh, E.-J., Woo, Y.-A., & Kim, H.-J. (2005). Determination of Water Content in Skin by using a FT Near Infrared Spectrometer. *Archives of Pharmacal Research*, 28(4), 458-462.
- Sun, D., Zhou, Z. Y., Liu, Y. H., & Shen, W. Z. (1997). Development and application of ultrasonic surgical instruments. *Biomedical Engineering, IEEE Transactions on*, 44(6), 462-467.
- Tilleman, T., Tilleman, M., & Neumann, M. (2004). The elastic properties of cancerous skin: Poisson's ratio and young's modulus. *Israel Medical Association Journal*, 6(12), 753-755.
- Vaitekunas, J., Stulen, F., & Grood, E. (2001). Effects of frequency on the cutting ability of an ultrasonic surgical instrument. *31st Annual Ultrasonic Industry Association Symposium The medical session-surgical/therapeutic*. Cincinnati.
- Vaitekunas, J., Stulen, F., & Grood, E. (2008). Cutting wax with an ultrasonically activated blade. *Engineering in Medicine and Biology Magazine, IEEE*, 27(4), 71-79.
- Weiner, D., Wainwright, M., Tacovorian, E., Gaudette, G., & Dunn, R. (2009). Design of a novel elliptical skin biopsy punch device. *Bioengineering Conference, 2009 IEEE 35th Annual Northeast*, (pp. 1-2). Boston.
- Welch, H. G., Woloshin, S., & Schwartz, L. M. (2005). Skin biopsy rates and incidence of melanoma: Population based ecological study. *BMJ: British Medical Journal*, 331(7515), 481-484.
- Wills, D. J., & Picton, D. (1972). An investigation of viscoelastic properties of periodontium in monkeys. *Journal of Periodontal Research*, 7(1), 42-51.
- Yamada, H. (1970). *Strength of Biological Materials*. Baltimore: Williams & Wilkins.
- Yoo, L., Kim, H., Gupta, V., & Demer, J. L. (2009, August). *Investigative Ophthalmology & Visual Science*, 50(8), 3721-3728.
- Zahn, S., Schneider, Y., & Rohm, H. (2006). Ultrasonic cutting of foods: Effects of excitation magnitude and cutting. *Innovative Food Science and Emerging Technologies*, 288-293.

- Zak, M., Kuropka, P., Kobielarz, M., Dudek, A., Katarzyna, K.-K., & Szotek, S. (2011). Determination of the mechanical properties of pig fetuses with respect to its structure. *Acta of Bioengineering and Biomechanics*, 13(2), 37-43.
- Zemanek, M., Bursa, J., & Detak, M. (2009). Biaxial Tension Tests with Soft Tissue of Arterial wall. *Engineering Mechanics*, 16(1), 3-11.
- Zhou, D., & McMurray, G. (2010). Modeling of blade sharpness and compression cut of biomaterials. *Robotica*, 28(Special Issue 02).

## APPENDIX A: CODES

## A.1 Ansys Input File (Scaled\_Implicit\_Interface\_Mooney)

```
finish
/CLEAR
/COM,ANSYS RELEASE 13.0  UP20101012   21:16:37  10/16/2012
/input,start130,ans,'C:\Program Files\ANSYS Inc\v130\ANSYS\apdl\,,,,,,,,,,,,,1
! /CWD,'C:\Users\Kevin\Desktop\SkinCrackPropagation\LSDYNA\junk' !Set working directory
/TITLE, RIGID BLADE TSTS
/COM REF: VM248, VM201
/FILENAME, CourseBladeSkin
!/units,SI !m, kg, s, K
/PREP7
smrt,off

/PNUM,LINE,1
/PNUM,AREA,1

!-----
!          ***** DESCRIPTION *****
!  A barrier exist between the blade gap, contact is not yet activated
!  contact is between blade part 1 and rightskin part 2
!  tiebreak is between the left and right edges
!-----
!          ***** Unit Conversions *****
!  1 kg          = 10E6 mg
!  1 micron      = 10E-6 m
!  1 N           = 1 kg/(m*s^2)      = 10E12 mg * micron / s^2
!  1 micron^2   = 10E-12 m
!
!  1 Pa [N/m^2]= 1 [mg * micron / s^2] / [m^2]
!  1 kg/m^3     = 10E-12 mg / micron^3
!  1 psi        = 6894.75729 Pa
!-----
!          ***** CONSTANTS *****
pi = 3.14159265358979323846264338327950
theta = 15                                ! Note 45 degrees is a vertical blade
phi = 90 - theta
R      = 1                                ! RADIUS OF BLADE (micron) * conversion
SEL_TOL=0.05*R/3
!      K,9999,SELTOL
```

```

STRESS_CONVER=1
VEL_CONVER=1
TIME_CONVER=(5*R)/(0.05*VEL_CONVER)
DENSITY_CONVER=1

OFFSET=0.2*R

BLD_LENGTH = R*10                ! -(BOTTOMBOUND-CRACK_Y)
BLD_THICK = BLD_LENGTH*tan(theta*pi/180)+R    !NO SPACES      !
cos(30)/sin(30) = 1.732
alpha = (180/pi)*atan( BLD_LENGTH/(BLD_THICK-R) )    !angle check where alpha is
the larger bisecting angle with blade

BLDDIV_Y = 20                    !BLD_LENGTH*(SKINDIV_Y/(-
BOTTOMBOUND-CRACK_Y))
BLDDIV_X = 5                    !R*(SKINDIV_X/RIGHTBOUND)

NOTCH_X = 1.1*R !-CRACK_Y/tan(phi*pi/180)          !1.5*R
NOTCH_Y = 0

NOTCHDIV_Y = 10 !( SKINDIV_Y*NOTCH_Y - SKINDIV_Y *CRACK_Y ) / (-
BOTTOMBOUND + CRACK_Y ) !divions for notch height kept same as rect of skin

CRACK_Y = -R*tan(phi*pi/180)!-2*R !
BOTTOMBOUND = -(20*R)
NOTCHED_DIV_TRUNCATE = CRACK_Y*(BLDDIV_Y/BOTTOMBOUND)

EXTRUDE = 10*R ! (R/5)
EXT_DIV = 5 ! 2

LSKIN3DIV_Y = 7
RIGHTBOUND = (10*R)
SKINDIV_X = 40 !4*RIGHTBOUND/R
SKINDIV_Y = 40 !-4*BOTTOMBOUND/R
LEFTBOUND = -RIGHTBOUND/(0.5*SKINDIV_Y)    !-(5*R)/20    ! NOTE: Skin lies one
radius beneath the Y-axis

```

SS\_CUT = -0.05\*VEL\_CONVER ! 0.8\*(BOTTOMBOUND+R) ! Steady State cut speed to at 80% of skin depth in 1 sec

!-----  
! \*\*\*\*\* Type 1 - BLADE STRUC \*\*\*\*\*

ET,1,PLANE182 !\* 2D 4-NODE STRUCTURAL SOLID ELEMENT  
KEYOPT,1,1,2 !\* ENHANCE STRAIN FORMULATION  
KEYOPT,1,3,2 !\* PLANE STRAIN

!-----  
! \*\*\*\*\* Type 2 - RIGHT SKIN STRUC \*\*\*\*\*

ET,2,PLANE182 !\* 2D 4-NODE STRUCTURAL SOLID ELEMENT  
KEYOPT,1,1,2 !\* ENHANCE STRAIN FORMULATION  
KEYOPT,1,3,2 !\* PLANE STRAIN

!-----  
! \*\*\*\*\* Type 3 - LEFT SKIN STRUC \*\*\*\*\*

ET,3,PLANE182 !\* 2D 4-NODE STRUCTURAL SOLID ELEMENT  
KEYOPT,1,1,2 !\* ENHANCE STRAIN FORMULATION  
KEYOPT,1,3,2 !\* PLANE STRAIN

!-----  
! \*\*\*\*\* Type 4 - BARRIER STRUC \*\*\*\*\*

ET,4,PLANE182 !\* 2D 4-NODE STRUCTURAL SOLID ELEMENT  
KEYOPT,1,1,2 !\* ENHANCE STRAIN FORMULATION  
KEYOPT,1,3,2 !\* PLANE STRAIN

! \*\*\*\*\* CONTACT CONDITIONS \*\*\*\*\*

ET,5,TARGE169 ! 2-D TARGET ELEMENTS - lines 7 & 9 - blade is stiffer, courser, and more flat  
ET,6,CONTA175 ! 2-D CONTACT ELEMENTS

!-----  
! \*\*\*\*\* MATERIAL PROPERTIES \*\*\*\*\*

! 1020 Steel

:<http://www.matweb.com/search/datasheet.aspx?matguid=12c37b34695945afb47d8446162febf3&ckck=1>

! [http://books.google.com/books?id=JDd61NujspYC&pg=SA4-PA17&lpg=SA4-PA17&dq=1020+steel+shear+strength&source=bl&ots=YkttE1k-rT&sig=cBoZY\\_YFz8yN4U873AFey0Jriro&hl=en&sa=X&ei=tS4AUc3eOpP08AS9-oC4CQ&ved=0CEoQ6AEwBA#v=onepage&q=1020%20steel%20shear%20strength&f=false](http://books.google.com/books?id=JDd61NujspYC&pg=SA4-PA17&lpg=SA4-PA17&dq=1020+steel+shear+strength&source=bl&ots=YkttE1k-rT&sig=cBoZY_YFz8yN4U873AFey0Jriro&hl=en&sa=X&ei=tS4AUc3eOpP08AS9-oC4CQ&ved=0CEoQ6AEwBA#v=onepage&q=1020%20steel%20shear%20strength&f=false)

### ! TIEBREAK STRESSES

! NormStress= 400000\*STRESS\_CONVER! 10E3\*(10^-8) ! NORM\_TEST !  
12.75\*10E4 ! 12.75\*10^6 Pa \* Conversion=1

! [http://www.satoriseal.com/technical/technical\\_articles/physical\\_properties\\_of\\_rubber\\_part\\_1\\_of\\_2.htm](http://www.satoriseal.com/technical/technical_articles/physical_properties_of_rubber_part_1_of_2.htm)

! ShearStress= 500000\*STRESS\_CONVER ! 6E3\*(10^-8) ! SHEAR\_TEST !  
10\*10E6 ! 50\*10^6 Pa \* Conversion=1

! [http://scholar.lib.vt.edu/theses/available/etd-02252002-131148/unrestricted/1JTS\\_ETD.pdf](http://scholar.lib.vt.edu/theses/available/etd-02252002-131148/unrestricted/1JTS_ETD.pdf)

! EDMP,RIGI,1,6,7 ! STEEL BLADE - RIGID PROPERTIES

! MP,DENS,1, 7650\*DENSITY\_CONVER! ! 7650 kg/m^3 (azom.com) \* [ conversion 1  
kg/m^3 = 10E-12 mg / micron^3 ]

MP,EX,1, 200E5 !MPa ! 200E+09\*(10^-8) ! 2.04E+09 ! 200  
GPa (azom.com)

MP,NUXY,1,0.285 ! efunda.com

!-----  
! \*\*\*\*\* VISCOELASTIC MODELS \*\*\*\*\*

!C10 = 0.558\*10E2 !0.293\*10E2!\*10E2

!C01 = 0.342\*10E2 !0.177\*10E2!\*10E2

E\_skin=0.77\*10E2! 0.77\*10E2

! C01 = 6353254.64!0.177\*10E2 !\*10E2

! C02 = 1102854.70

! C10 = -3934108.58!0.293\*10E2 !\*10E2

! C11 = -240.44

! C20 = -164.05

C01 = 6.4446E2!0.177\*10E2 !\*10E2

C02 = 1.1218 E2

C10 = -4.0028E2!0.293\*10E2 !\*10E2

C11 = -0.00054117E2  
C20 = -0.00014829E2

MP,EX,2,E\_skin

TNMAX=11.61E2 !8 !MPa  
delta\_norm=0.01  
delta\_shear=0.01

! SKIN\_DEN = 1000\*DENSITY\_CONVERT  
MU=0.49967  
DD = (1-2\*MU)/(C10+C01)  
TB,HYPER,1,1,2,MOONEY  
TBDATA,1,C10,C01,DD

! MP,dens,2, SKIN\_DEN ! \*10E-12 ! 1.02 g/cm^3 = 1020kg/m^3 according to Liang &  
Boppart \* [ conversion 1 kg/m^3 = 10E-12 mg / micron^3 ]  
MP,nuxy,2,MU ! Generally accepted as 0.5, for FEM best to approximate  
TB,HYPER,1,1,2,MOONEY  
TBDATA,1, C10 ! 80\*6894.75729 ! C10 ! 80 C10 (psi) \* 6894.75729 (psi/Pa)  
TBDATA,2, C01 ! 20\*6894.75729 ! C01 g/cm^2 !C01 ! 20(psi) \*  
6894.75729(psi/Pa)

! MP,dens,3, SKIN\_DEN ! \*10E-12 ! 1.02 g/cm^3 = 1020kg/m^3 according to Liang &  
Boppart \* [ conversion 1 kg/m^3 = 10E-12 mg / micron^3 ]  
MP,EX,3,E\_skin  
MP,nuxy,3,MU ! Generally accepted as 0.5, for FEM best to approximate  
TB,HYPER,3,1,2,MOONEY  
TBDATA,1,C10,C01,DD

!-----  
! \*\*\*\*\* BLADE GEOM / MESH \*\*\*\*\*  
! DEFINE KEYPOINTS  
K,1,0,-R !Blade Tip  
K,2,R,0 !Blade Outside Arc End  
K,3, !Blade Inside  
K,4,0,BLD\_LENGTH !BLADE INSIDE TOP

```

K,5,BLD_THICK, BLD_LENGTH !BLADE OUTSIDE TOP
CSYS,1,
K,6,R,-THETA !INTERCEPT
CSYS,0

LARC,1,2,3,R !RADIUS LINE 1
L,2,3 !RADIUS TOP LINE 2
L,3,1 !RADIUS INNER SIDE LINE 3
AL,1,2,3, !RADIUS AREA 1

L,6,5 !BLADE LENGTH OUTER LINE 4
L,5,4 !BLADE LENGTH TOP LINE 5
L,4,3 !BLADE LENGTH INNER LINE 6
L,3,6 !BLADE LENGTH BOTTOM LINE 7
AL,4,5,6,7 !BLADE LENGTH AREA 2

AADD,1,2 !SCALPEL AREA 3 LINE 1 DELETED

K,2,2*R,0 !Blade Outside Arc End
L,3,2 ! NEW LINE 1
ASBL,3,1 !DIVIDES AREA 3 BY NEW LINE 1

LCOMB,7,8,0 !COMBINES ADJACENT LINES INTO NEW
LINE 7

TYPE, 1
MAT, 1
MSHKEY,2 ! use mapped meshing
ALLSEL
LESIZE,2, , ,BLDDIV_X
LESIZE,3, , ,BLDDIV_X ! LESIZE, NL1, SIZE, ANGSIZ, **NDIV**, SPACE, KFORC,
LAYER1, LAYER2, KYNDIV

TYPE, 1
MAT, 1
! MSHAPE,0,2D ! mesh with quadrilateral shaped elements
MSHKEY,2 ! use mapped meshing
LESIZE,5, , ,BLDDIV_X ! LESIZE, NL1, SIZE, ANGSIZ, **NDIV**, SPACE, KFORC,
LAYER1, LAYER2, KYNDIV

LSEL,S,LINE,,6,9,3 !* DEFINE LINE DIVISION ! selects lines side edges of rects set
same divisions as right skin

```

```
LESIZE,ALL, , ,BLDDIV_Y      ! LESIZE, NL1, SIZE, ANGSIZ, **NDIV**, SPACE,  
KFORC, LAYER1, LAYER2, KYNDIV
```

```
AMESH,2  
AMESH,1
```

```
!-----  
!      ***** SKIN AREAS *****  
RECTNG,0,RIGHTBOUND,(CRACK_Y-OFFSET),(BOTTOMBOUND-OFFSET)      !*  
DEFINE AREAS - Lines numbered counterclockwise from bottom  
RECTNG,0,LEFTBOUND,(CRACK_Y-OFFSET),(BOTTOMBOUND-OFFSET)      !  
RECTNG, X1, X2, Y1, Y2  
k, 1001, NOTCH_X, (NOTCH_Y-OFFSET), 0  
k, 1002, RIGHTBOUND, (-OFFSET), 0  
A, 1001, 9, 8,1002
```

```
!-----  
!      ***** RIGHT SKIN MESH *****  
MSHAPE,0,2D ! mesh with quadrilateral shaped elements  
MSHKEY,1 ! use mapped meshing  
TYPE,2  
MAT, 2  
ALLSEL
```

```
SPACE_Y = 2  
SPACE_Y_NOTCH = 2  
SPACE_X = 2  
SPACE_X_NOTCH = 2  
SPACE_X_TOP = 0.5
```

```
LSEL,S,LINE,,4,      !* DEFINE LINE DIVISION ! selects lines side edges of rects set same  
divisions as right skin  
LESIZE,ALL, , ,SKINDIV_Y,1/SPACE_Y      ! LESIZE, NL1, SIZE, ANGSIZ, **NDIV**,  
SPACE, KFORC, LAYER1, LAYER2, KYNDIV
```

```
LSEL,S,LINE,,10,     !* DEFINE LINE DIVISION ! selects lines side edges of rects set same  
divisions as right skin  
LESIZE,ALL, , ,SKINDIV_Y,SPACE_Y      ! LESIZE, NL1, SIZE, ANGSIZ, **NDIV**,  
SPACE, KFORC, LAYER1, LAYER2, KYNDIV
```

```
LSEL,S,LINE,,8,,      !* DEFINE LINE DIVISION ! selects lines top of rect set 1 division
LESIZE,ALL, , ,SKINDIV_X,1/SPACE_X
```

```
LSEL,S,LINE,,1,,      !* DEFINE LINE DIVISION ! selects lines top of rect set 1 division
LESIZE,ALL, , ,SKINDIV_X,SPACE_X
```

```
LSEL,S,LINE,,15,,     !* DEFINE LINE DIVISION ! selects lines side edges of rects set same
divisions as right skin
LESIZE,ALL, , ,NOTCHDIV_Y,1/SPACE_Y_NOTCH      ! LESIZE, NL1, SIZE, ANGSIZ,
**NDIV**, SPACE, KFORC, LAYER1, LAYER2, KYNDIV
```

```
LSEL,S,LINE,,16,,     !* DEFINE LINE DIVISION ! selects lines side edges of rects set
same divisions as right skin
LESIZE,ALL, , ,NOTCHDIV_Y,SPACE_Y_NOTCH      ! LESIZE, NL1, SIZE, ANGSIZ,
**NDIV**, SPACE, KFORC, LAYER1, LAYER2, KYNDIV
```

```
LSEL,S,LINE,,17      !* DEFINE LINE DIVISION ! selects lines top of rect set 1 division
LESIZE,ALL, , ,SKINDIV_X,SPACE_X_TOP
AMESH, 3, 5, 2
```

```
!-----
!      ***** LEFT SKIN MESH *****
```

```
ALLSEL,ALL
LSEL,S,LINE,,12,,     !* DEFINE LINE DIVISION ! selects lines side edges of rects set same
divisions as right skin
LESIZE,ALL, , ,SKINDIV_Y,1/SPACE_Y      ! LESIZE, NL1, SIZE, ANGSIZ, **NDIV**,
SPACE, KFORC, LAYER1, LAYER2, KYNDIV
```

```
LSEL,S,LINE,,14,,     !* DEFINE LINE DIVISION ! selects lines side edges of rects set same
divisions as right skin
LESIZE,ALL, , ,SKINDIV_Y,SPACE_Y      ! LESIZE, NL1, SIZE, ANGSIZ, **NDIV**,
SPACE, KFORC, LAYER1, LAYER2, KYNDIV
```

```
LSEL,S,LINE,,11,13,2  !* DEFINE LINE DIVISION ! selects lines top of rect set 1
division
LESIZE,ALL, , ,1
```

```
TYPE, 3
```

MAT, 1  
AMESH, 4  
ALLSEL, ALL

!-----  
! \*\*\*\*\* SKIN TO SKIN BARRIER \*\*\*\*\*  
RECTNG,0,LEFTBOUND,(CRACK\_Y-OFFSET) ,(BOTTOMBOUND-OFFSET) !  
RECTNG, X1, X2, Y1, Y2  
RECTNG,0,LEFTBOUND,(CRACK\_Y-OFFSET) ,(-R-OFFSET) ! RECTNG, X1, X2,  
Y1, Y2

!-----  
! \*\*\*\*\* BARRIER SKIN MESH \*\*\*\*\*

LSEL,S,LINE,,23,25,2 !\* DEFINE LINE DIVISION ! selects lines side edges of rects set  
same divisions as right skin  
LESIZE,ALL, , ,LSKIN3DIV\_Y ! LESIZE, NL1, SIZE, ANGSIZ, \*\*NDIV\*\*, SPACE,  
KFORC, LAYER1, LAYER2, KYNDIV

LSEL,S,LINE,,22,24,2 !\* DEFINE LINE DIVISION ! selects lines top of rect set 1  
division  
LESIZE,ALL, , ,1

TYPE, 4  
MAT, 1  
AMESH, 7,

ALLSEL, ALL

!-----  
! \*\*\*\*\* CONTACT CONDITIONS \*\*\*\*\*

ALLSEL !CONTACT RIGHTSKIN  
ET, 7,INTER202  
KEYOPT,7,3,2

TB,CZM,7,,EXPO  
TBDATA,1,TNMAX,delta\_norm,delta\_shear  
!CMSEL, S, RIGHT\_ELEM, ELEM

```

!CMSEL, A, LEFT_ELEM, ELEM
!E,232,272,2283,2244
!CZMESH, RIGHT_ELEM,LEFT_ELEM ,,,
CSYS,0
NSEL, S,LOC,Y,(CRACK_Y-OFFSET-0.5*R),BOTTOMBOUND-OFFSET
NUMMRG,NODES
ESLN
TYPE,7
MAT,7
CZMESH, , ,0,X,0

```

```

ALLSEL
TYPE,5
courser, and more flat
ESEL,S,TYPE,,1
NSLE
ESURF,
! 2-D TARGET ELEMENTS - lines 7 & 9 - BLADE is stiffer,

```

```

ALLSEL
TYPE,6
ESEL,S,TYPE,,2
NSLE
ESURF,
!Target RIGHTSKIN

```

```

! !***** NAMING *****

```

```

ALLSEL
! EDPART, CREATE
LEFTSKIN=3 BARRIER=4
ESEL, S, TYPE, , 1
NSLE
CM, BLADE, NODE
!BLADE = 1 RIGHTSKIN =2

```

```

ESEL, S, TYPE, , 2
NSLE
CM, RIGHTSKIN, NODE

```

```

ESEL, S, TYPE, , 3
ESEL, A, TYPE, , 4
NSLE
CM, LEFTSKIN, NODE

```

```

Seltol, SEL_TOL

```

```
CMSEL, S, RIGHTSKIN, NODE          ! NAMES THE RIGHTBOUND
NSEL, R, LOC, X, RIGHTBOUND
CM, RIGHTBOUND, NODE
!*
```

```
CMSEL,S, LEFTSKIN, NODE            !Names Left Side
NSEL, R, LOC, X, LEFTBOUND
CM, LEFTBOUND, NODE
!*
```

```
CMSEL, S, RIGHTSKIN, NODE          ! NAMES THE Right side of Crack
NSEL, R, LOC, X, 0
CM, RIGHTEDGE, NODE
!*
```

```
ESEL, S, TYPE, , 3
NSLE
NSEL, R, LOC, X, 0
CM, LEFTEDGE, NODE
```

```
CMSEL, S, RIGHTSKIN, NODE
NSEL, R, LOC, X, 0
NSEL, R, LOC, Y, BOTTOMBOUND-OFFSET
CM, CORNER_R, NODE                ! Right Crack Base CORNER_B
```

```
CMSEL, S, LEFTSKIN, NODE           ! Names Left Crack Base
CORNER_D
NSEL, R, LOC, X, 0
NSEL, R, LOC, Y, BOTTOMBOUND-OFFSET
CM, CORNER_L, NODE                ! BOTTOM CORNER
```

```
CMSEL,S,LEFTEDGE,NODE
ESLN
CM, LEFT_ELEM,ELEM
```

```
CMSEL,S,RIGHTEDGE,NODE
ESLN
ESEL, U,ELEM,,1731
CM, RIGHT_ELEM,ELEM
```

```
!-----  
!***** Boundary Conditions *****
```

```
CMSEL,S,RIGHTBOUND, NODE      ! Fix right bound in X direction  
D,ALL,UX,0  
D,ALL,UY,0  
!*
```

```
CMSEL, S, LEFTSKIN, NODE  
D,ALL,UY,0  
D,ALL,UX,0
```

```
ALLSEL,all  
!EDCLIST !Lists contact entity specifications in an explicit dynamics analysis.
```

```
!!-----  
!!          ***** LOAD CONDITIONS *****
```

```
/SOLU          ! Enter solution processor  
ANTYPE,STATIC  
CSYS,0  
CMSEL,S,BLADE  
D,BLADE,UY,(-5*R)  
D,BLADE,UX
```

```
NSEL,ALL  
ESEL,ALL  
NLGEOM,ON  
TIME,1
```

```
!NSUBST,100,100,100  
AUTOTS, ON  
!deltim check for manual sub-stepping
```

```
OUTRES,ALL,ALL  
SOLVE          !* PERFORM SOLUTION  
!          ***** LOAD CONDITIONS *****
```

```
!! CSYS,0  
!! CMSEL,S,BLADE  
!! D,BLADE,UY,0
```

```
!! NSEL,ALL
!! ESEL,ALL
!! NLGEOM,ON
!! TIME,2

!! !NSUBST,100,100,100
!! AUTOTS, ON

!! OUTRES,ALL,ALL
!! SOLVE          !* PERFORM SOLUTION
```

## A.2 Ansys Post Processing File (Post\_E)

```
! !post proc
! RESUME,CourseBlade_proc1
/OUTPUT, PostProc_junk, txt,
ASEL, S,AREA, ,7,11,4           ! BLADE EXTERIOR
NSLA,s,1
CM, BLADE_EXT, NODE

!Z_loc= extrude*3/5
SX_TOL = 0 ! 0.000001

! *** Set up Crack Selection Arrays ***
CMSEL,S,RIGHTEDGE,NODE
!NSEL,R,LOC,Z,0
*GET,CRACK_COUNT, NODE, ,COUNT           ! number of nodes selected
*VGET, CRACK_NODE,NODE, ,NLIST,          ! returns list of selected nodes

cmsel,s,BLADE,NODE
NSEL,R,LOC,Y,-R
!NSEL,R,LOC,Z,0
*GET, BLADE_TIP_NUM, NODE,0,NUM,MAX

! creates a matrix of crack position along Y and corresponding node numbers on each side
! cycles selected node path and retrives maximum Y-position value and retrieves the node
number
! Then the selected node path is reset to omit the previously selected maximum Y node location
*DIM,CRACK_Y_POSITION,ARRAY,CRACK_COUNT,3           ! col 1 is position Y;
col 2 is right skin node num; col 3 is leftskin node num
MAX_Y = CRACK_Y
*DO, j, 1, CRACK_COUNT, 1
    CMSEL, S, RIGHTSKIN, NODE
!    NSEL,R, LOC, Z, 0
    NSEL,R, LOC, x, 0
    NSEL, R, LOC, Y, BOTTOMBOUND-OFFSET,MAX_Y
    *GET, MAX_Y, NODE, 0, MXLOC, Y,

    NSEL, R, LOC, Y, MAX_Y,
    *GET, NODE_Y, NODE,0, NUM,MAX,
    CMSEL, S, LEFTSKIN, NODE
    NSEL,R, LOC, Z, 0
    NSEL,R, LOC, x, 0
```

```

NSEL, R, LOC, Y, MAX_Y,
*GET, NODE_Y_LEFT, NODE,0, NUM,MAX,
CRACK_Y_POSITION(j,1)=MAX_Y
CRACK_Y_POSITION(j,2)=NODE_Y
CRACK_Y_POSITION(j,3)=NODE_Y_LEFT

MAX_Y = MAX_Y - 1.1*SEL_TOL
*ENDDO

! Time Array
TIME_count=202

*DIM,TTime,ARRAY,TIME_count,1      ! 202 rows 1 column

/post1
!! *** Crack Growth over Time Array ***
! cycles crack path and when displacement UX is greater than a tolerance, crack is found and exit
cycle
*get, last_num,active, 0, set, nset,
*DIM, CRACK_DATA, ARRAY,last_num,5! output array Col 1 time, col 2 node#, col 3 x, col
4 y, col 5 stress Rows: Facecount
ALLSEL
selecttol=(0.05*R/3)
SET,FIRST
NODE_LAST=CRACK_Y_POSITION(CRACK_COUNT,2)
*DO, i, 1, last_num      ! Cycles through solution sets
  *DO, j, CRACK_COUNT, 1, -1      ! note this should equal
FACECOUNT_left

      ALLSEL
      *GET, NODE_X, NODE, CRACK_Y_POSITION(j,2), U, X,

      *if, NODE_X, NE, NODE_LAST,THEN
          tracking=1
      *else
          tracking =0
      *endif

      *if, NODE_X, GT,selecttol,THEN      ! AND,
NODE_STRESS_LEFT, LT,SX_TOL
          NODE_NUM = CRACK_Y_POSITION(j+tracking,2)
          *GET, CRACK_UY, NODE, NODE_NUM, U, Y, !
CRACK_Y_POSITION col 2 is the rightskin node numb

```

```

*GET, CRACK_UX, NODE, NODE_NUM, U, X,
*GET, STRESS_EQV, NODE, NODE_NUM, S, EQV,
CRACK_DATA(i,2) = NODE_NUM ! rightskin node number
CRACK_DATA(i,3) = CRACK_UX
CRACK_DATA(i,4) =
CRACK_UY+CRACK_Y_POSITION(j+tracking,1) ! displacement of node j at time i plus
original position of node j
CRACK_DATA(i,5) = STRESS_EQV
*Exit
*Endif
*ENDDO
SET,NEXT
*ENDDO

!!! *** Max Stress Along Crack over Time Array ***
! sorts selected nodes by stress places desired data into array
! cycles over all time steps
*DIM, PATH_DATA, ARRAY,last_num, 5
SET,FIRST
*DO, i, 1, last_num ! Cycles through solution sets
CMSEL, S, RIGHTEDGE, NODE
! NSEL,R,LOC, Z,Z_LOC

NSORT, S, EQV,0, 1, ,
*GET,NODE_STRESS, SORT,0,MAX
*GET,NODE_NUM, SORT,0,IMAX

*GET, NODE_LOC_X, NODE, NODE_NUM,LOC, X,
*GET, NODE_LOC_Y, NODE, NODE_NUM,LOC, Y,

*GET, NODE_UX, NODE, NODE_NUM, U, X,
*GET, NODE_UY, NODE, NODE_NUM, U, Y, ! CRACK_Y_POSITION col 2
is the rightskin node numb

PATH_DATA(i,2) = NODE_NUM ! node number
PATH_DATA(i,3) = NODE_UX+NODE_LOC_X
PATH_DATA(i,4) = NODE_UY+NODE_LOC_Y
PATH_DATA(i,5) = NODE_STRESS

SET,NEXT
*ENDDO

!!! *** Max Stress In RIGHTSKIN ***

```

! sorts selected nodes by stress places desired data into array  
! cycles over all time steps

```
*DIM, STRESS_DATA, ARRAY, last_num, 5
SET, FIRST
*DO, i, 1, last_num          ! Cycles through solution sets
    CMSEL, S, RIGHTSKIN, NODE
    NSORT, S, EQV, 0, 1, ,
    *GET, NODE_STRESS, SORT, 0, MAX
    *GET, NODE_NUM, SORT, 0, IMAX

    *GET, NODE_LOC_X, NODE, NODE_NUM, LOC, X,
    *GET, NODE_LOC_Y, NODE, NODE_NUM, LOC, Y,

    *GET, NODE_UX, NODE, NODE_NUM, U, X,
    *GET, NODE_UY, NODE, NODE_NUM, U, Y, ! CRACK_Y_POSITION col 2
is the rightskin node numb
```

```
    STRESS_DATA(i,2) = NODE_NUM          ! node number
    STRESS_DATA(i,3) = NODE_UX + NODE_LOC_X
    STRESS_DATA(i,4) = NODE_UY + NODE_LOC_Y
    STRESS_DATA(i,5) = NODE_STRESS
```

```
SET, NEXT
*ENDDO
```

!-----

```
*DIM, BLADE_LOAD, ARRAY, last_num, 3
SET, FIRST
*DO, i, 1, last_num
    ESEL, S, TYPE, , 5
    ESLN
    NSLE
    FSUM, , CONTA
    *GET, SUM_LOAD, FSUM, 0, ITEM, FY,
    *GET, NODE_LOC_Y, NODE, BLADE_TIP_NUM, LOC, Y,
    *GET, NODE_UY, NODE, BLADE_TIP_NUM, U, Y,
    BLADE_LOAD(i,2) = SUM_LOAD
    BLADE_LOAD(i,3) = NODE_UY + NODE_LOC_Y
SET, NEXT
*ENDDO
```

```
/post26
FILE, 'CourseBladeSkin', 'rst', '.'
```

```
/UI,COLL,1
NUMVAR,200
SOLU,191,NCMIT
STORE,MERGE
FILLDATA,191,,,,1,1
REALVAR,191,191
```

```
VGET,STRESS_DATA(1,1,1),1      ! places time into col 1
VGET,PATH_DATA(1,1,1),1
VGET,CRACK_DATA(1,1,1),1      ! places time into col 1
VGET,BLADE_LOAD(1,1,1),1
! RESUME,CourseBlade_proc1
!! *** Writes File ***
```

```
! *DIM,TTIME,ARRAY,last_num    ! Dimension array for time values
! VGET,TTIME(1,1,1),1          ! Fill array with values of time - VGET, Par,
IR, TSTRT, KCPLX
! *CFOPEN,TTIME,txt
! *VWRITE,TTIME(1)
! %14.5G
! *CFCLOSE
```

## A.2 Ansys Output File (Write\_Command2)

```
!RESUME,CourseBlade_proc1, db
!! *** Writes File ***
/OUTPUT, Write_junk, txt,
/post26
FILE,'CourseBladeSkin','rst','.'
/UI,COLL,1
SOLU,191,NCMIT
STORE,MERGE
FILLDATA,191,,1,1
REALVAR,191,191
```

```
*DIM,TTIME,ARRAY,last_num           ! Dimension array for time values
VGET,TTIME(1,1,1),1                 ! Fill array with values of time - VGET, Par,
IR, TSTRT, KCPLX
*CFOPEN,TTIME,txt
*VWRITE,TTIME(1)
% 14.5G
*CFCLOSE
```

```
*CFOPEN,STRESS_DATA,txt
*VWRITE,'Maximum Stress in Skin'
% 25C
*VWRITE,'TIME', 'Node Number', 'X ', 'Y ', 'S_EQV'
% 7C % 22C % 6C % 14C % 18C
*VWRITE,STRESS_DATA(1,1,1), STRESS_DATA(1,2,1), STRESS_DATA(1,3,1),
STRESS_DATA(1,4,1), STRESS_DATA(1,5,1),
% 14.5G % 14.5G % 14.5G % 14.5G % 14.5G
*CFCLOSE
```

```
*CFOPEN,PATH_DATA,txt
*VWRITE,'Maximum Stress Along Crack Path'
% 34C
*VWRITE,'TIME', 'Node Number', 'X ', 'Y ', 'S_EQV'
% 7C % 22C % 6C % 14C % 18C
*VWRITE,PATH_DATA(1,1,1), PATH_DATA(1,2,1), PATH_DATA(1,3,1),
PATH_DATA(1,4,1), PATH_DATA(1,5,1),
% 14.5G % 14.5G % 14.5G % 14.5G % 14.5G
*CFCLOSE
```

```

*CFOPEN,CRACK_DATA,txt
*VWRITE,'Stress At Crack Tip'
%22C
*VWRITE,'TIME', 'Node Number', 'X ', 'Y ', 'S_EQV'
%7C %22C %6C %14C %18C
*VWRITE,CRACK_DATA(1,1,1), CRACK_DATA(1,2,1), CRACK_DATA(1,3,1),
CRACK_DATA(1,4,1), CRACK_DATA(1,5,1),
%14.5G %14.5G %14.5G %14.5G %14.5G
*CFCLOSE

*CFOPEN,CRACK_Y_POSITION,txt
*VWRITE,'Crack Numbers & Loc Y'
%S
*VWRITE,'Y', 'Right Node', 'Left Node',
%4C %25C %14C
*VWRITE,CRACK_Y_POSITION(1,1,1), CRACK_Y_POSITION(1,2,1),
CRACK_Y_POSITION(1,3,1)
%14.5G %14.5G %14.5G
*CFCLOSE

*CFOPEN,Y_COMPARISON,txt
*VWRITE,'Crack Loc Y & Peak Stresses'
%S
*VWRITE,'TIME','Crack Tip', 'Max Stress', 'Max Stress Path',
%7C %21C %16C %17C
*VWRITE,TTIME(1), CRACK_DATA(1,3,1), STRESS_DATA(1,4,1), PATH_DATA(1,4,1)
%14.5G %14.5G %14.5G %14.5G
*CFCLOSE

*CFOPEN,BLADE_LOAD,txt
*VWRITE,'Blade Y-Reaction Force'
%S
*VWRITE,'TIME','Load','Position',
%7C %21C %16C %17C
*VWRITE,BLADE_LOAD(1,1,1), BLADE_LOAD(1,2,1),BLADE_LOAD(1,3,1)
%14.5G %14.5G %14.5G %14.5G
*CFCLOSE

```

## APPENDIX B: TECHNICAL DRAWINGS



## APPENDIX C: EXPERIMENTAL DATA